Spring 2016

A multimodal machine-learning graph-based approach for segmenting glaucomatous optic nerve head structures from SD-OCT volumes and fundus photographs

Mohammad Saleh Miri
University of Iowa

A MULTIMODAL MACHINE-LEARNING GRAPH-BASED APPROACH FOR SEGMENTING GLAUCOMATOUS OPTIC NERVE HEAD STRUCTURES FROM SD-OCT VOLUMES AND FUNDUS PHOTOGRAPHS

by

Mohammad Saleh Miri

A thesis submitted in partial fulfillment of the
requirements for the Doctor of Philosophy degree
in Electrical and Computer Engineering
in the Graduate College of
The University of Iowa

May 2016

Thesis Supervisor: Associate Professor Mona K. Garvin

Graduate College
The University of Iowa
Iowa City, Iowa

CERTIFICATE OF APPROVAL

PH.D. THESIS

This is to certify that the Ph.D. thesis of

Mohammad Saleh Miri

has been approved by the Examining Committee for the thesis requirement for the Doctor of Philosophy degree in Electrical and Computer Engineering at the May 2016 graduation.

Thesis Committee: _____
Mona K. Garvin, Thesis Supervisor

_____
Michael D. Abràmoff

_____
Joseph M. Reinhardt

_____
Todd Scheetz

_____
Milan Sonka

There are a number of people to whom I am greatly indebted, and to whom I would like to dedicate this thesis with pleasure:
To my parents and brother for their selfless love, and encouragement and guidance all throughout my life to pursue my educational dreams.
To my in-laws, the Mortazavi family, for their constant reassurance, support and advice throughout these many stressful years.
And finally to my brilliant and beautiful wife, Maryam, whose love and confidence is a constant source of inspiration and encouragement.

ACKNOWLEDGEMENTS

I feel blessed and fortunate to have had the help and support of so many individuals throughout my lifetime to achieve/get me to where I am today, and I would like to extend my sincere thanks to all of them.

First I want to thank my advisor Dr. Mona K. Garvin for all her contributions of time, ideas, and funding to make my Ph.D. experience productive and stimulating. The passion and enthusiasm she has for her research was motivational for me, even during tough times in the Ph.D. pursuit. I would also want to thank the faculty members of our weekly OCT meetings, Dr. Milan Sonka, Dr. Michael D. Abràmoff, and Dr. Young H. Kwon, who have contributed immensely to my professional time at the University of Iowa by their invaluable advice and encouragement. I am also grateful for the help of the past and current members of the OCT meetings, Kyungmoo Lee, Li Zhang, Li Tang, Mindert Niemeijer, Hrvoje Bogunovič, and Andreas Whale. My colleagues and friends in the lab Bhavna J. Antony, Jui-Kai Wang, Qiao Hu, Victor Robles, Wenxiang Deng, and Jason Agne also deserve special mention here.

In addition, I would like to thank the coauthors from other labs who contributed in my publications, Dr. Xiaodong Wu, Dr. Punam Saha, Dr. Randy H. Kardon, Dr. Hans J. Johnson, Dr. Wallace L. M. Alward, Susannah Q Longmuir, Ali Ghayoor, Junjie Bai, and Yinxiao Liu. I also would like to thank Dr. Mona Garvin and Dr. Young H. Kwon for their effort and valuable time that they spent on providing ground truth and manual delineation of optic nerve head structures. Creation of reference standards is extremely important and the evaluation of my thesis would not be possible without having the reference standards. Mses Cathy Kern and Dina Blanc also deserve a special thank for being a great help in the department's office.

This work was supported, in part, by the National Institutes of Health grants R01 EY018853 and R01 EY023279; the Department of Veterans Affairs Rehabilitation Research and Development Division (Iowa City Center for the Prevention and

Treatment of Visual Loss and Career Development Award 1IK2RX000728); and the Marlene S. and Leonard A. Hadley Glaucoma Research Fund.

ABSTRACT

Glaucoma is the second leading cause of blindness worldwide. The clinical standard for monitoring the functional deficits in the retina that are caused by glaucoma is the visual field test. In addition to monitoring the functional loss, evaluating disease-related structural changes in the human retina also helps with diagnosis and management of this progressive disease. The characteristic changes of retinal structures such as the optic nerve head (ONH) are monitored utilizing imaging modalities such as color (stereo) fundus photography and, more recently, spectral-domain optical coherence tomography (SD-OCT). With the inherent subjectivity and time required for manually segmenting retinal structures, there has been a great interest in automated approaches. Since both fundus and SD-OCT images are often acquired for the assessment of glaucoma, automated segmentation approaches can benefit from combining multimodal complementary information from both sources.

The goal of the current work is to automatically segment the retinal structures and extract the proper parameters of the optic nerve head related to the diagnosis and management of glaucoma. The structural parameters include the cup-to-disc ratio (CDR) which is a 2D parameter and is obtainable from both fundus and SD-OCT modalities. Bruch's membrane opening-minimum rim width (BMO-MRW) is a recently introduced 3D structural parameter that is obtainable from the SD-OCT modality only. We propose to use the complementary information from both fundus and SD-OCT modalities in order to enhance the segmentation of structures of interest. In order to enable combining information from different modalities, a feature-based registration method is proposed for aligning the fundus and OCT images. In addition, our goal is to incorporate the machine-learning techniques into the graph-theoretic approach that is used for segmenting the structures of interest.

Thus, the major contributions of this work include: 1) use of complementary information from SD-OCT and fundus images for segmenting the optic disc and cup boundaries in both modalities, 2) identifying the extent that accounting for the pres-

ence of externally oblique border tissue and retinal vessels in rim-width-based parameters affects structure-structure correlations, 3) designing a feature-based registration approach for registering multimodal images of the retina, and 4) developing a multimodal graph-based approach to segment the optic nerve head (ONH) structures such as internal limiting membrane (ILM) surface and Bruch's membrane surface's opening.

PUBLIC ABSTRACT

Glaucoma is one of the major leading causes of blindness worldwide. In addition to functional deficits, monitoring and evaluating disease-related structural changes in the human retina also helps with diagnosis and management of this progressive disease. Color (stereo) fundus photography and, more recently, spectral-domain optical coherence tomography (SD-OCT), are two types of imaging modalities that are currently utilized for monitoring the characteristic changes of retinal structures such as the optic nerve head (ONH).

With the inherent subjectivity and time required for manually segmenting retinal structures, there has been a great interest in automated approaches. The goal of the current work is to automatically segment the retinal structures and extract the proper parameters of the optic nerve head related to the diagnosis and management of glaucoma. The structural parameters include: 1) cup-to-disc ratio (CDR) which is a 2D parameter and is obtainable from both fundus and SD-OCT modalities, and 2) Bruch's membrane opening-minimum rim width (BMO-MRW) which is a recently introduced 3D structural parameter that is obtainable from the SD-OCT modality only. Since both fundus and SD-OCT images are often acquired for the assessment of glaucoma, we propose to use the complementary information from both fundus and SD-OCT modalities in order to enhance the segmentation of structures of interest using machine-learning graph-theoretic based approaches.

TABLE OF CONTENTS

LIST OF TABLES

Table

LIST OF FIGURES

Figure

CHAPTER 1
INTRODUCTION

The two types of modalities that are used in this project include color fundus photographs (Fig. 1.1a) and spectral domain-optical coherence tomography (SD-OCT) (Fig.1.1b). The color fundus photographs are 2D images capturing the projective appearance of the back of the eye. In contrast, optical coherence tomography, which is also a noninvasive modality, is capable of 3D imaging of different retinal structures that contain high-resolution (micrometers) and cross-sectional views. OCT was first introduced by Huang *et al.* [1] and it has contributed significantly in the diagnosis and quantitative assessment of ocular diseases. There are two types of OCT: time-domain-OCT (TD-OCT) and spectral-domain-OCT. TD-OCT is the first generation of OCT which was commercially available since 2003. TD-OCT can acquire up to six cross-sectional scans in a single acquisition which makes TD-OCT primarily a 2D imaging technique. The SD-OCT modality, has been commercially available since 2007, has provided truly volumetric imaging of the retinal structures.

The manual segmentation of the retinal structures from SD-OCT images is a very time-consuming task due to the size of 3D volumes. Furthermore, experts do not always agree on the manual delineation of the structure of interest. Hence, fast and reliable automated approaches with high reproducibility is the solution to these

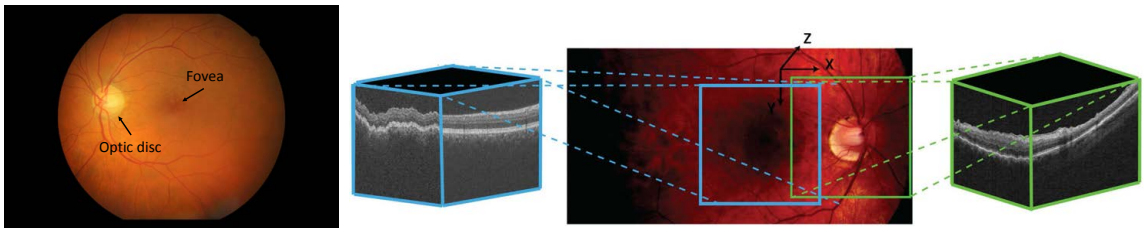

(a) (b)

Figure 1.1: (a) Retina as seen through an ophthalmoscope. (b) The regions scanned in macula-centered (the blue cube) and ONH-centered (the green cube) OCT images.

issues. The automated segmentation, however, is not a trivial task as there are several issues that are needed to be handled properly. There are motion related artifacts and acquisition errors as well as speckle noise which are related to imaging procedure. Moreover, having lower contrast due to the presence of disease or vessel shadows causes the segmentation of structure of interest to be more challenging. As mentioned before, the volumes have relatively large sizes; for instance, Carl Zeiss Meditec Inc. is one of the imaging companies that produces the Cirrus SD-OCT machines which obtain images of size 200×200×1024 voxels from a 6mm×6mm×2mm region. The other issue that needs to be addressed is the structural variation which is the inherent characteristics of retinal structure even in normative data. However, the variation can be substantially larger in the presence of disease. One of the crucially important benefits of 3D volumes is the 3D spatial contextual information available which can be a tremendous help in segmenting the structures that are ambiguous in an individual 2D B-scan as they may be better characterized in 3D context.

Glaucoma causes the ganglion cells along with their axons to die, resulting in thinning of the nerve fiber bundle layer and loss of the neuroretinal rim tissue. Physicians used to diagnose and assess the progression of glaucoma using the visual field test and by looking at the 2D fundus photographs. However, with the SD-OCT modality being commercially available, the opportunity of better understanding the glaucoma disease and studying how structures change due to the disease has been provided. For example, the standardly used cup-to-disc ratio is proposed to be replaced by the new 3D structural parameter called Bruch's membrane opening-minimum rim width (BMO-MRW) [2–6]. The reason is that the optic disc margin tended to be identified from the fundus photographs, however, by looking at the SD-OCT scans it was found that the clinically visible disc margin does not always overlap with the innermost edge of Bruch's membrane visible in SD-OCT. In this work, in addition to providing better approaches for segmentation of traditional structures such as the projected optic

disc and cup, we will focus on the challenges of computing the new retinal structure automatically.

With the inherent subjectivity and time required for experts to segment the optic disc and cup, there has been great interest in automated approaches. Most prior optic disc and cup segmentation approaches have focused on segmenting color fundus images alone [7–15], with few approaches having been presented for the segmentation within SD-OCT volumes alone [16–18]. More specifically, the prior fundus-only approaches for segmenting the disc and cup include pixel-based classification methods [7,8], model-based approaches [9–12], and graph-based approaches [13–15]. Initial SD-OCT-only approaches include the work of Lee *et al.* [16] and Abràmoff *et al.* [17] where each A-scan (i.e., projected pixel location) was classified as cup, rim, or background from SD-OCT features within the A-scan. While the final approach was an SD-OCT-only approach, the pixel-classification-approach was trained and tested using expert-marked color fundus images. Nevertheless, the accuracy of this classification method utilizing SD-OCT-only features was higher than classification methods using fundus-only features.

More recently, Bruch's membrane opening-minimum rim width (BMO-MRW), defined as the minimum Euclidean distance from Bruch's membrane opening to the internal limiting membrane (ILM) surface, is introduced which measures the remaining neuroretinal rim tissue [19] and recent studies showed that BMO-MRW is superior to other structural parameters for diagnosing open-angle glaucoma [20]. Beside the necessity of identifying BMO points for computing the BMO-MRW, the BM surface ending points also define the true optic disc boundary. The 3D imaging ability of SD-OCT machines showed that disc margin (DM) from fundus photographs does not always coincide with the outer border of rim tissue, however, BMO, also referred to as the neural canal opening (NCO), is the true outer border of rim tissue (optic disc boundary) which remains unaltered during the intraocular pressure changes due to

glaucoma [19–21]. The approaches that attempted to segment the BMO from SD-OCT volumes, mostly focused on 2D segmentation of BMO points. For instance, the works in [18] and [22] focused on segmenting the 2D projection of BMO points, while Fu *et al.* found the BMO points from a number of individual 2D B-scans and fitted an ellipse to the points to obtain the complete ring-shape BMO segmentation [23]. The method proposed in [24] was the first step towards obtaining a 3D segmentation, where the authors presented an automated iterative graph-theoretic approach for segmenting multiple surfaces with a shared hole.

Besides identifying the BMO points, obtaining an accurate ILM surface segmentation is required in order to be able to compute the recently introduced BMO-MRW structural parameter. Intraretinal layers are the other important structures of retina and many attempts have been performed in order to segment the intraretinal layer automatically. The early works reported on this area were mostly 2D approaches [25–33]. Other approaches include machine-learning based approaches [34–40], 2D graph-based approaches [41–43], and 3D graph-based approaches [16, 44–46] that have been proposed to automatically segment the intraretinal layers from normative and diseased data. More specifically, precisely segmenting the ILM surface in optic nerve head (ONH)-centered OCT volumes, as needed for computing parameters such as the BMO-MRW of glaucoma patients, can be a challenging task. Since glaucoma patients typically have deeper cups, in order to be able to follow the rapid changes in the shape of the ONH, steep slopes must be allowed in the ILM surface. Moreover, the presence of large retinal blood vessels also makes a precise segmentation of the ILM at the ONH challenging as the larger blood vessels are capable of altering the topology of the ILM surface. Current segmentation approaches include blood vessels and their surrounding gaps (if they exist) as part of the ILM surface.

1.1 Thesis Aims

In this work, human patients showing varying stages of glaucoma disease are imaged using fundus and SD-OCT modalities. The goal is to automatically segment the retinal structures and extract the proper parameters of the optic nerve head related to the diagnosis and management of glaucoma. We propose to use the complementary information from both fundus and SD-OCT modalities in order to enhance the segmentation of structures of interest. In order to be able to combine fundus (color and stereo photographs) and OCT information, we propose a feature-based registration method. In addition, our goal is to incorporate the machine-learning techniques into the graph-theoretic approach that is used for segmenting optic nerve head's structures. More specifically, the cost functions that will be used in graph-theoretic approach are proposed to be designed using machine-learning based methods instead of conventional hand-design methods. Furthermore, the interactions between the neural canal opening structures (i.e. BMO, ILM, and retinal blood vessels) will be taken into consideration in order to address some of the existing issues for ILM surface segmentation and BMO identification. In summary my work has three specific aims:

- **Aim 1: Use complementary information from SD-OCT volumes and fundus photographs for segmenting the optic disc and cup boundaries in both modalities.** This aim is completed using a multimodal machine-learning graph-based approach. The problem is formulated as an optimization problem and using a graph-theoretic approach the optic disc and cup boundaries are segmented simultaneously. The in-region and on-boundary cost functions needed for the graph-theoretic approach are designed using a machine-learning method that utilized multimodal (fundus+SD-OCT) and unimodal (OCT only) feature sets.
- **Aim 2: Identify the extent that accounting for the presence of Externally Oblique Border Tissue (EOBT) and retinal vessels in rim-width-**

based parameters affects structure-structure correlations. In this aim the structure-structure correlation of Retinal Nerve Fiber Layer Thickness (RNFLT) with different rim-width-based parameters in presence of EOBT are computed in order to identify the suitable rim-width-based parameter. Additionally, utilizing the retinal vessels probability map from fundus photographs, the ILM surface is compensated for the presence of retinal blood vessels and the rim-width-based parameter is computed again using the corrected ILM surface with the intention of increasing the structure-structure correlation with RNFLT.

- **Aim 3: Develop a multimodal graph-based approach to segment the optic nerve head (ONH) structures such as Internal Limiting Membrane (ILM) surface, Bruch's membrane (BM) surface and its opening (BMO) by taking into account the interaction constraints between the structures and the retinal blood vessels prior.** In this aim, a feature-based registration method is proposed in order to register the fundus photographs to the SD-OCT projection images. Furthermore, the retinal vessels prior from fundus photographs is incorporated in a graph-theoretic approach for segmentation of ONH structures. Since the retinal blood vessels presence affects the appearance of ONH structures, incorporating the blood vessel prior in a graph-theoretic approach is beneficial. Furthermore, taking into consideration the interaction between the ONH structures such as BMO and ILM surface can help set up the interaction constraints for the graph-theoretic approach.

1.2 Thesis Overview

This thesis is organized in eight remaining chapters as follows:

- Chapter 2 provides clinical background and motivation behind this work and also information regarding the human retinal structures that are automatically segmented in this research.

- Chapter 3 explains an overview of the graph-theoretic approach utilized in this work and summarizes the previous works for automated segmentation of optic nerve head structures.
- Chapter 4 provides the methods and validation performed for multimodal segmentation of the optic disc and cup from color fundus and SD-OCT modalities.
- Chapter 5 summarizes the results of investigation on computing the rim-width-based parameters in the presence of externally oblique border tissue (EOBT).
- Chapter 6 explains the methods and validation performed for registering fundus (stereo and color photographs) and SD-OCT images using a feature-based registration approach.
- Chapter 7 provides information regarding the methods and validation performed for segmenting the ILM surface from SD-OCT volumes utilizing gradient vector flow field.
- Chapter 8 includes a machine-learning graph-based approach for 3D segmentation of BMO from SD-OCT volumes and the validation performed for evaluating the proposed method.
- Chapter 9 concludes the remarks of this work and provides possible future directions of the research.

CHAPTER 2
CLINICAL BACKGROUND

In this chapter a brief explanation about glaucoma and the structural changes caused due to this disease is provided. The subjects in this work come from glaucoma studies and our methods will be applied and evaluated on the patients showing varying stages of glaucoma.

2.1 Glaucoma

Fig. 1.1a is a view of retina from an ophthalmoscope that ophthalmologists use to look into the eye. According to [47, 48], glaucoma is among the major causes of blindness worldwide and 1–2% of people in the United States become affected by this disease. In 2020, approximately 80 million people will be affected by glaucoma due to the aging population [49]. One of the symptoms of glaucoma is the increased intraocular pressure (IOP). However, the recent studies have showed that the increased IOP might not be present in the initial stages of glaucoma. The glaucoma damages mostly affect the peripheral vision and because of that the patient often does not notice it until significant damage has occurred. The treatment can prevent permanent vision loss if the disease is diagnosed in the early stages.

While visual field tests are the clinical standard for monitoring functional deficits, structural imaging modalities, such as color (stereo) fundus photography and, more recently, spectral-domain optical coherence tomography (SD-OCT) [50], are also important to monitor the optic nerve cupping and other structural changes that are characteristic of this progressive disease. For example, one structural parameter of interest is the cup-to-disc ratio (CDR), which is defined as the cup area over the optic disc area. A larger CDR is associated with glaucomatous damage because of the presence of fewer remaining nerve fiber bundles in the neuroretinal rim (Fig. 2.1). Structurally, glaucoma causes the thinning of the retinal nerve fiber layer (RNFL) and the ganglion cell layer (GCL) thicknesses. Correspondingly, Bruch's membrane

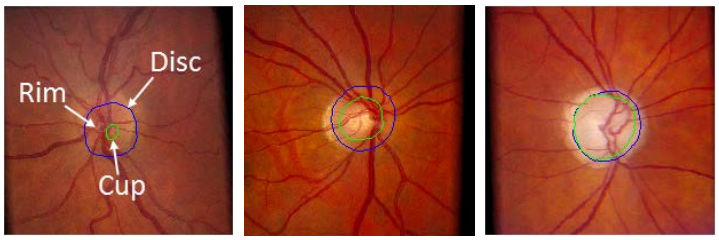

(a) (b) (c)

Figure 2.1: Cupping causes an increase in cup-to-disc ratio (CDR). (a) CDR = 0.15, (b) CDR = 0.46, (c) CDR = 0.84.

opening-minimum rim width (BMO-MRW) which is measured as the minimum Euclidean distance between the BMO and the ILM surface is smaller in glaucoma patients due to the loss of neuroretinal rim tissue. Quantitative measurements from SD-OCT volumes have shown that the RNFL thickness in glaucoma patients is significantly thinner in comparison with normative data, which can be used in diagnosing the disease [29,51–53]. Furthermore, it has been shown that there is a significant correlation between the RNFL thickness (RNFLT) measured along the tracts of fiber bundle and the neuroretinal rim thickness and the peripapillary RNFLT [54, 55].

2.2 Retinal and Optic Nerve Head Structures

The retina is a thin layered structure approximately 250 μm thick [56] and lines the back of the eye. The circular to oval shape with white structure (as visible from a fundus photograph) measuring about 2×1.5 mm across in the center of the retina is the optic disc. The major retinal blood vessels radiates from the optic disc (aka optic nerve head). The fovea, the center of macula, is a blood vessel-free reddish spot located in approximately two and half disc diameters away from the optic disc. The optic disc contains the incoming blood vessels that vasuclarize the neurons and retinal layers as well as the ganglion cell axons running to the brain. Inside the retina, the visual input is transformed to electrical signals that are transmitted to

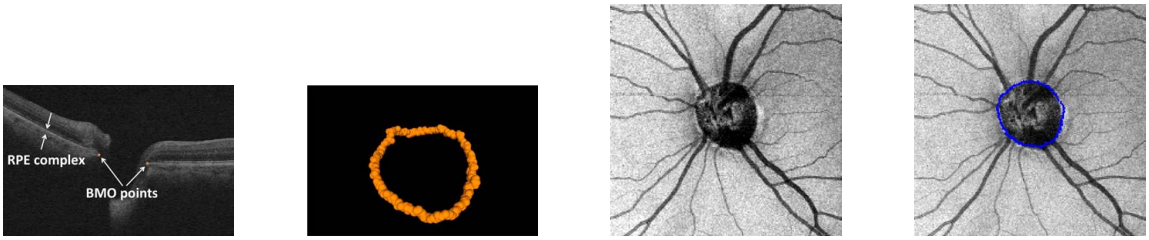

(a) (b) (c) (d)

Figure 2.2: Bruch's membrane opening (BMO) within an SD-OCT volume. (a) An SD-OCT B-scan with BMO points marked with two filled circles. RPE = retinal pigment epithelium. (b) 3D view of all BMO points for the entire SD-OCT volume. (c) SD-OCT projection image. (d) Projected view of BMO points on SD-OCT projection image.

the visual cortex in the brain via neurons passing through the optic nerve. The retinal photoreceptors at the back of the retina absorb photons resulting in stimulating interneurons that relay signals to the retinal ganglion cells. The ganglion cell nerve fiber axons exit the eye on the way to the brain through the optic nerve head. The optic nerve head is free of any photosensitive cells resulting in being insensitive to light and is called the *blind spot*. Unlike a CCD chip with regularly spaced pixels, the retinal photoreceptor mosaic is an inhomogeneous distribution of cone and rod photoreceptors with various sizes [56]. The most central retina is responsible for sharp vision as it is dominated with cone photoreceptors with a cone density peak at the fovea whereas the periphery is dominated by rod photoreceptors.

2.2.1 Optic Nerve Head

The neural canal opening (NCO) also is referred in the literature as Bruch's membrane opening (BMO) (see Fig. 2.2), and is a 3D planar structure [57] that occurs at the level of the retinal pigment epithelium (RPE) and the Bruch's membrane which is also the anatomic entrance to the neural canal. The Bruch's membrane is the anterior surface of the choroid and the BMO is the location at which the optic

nerve passes through this membrane. There is some ambiguity about whether these separate structures can truly be discerned in SD–OCT images obtained from human subjects particularly when there is a externally oblique border tissue (EOBT) [19] as will be discussed further in Chapter 5. There is no evidence for BMO change due to glaucoma in primates and this structure has been used as a stable reference plane from which structural measurements were made in histomorphometric reconstructions of primate eyes [58, 59]. These studies encourage the use of this structure for the detection and tracking of glaucoma in human subjects as well as computing quantitative structural measurements such as BMO–minimum rim width (BMO–MRW) and BMO–horizontal rim width (BMO–HRW).

2.2.2 Intraretinal Layers

The eye structure as well as intraretinal layers of the retina are shown in Fig. 2.3a. Glaucoma causes changes in the intraretinal as well. Specifically, the ganglion cell and nerve fiber bundle layers become thinner due to the death of ganglion cells and loss of nerve fibers. The intraretinal layers are explained as below:

- Inner Limiting Membrane (ILM) surface: located at the boundary of retina and the vitreous body.
- Retinal Nerve Fiber Layer (RNFL): contains the ganglion cells axons which form the optic nerve.
- Ganglion Cell Layer (GCL): consists of the nuclei of ganglion cells.
- Inner Plexiform Layer (IPL): contains axons of bipolar and amacrine cells as well as the ganglion cells dendrites.
- Inner Nuclear Layer (INL): contains the nuclei of horizontal, bipolar, amacrine and Müller cells.
- Outer Plexiform Layer (OPL): consists of photoreceptor axons, and dendrites of horizontal and bipolar cells.

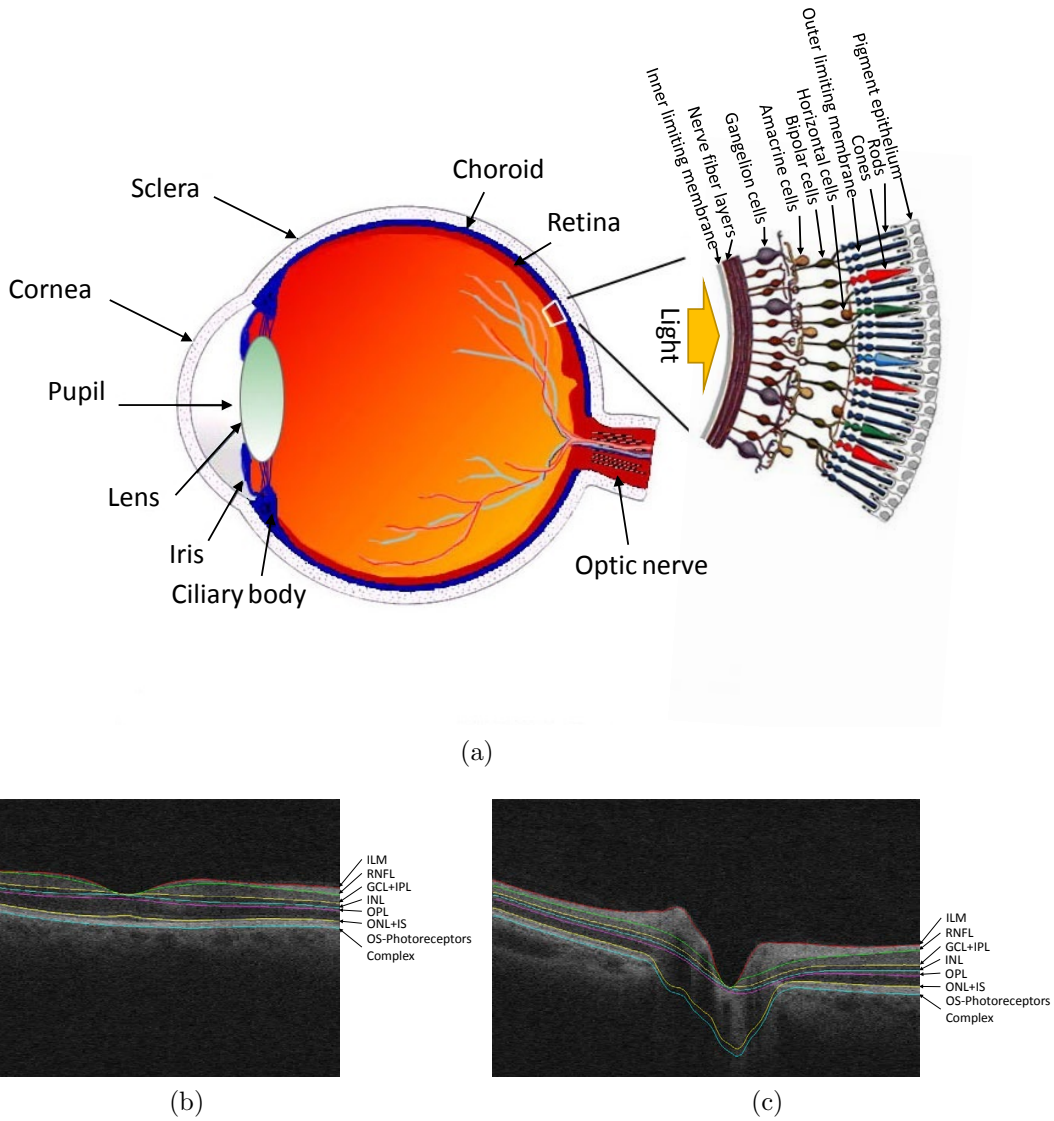

Figure 2.3: Eye structure and intraretinal layers [60] (a) and a segmentation example of intraretinal layers on a central xz–slice from a macular SD-OCT volume (b) and a ONH SD-OCT volume (c).

- Outer Nuclear Layer (ONL): consists of the cells bodies of the both rods and cones photoreceptor cells.
- External Limiting Membrane (ELM): separates the inner and outer segments of the photoreceptors.
- Photoreceptor Layer: consists of the segments of rods and cones photoreceptors and can be divided into two layers of the inner segments (IS) and the outer segments (OS).
- Retinal Pigment Epithelium (RPE) layer: a single layer of cells located between the retina and the choroid.

CHAPTER 3
TECHNICAL BACKGROUND

In this section the previous contributions to the area of segmentation of the ophthalmic structures from SD-OCT volumes are briefly described. Since in this work, a graph-theoretic approach is used in the research aims extensively for segmenting the retinal structures (Chapter 4 and 8 for finding the 2D location of BMO points and Chapter 7 for segmenting the 3D ILM surface), this approach will be explained in more detail.

By advancing the technology in the imaging modalities and moving from the time domain-OCT (TD-OCT) to the spectral domain-OCT (SD-OCT) also called Fourier domain-OCT (FD-OCT) [61–63], developing reliable automated methods to quantitatively measure the retinal properties has attracted attentions in the field of ophthalmic image analysis. For instance, Zeiss Cirrus OCT (Carl Zeiss Meditec, Dublin, CA) enables the acquisition of an ONH volume with a resolution of $200 \times 200 \times 1024$ voxels, covering $6 \times 6 \times 2$ mm^3 of retina in the physical domain in only about two seconds. Some of the inherent challenges in the analysis of SD-OCT volumes include [64]: 1) presence of speckle noise which is an intrinsic characteristic of coherent images and degrades the quality of the SD-OCT scans and also makes the intraretinal boundaries a bit fuzzy. 2) Signal attenuation at deeper retinal structures. The intensity of each voxel in SD-OCT volumes is created by comparing the reflected light from the tissue and the light source. Deeper structures have weaker reflections due to the fact that penetration of light to the deeper structure is more difficult, causing voxels with lower intensity in SD-OCT volumes. 3) Presence of motion artifact due to the eye movement. Despite the fact that the OCT modality is a relatively fast imaging modality, however, the patient eyeball can possibly move or trembles during the scanning which causes a shift of a few successive B-scans in the same direction. 4) Presence of retinal blood vessels which appear as shadows in SD-OCT volumes. These shadows can ob-

scure the retinal layers and other structures, specifically around the ONH, and cause the segmentations to fail locally.

3.1 Previous Work

In this section a summary of previous attempts for segmenting the ONH structures (optic disc, cup, and BMO) as well as intraretinal layers is presented. Additionally, the works that have been accomplished for registering retinal images are briefly discussed. The quantity and variety of approaches that have attempted to segment the intraretinal layers from SD-OCT volumes and optic disc and cup from fundus photographs are more than the number of works on segmenting the optic disc, cup as well as BMO from the SD-OCT modality. The reason is that SD-OCT is a newer modality and BMO-based structural parameters have been recently introduced [2, 3, 3–6].

3.1.1 Segmenting the ONH Structures

ONH structures such as the optic disc and cup play important role in diagnosing glaucoma. Many attempts have been completed in order to automatically segment these structures of interest. More specifically, the prior fundus-only approaches include pixel-based classification methods to segment the optic disc and cup, where a set of features, corresponding to each pixel, are extracted to be used for training a classifier and then the trained classifier is tested on the unseen data [7, 8]. Model-based approaches [9–12] are another well-known group where an optic disc model, which is created from a training set, tries to fit to the testing data. Zheng *et al.* [15] proposed the use of graph–cut for segmenting the optic disc and cup boundaries. Merickel *et al.* [13, 14] utilized theoretical graph-based approaches in their method where the images sampled in the radial direction and the segmentation was done in the radial domain. While the classification-based method and graph-cut methods suffer from not having well-defined boundaries due to the pixel-based labeling, model-based methods and the graph-based method proposed by Merickel *et al.* do not have such

a problem. However, there are limitations for the active contour methods where they need to have a good estimation of the location of object so that the contour can fit to the target otherwise they fail to segment the object. Despite all the works that have been accomplished, segmentation of optic disc and cup boundaries from fundus photographs is still a challenging task. In fact, the high inter-observer variability of manual segmentation of the optic disc and cup boundaries shows the difficulty of the task [18].

Initial SD-OCT-only approaches include that of Lee *et al.* [16] and Abràmoff *et al.* [17] where a pixel-based classification method for segmenting the boundaries is used. In their methods, a set of features were extracted from SD-OCT volumes and their methods were evaluated based on a fundus-based reference standard. Hu *et al.* [18] used a theoretical graph-based method to find the 2D projections of NCO (aka BMO), however, the evaluation of their work was done using a fundus-based reference standard. Although, the theoretical graph-based method has the ability to well-define the boundaries, it requires having a set of suitable cost functions corresponding to the boundaries of interest, which means the quality of the results depends on the quality of the cost functions. More recently, Antony *et al.* [24] proposed an iterative graph-based approach for segmenting surfaces sharing a common hole. They used the proposed method to segment the BMO (as the shared hole) and the surrounding surfaces.

3.1.2 Segmenting the Intraretinal Structures

The early attempts were mostly 2D methods [25–33]. In these approaches, the surface between the inner and outer segments of photoreceptors was used to flatten the volume (adjusting A–scans in the z–direction) and the reason is that there is a large gradient at the location of this surface which makes it easier to segment. Then, using 2D information, the edges in each A–scan was detected to find the entire surface. Use of an iterative method to refine the result at each iteration [31], Markov model to

correct the segmentation errors at the location of detected peaks [65], polynomial line fitting and statistical regression [66], and Canny edge detection [67] are additional features to this schema that tried to improve the segmentation results.

Another group of people who tried to segment the intraretinal layers used a machine learning based approach in which appropriate features are extracted from the different layers to train a classifier and then the intraretinal layers are segmented using the trained classifier. K–means clustering was used in Rossant *et al.* [35] to segment the inner retinal layers. Before segmenting the inner retinal layers, using peak detection in edge profiles, the ILM and IS/OS surfaces are segmented with this assumption that each slice is centered on the macula so that they can correct the errors that occurs at the fovea. Zawadzki *et al.* [34] trained an SVM classifier using user input to find the region of interest in SD-OCT images. They tested their method on various normal and diseased scans. Vermeer *et al.* [36] proposed training the SVM classifier using a Haar-like features derived from each A–scan on the manually traced scans. The final result was obtained by applying a post-processing step which involves surface smoothness constraints.

Employing active contours is another approach to the problem where shape priors as well as edge gradients and local information are incorporated in the method. Mujat *et al.* [68] segment the RNFL by minimizing an energy function using a filtered image and gradient information which makes their method robust to speckle noise. Yazdanpanah *et al.* [38] approached the problem by relying on regional information rather than the edge features. One limitation to their approach is use of a circle as the shape prior and the assumption of segmenting smooth-arc like structures specially in processing of diseased scans. Kajic *et al.* [40] used an active appearance model (AAM) for segmentation of retinal surfaces where a large dataset is needed for creating the proposed model. Rathke *et al.* [39] proposed the use of probabilistic principal component analysis (PPCA) to estimate an appearance model as well as the

global shape and the variations along each column. The method, however, is designed for 2D circular scans and the extension to 3D is far from trivial.

Dynamic programing and shortest path algorithms are among graph-based approaches that have been employed for intraretinal layer segmentation. Yang *et al.* [41] proposed a 2D dynamic programming shortest path method for segmentation of the intraretinal layers. The cost of each node comes from the gradient maps created by Canny edge detector where each surface had a corresponding threshold values. This approach uses neither the 3D contextual information nor the regional or shape information. Chiu *et al.* [42,43] utilized Dijakstra's shortest path algorithm to segment the intraretinal surfaces where the starting and ending points of each surface are obtained through an initialization step. This method is also a 2D approach that obtains the 3D surface segmentation by stitching the 2D segmentations of B–scans.

The first "true 3D" approach for segmenting the intraretinal surfaces was proposed by Garvin *et al.* [44] where the graph-theoretic approach [69, 70] described in section 3.2 was applied to simultaneously segment the intraretinal surfaces from macular SD–OCT volumes. The proposed method formulated the segmentation of multi–surface problem as an optimization problem where the goal was finding a minimum–cost closed set of nodes with respect to the provided cost functions and satisfying the feasibility constraints. The feasibility constraints include the surface interaction constraint and the smoothness constraints. There are two types of cost functions, the first one is the on–surface cost function which was obtained by performing directed gradients and the second one is the in–region cost function which is computed using a fuzzy membership function which assigned each voxel the unlikeness of belonging to particular regions. The solution to the graph is computed using the maximum-flow theorem which has a polynomial running time. This method could be extended for finding surfaces simultaneously in higher dimensions. The smoothness constraint enables the graph structure to incorporate "true 3D" contextual information and the

surface interaction constraint controls the "shape" of the surfaces with respect to neighboring surfaces.

Lee *et al.* [16] later introduced a faster version of this method by performing the graph-theoretic approach in multiple resolutions. This method also was employed to segment the intraretinal surfaces in ONH–centered SD–OCT scans [16, 46] and fundus photographs structures [71]. The cost functions used in these works were designed mostly by hand and learned features were incorporated slightly. Besides in the opthalmology area, the graph-theoretic approach was also employed to segment structures in CT [72,73] as well as MR [74,75] images where shape priors and texture also were incorporated in the method. Song *et al.* [45,76] proposed the incorporation of learned shape and context priors which influenced the topology of surfaces significantly. Shape prior is responsible for penalizing the local shape changes whereas the context prior penalizes the change from the expected surface distances. Adding the prior information's terms to the graph-theoretic algorithm generates a more robust approach. Antony et al [77] proposed that instead of using hand-designed cost functions needed for the graph-theoretic approach, to compute the cost functions using a machine-learning method.

3.1.3 Retinal Image Registration

Image registration is an essential step in many medical imaging applications from different areas such as radiology, neurology, and opthalmology. The registration approaches either find a set of corresponding points between the images or benefit from the pixel/voxel intensities and try to align the images (of the same or from different modalities) using different transformations such as rigid, affine, polynomial or more sophisticated transformations such as nonlinear and deformable techniques. Similarly, the previous works in the retinal image registration area are applied to images from the same or different modalities. The imaging techniques include a variety of modalities such as color fundus, stereo fundus, fluorescein angiography, infrared, and

OCT modalities.

Researchers have approached the problem of retinal image registration using different directions. Point-based [78,79], intensity-based [80–83], and feature-based [84–86] techniques have been used to register retinal images from different modalities. Each technique has some favorable and the unfavorable factors depending on the application and the imaging dataset for which the method is applied. For instance, the approaches that are proposed to register retinal images from the same modality may not be successful in registering multimodal retinal images. In Chapter 6 we discuss the retinal image registration techniques in more detail and propose a multimodal feature-based registration method using histogram of oriented gradients (HOG).

3.2 Graph-Theoretic Approach

Li *et al.* [70] proposed a graph-theoretic approach capable of segmenting multiple interacting surfaces simultaneously. They transfered the segmentation problem into an optimization problem with the goal of finding a minimum-cost closed set of nodes in a graph. The problem of finding a minimum-cost closed set is transferred into a maximum-flow problem where the global optimal solution is obtained using a minimum s–t cut. Two important components of this method are the feasibility constraints (*hard* and *soft*) which control the shape of surfaces and the cost functions which include the unlikeliness of a voxel belonging to a specific region (in-region cost function) and locating on a specific surface (on-surface cost function).

3.2.1 Feasibility Constraints

Consider a volumetric image described as $\mathcal{I}(x, y, z)$ with dimensions $X \times Y \times Z$, and the surface $\mathcal{S}_i$ can be defined as a function $\mathcal{S}_i(x, y)$ mapping (x, y) pairs to their z–values where $x \in \{0, 1, \cdots, X-1\}$, $y \in \{0, 1, \cdots, Y-1\}$, and $z \in \{0, 1, \cdots, Z-1\}$. The surface $\mathcal{S}_i$ intersects only one voxel of each column, parallel to the z–axis (e.g. an A-Scan in a SD-OCT volume) and spans the entire $x \times y$ domain. Originally

[69, 70], the smoothness constraint represented the maximum change in z-position allowed in the x–direction Δ_x and in y–direction Δ_y. In other words, if $\mathcal{I}(x, y, z_1)$ and $\mathcal{I}(x+1, y, z_2)$ are two adjacent voxels on a surface in the x–direction then $|z_1 - z_2| \leq \Delta_x$. Similarly, for two adjacent voxel on a surface in the y–direction ($\mathcal{I}(x, y, z_1)$ and $\mathcal{I}(x, y+1, z_2)$) we have $|z_1 - z_2| \leq \Delta_y$. Later, Garvin *et al.* [44, 87] proposed a varying smoothness constraint for which the smoothness constraints varied as we move along the surfaces with respect to the (x, y) of each voxel. The varying smoothness constraints when moving from location (x_1, y_1) to (x_2, y_2) can be written as follows:

$$-\Delta^u_{\{(x_1,y_1),(x_2,y_2)\}} \leq \mathcal{S}(x_1, y_1) - \mathcal{S}(x_2, y_2) \leq \Delta^l_{\{(x_1,y_1),(x_2,y_2)\}}, \tag{3.1}$$

where, $\Delta^u_{\{(x_1,y_1),(x_2,y_2)\}}$ and $\Delta^l_{\{(x_1,y_1),(x_2,y_2)\}}$ are the smallest and largest permitted change in the z–direction, respectively.

The second feasibility constraint, the surface-interaction constraint, represents the relationship between surfaces such as the minimum distance $\delta^l_{i,j}$ and the maximum distance $\delta^u_{i,j}$ between surface $\mathcal{S}_i$ and surface $\mathcal{S}_j$ as well as the order of the surfaces (e.g. which surface is above the other one). The original definition [70] of the surface-interaction constraint was constant values for each pair of adjacent surfaces but similar to smoothness constraint it can be defined as a varying constraint (i.e. a function of location (x, y)) [44, 87]. The varying surface-interaction constraint for surface $\mathcal{S}_i$ and surface $\mathcal{S}_j$ with the assumption that surface $\mathcal{S}_i(x, y)$ is above $\mathcal{S}_j(x, y)$ can be written as follows:

$$\delta^l_{i,j}(x, y) \leq \mathcal{S}_i(x, y) - \mathcal{S}_j(x, y) \leq \delta^u_{i,j}(x, y), \tag{3.2}$$

Song *et al.* [76] proposed a method to further incorporate the shape prior in the surface smoothness constraints. Previously, there were only feasible or non-feasible surfaces and the method did not grant the penalty of the deviation inside the allowed

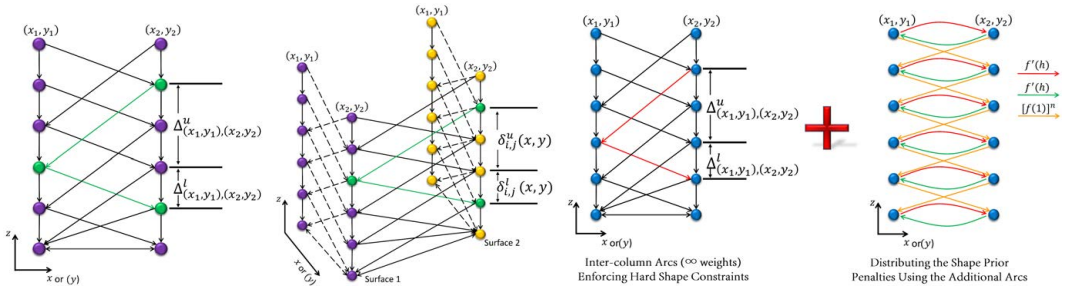

Figure 3.1: Feasibility constraints. (a) Varying smoothness constraints Δ^u and Δ^l. (b) Varying surface-interaction constraints δ^u and δ^l. (c) Soft smoothness constraints to incorporate shape priors.

constraints. In the Song *et al.* proposed method, an additional soft constraint based on some given shape prior is included. A convex function $f(h)$ penalizes the cost of the surface set if the change of the surface is deviated from the expected shape (i.e. the mean shape). If the shape prior between two adjacent columns (x_1, y_1) and (x_2, y_2) on surface $\mathcal{S}_i(x, y)$ is $m_{(x_1,y_1),(x_2,y_2)}$ the cost of the shape term can be written as:

$$C_{Sp_i} = \sum_{\{(x_1,y_1),(x_2,y_2)\in\mathcal{N}_c\}} f(\mathcal{S}_i(x_1, y_1) - \mathcal{S}_i(x_2, y_2) - m_{(x_1,y_1),(x_2,y_2)}) \tag{3.3}$$

where $\mathcal{N}_c$ reflects a set of neighboring columns. In order to add the additional soft constraint to the constructed graph, additional arcs need to be added. Here for simplicity and without loss of generality we only consider the x-direction. Assume that the smoothness constraint in the x-direction is Δ_x and the mean shape prior $m_(x_1, x_2)$ for two adjacent column x_1 and x_2 on a feasible boundary $\mathcal{S}(x)$ is given. The shape penalties are only imposed when $\mathcal{S}(x_1) - \mathcal{S}(x_2) \neq m_{(x_1,x_2)}$. Let $h = \mathcal{S}(x_1) - \mathcal{S}(x_2) - m_{x_1,x_2}$ therefore, the shape prior penalty is $f(h)$. The discrete second and first derivative of the convex function can be expressed as $[f(h)]'' = [f(h+1) - f(h)] - [f(h) - f(h-1)]$ and $[f(h)]' = f(h+1) - f(h)$, respectively. The feasibility

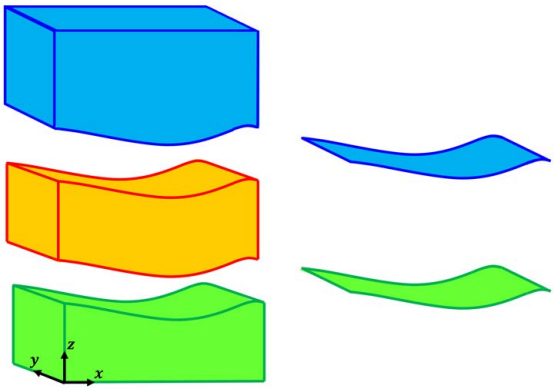

Figure 3.2: Illustration of total cost of segmenting two non-intersecting surfaces (where only hard constraints included) including three in-region (left) and two on-surface (right) costs.

constraint will be $-\Delta_x < h < \Delta_x$ and for each feasible h that satisfies $[f(h)]' \geq 0$ an arc with a weight of $[f(h)]''$ is added from $node(x_1, z)$ to $node(x_2, z - m_{(x_1,x_2)} - h)$. Similarly, for the feasible h with $[f(h)]' < 0$ an arc is added from $node(x_2, z)$ to $node(x_1, z + m_{(x_1,x_2)} + h)$ with a weight of $[f(h)]''$. Fig. 3.1 illustrates the hard and soft smoothness constraints.

3.2.2 Cost Function Computations

A minimum-cost closed set of nodes (i.e the minimum cost of the feasible surfaces) is obtained with respect to cost functions and soft constraints-related costs. Originally [70] the cost function was derived from directed gradients of the volumes making it an edge-based cost function. Later a cost function consisting edge-based and region-based cost functions was proposed [44, 87]. The edge-based cost function called *on-surface* cost function reflects the unlikelihood of a voxel locating on a specific surface. For surface $\mathcal{S}_i(x, y)$, the on-surface cost function be expressed as $C_{\mathcal{S}_i(x,y)} = \sum_{\{(x,y,z)|z=\mathcal{S}_i(x,y)\}} \mathcal{I}_{c_{\mathcal{S}_i}}(x, y, z)$ (Fig. 3.2).

The region-based cost function called *in-region* cost function represents the unlikeliness of a voxel belonging to a specific region. Consider a region $\mathcal{R}_i$, the in-region cost

can be described as $C_{\mathcal{R}_i} = \sum_{(x,y,z)\in\mathcal{R}_i} \mathcal{I}_{c_{\mathcal{R}_i}}(x,y,z)$. When there exists n non-intersecting surfaces the volume will be divided into $n+1$ regions (Fig. 3.2). Therefore the total cost C_T of n surfaces can be written as

$$\begin{aligned} C_T &= C_{\{\mathcal{S}_1(x,y),\ldots,\mathcal{S}_n(x,y)\}} + C_{\{\mathcal{R}_0,\ldots,\mathcal{R}_n\}} \\ &= \sum_{i=1}^{n} C_{\mathcal{S}_i(x,y)} + \sum_{i=0}^{n} C_{\mathcal{R}_i} \end{aligned} \tag{3.4}$$

The penalties induced by the soft smoothness constraint can be added to the total cost induced by the cost functions C_T. Therefore, the total cost C_{Total} can be computed as

$$\begin{aligned} C_{Total} &= C_{\{\mathcal{S}_1(x,y),\ldots,\mathcal{S}_n(x,y)\}} + C_{\{\mathcal{R}_0,\ldots,\mathcal{R}_n\}} + C_{\{\mathcal{S}_{Sp_1},\ldots,\mathcal{S}_{Sp_n}\}} \\ &= \sum_{i=1}^{n} C_{\mathcal{S}_i(x,y)} + \sum_{i=0}^{n} C_{\mathcal{R}_i} + \sum_{i=1}^{n} C_{\mathcal{S}_{sp_i}}. \end{aligned} \tag{3.5}$$

CHAPTER 4
MULTIMODAL SEGMENTATION OF OPTIC DISC AND CUP FROM SD-OCT AND COLOR FUNDUS PHOTOGRAPHS USING A MACHINE-LEARNING GRAPH-BASED APPROACH

The content of this chapter is presented in [22,88,89]. As mentioned in Chapter 2, the characteristic structural changes that are caused due to glaucoma are monitored via structural imaging modalities such as color (stereo) fundus photography and SD-OCT. Cup-to-disc ratio (CDR) is a structural parameter that helps with diagnosing glaucoma and is obtainable from both color fundus photographs and SD-OCT volumes. Most prior optic disc and cup segmentation approaches have focused on segmenting color fundus images alone [7–15], with few approaches having been presented for the segmentation within SD-OCT volumes alone [16–18]. More specifically, the prior fundus-only approaches for segmenting the disc and cup include pixel-based classification methods [7, 8], model-based approaches [9–12], and graph-based approaches [13–15]. Initial SD-OCT-only approaches include the work of Lee *et al.* [16] and Abràmoff *et al.* [17] where each A-scan (i.e., projected pixel location) was classified as cup, rim, or background from SD-OCT features within the A-scan. While the final approach was an SD-OCT-only approach, the pixel-classification-approach was trained and tested using expert-marked color fundus images.

Another type of SD-OCT approach has focused on directly segmenting the termination of Bruch's membrane at the optic nerve head within SD-OCT volumes using a graph-based approach [18]. Anatomically, it was originally assumed that the projected location of the BMO would coincide with that of the clinical disc margin visible in a color fundus photograph. (In fact, the automated BMO segmentation work [18] was evaluated via comparisons with the clinical disc margin from color fundus photographs.) While it has been found that the projected location of the BMO often does indeed closely coincide with the clinical disc margin, differences do exist, such as in the presence of externally oblique border tissue [18–21], challenging the

original anatomical assumptions behind the fundus-based clinical disc margin. Correspondingly, when available, the BMO (or, more precisely, the projected BMO for computation of 2D parameters) is becoming recognized as an appropriate disc margin definition.

While SD-OCT-only approaches have been shown to outperform fundus-only approaches [7, 88] (in part due to their ability to provide 3D information of anatomic landmarks such as the BMO) for the segmentation of the disc and cup, the color information and higher resolution in the en-face (i.e., projected plane) in color fundus photographs (6–10 microns in fundus photographs versus 30–100 microns spacing between A-scans of SD-OCT volumes) provides complementary information to help localize such structures. Given that both fundus and SD-OCT images are often acquired for the assessment of glaucoma and with existence of fundus-OCT image-registration algorithms [90–93], it makes sense to combine the complementary information from both sources for the segmentation of the disc and cup. Use of multimodal information is further justified via prior work in the multimodal segmentation of the retinal blood vessels by Hu *et al.* [93], where it was shown that approaches that combined the use of fundus and SD-OCT information outperformed SD-OCT-only approaches.

Correspondingly, the purpose of this chapter is to develop a multimodal approach that utilizes information from both SD-OCT volumes and color fundus photographs to segment the disc and cup. In particular, after fundus-to-OCT image registration, our approach uses a machine-learning strategy to compute the likelihood of each projected pixel belonging to either cup or rim or background classes (from multimodal features) and the likelihood of belonging to the projected BMO boundary locations (from SD-OCT features). These in-region and disc-boundary likelihoods are then used as part of the cost functions in an optimal graph-based approach to simultaneously find the disc and cup boundaries. A preliminary version of our multimodal region-based-classification-only results were presented in [88], but we did not use a

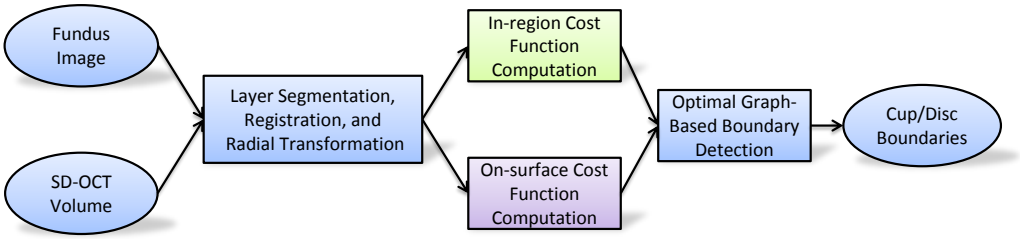

Figure 4.1: Flowchart of overall method.

graph-based strategy to find the final boundaries and did not compute the BMO boundary likelihoods. Furthermore, to reflect our updated understanding of the best reference to use for the disc margin, the projected location of the BMO is used as the disc margin reference standard for training/testing in this work rather than the disc margin marked from color fundus photographs. The expert-marked cup boundary from fundus photographs is still used as the reference standard for the cup.

4.1 Methods

An overall flowchart for the proposed method is shown in Fig. 4.1. The four major components are as follows: 1) a preparation step including SD-OCT intraretinal layer segmentation, fundus-to-OCT registration, and radial transformation (Section 4.1.1), 2) in-region cost function computation (Section 4.1.2), 3) disc-boundary cost function computation (Section 4.1.3), and 4) optic disc and cup boundaries segmentation using a theoretical graph-based approach (Section 4.1.4). The in-region and disc boundary cost functions contain the information regarding the likelihood of a pixel belonging to each region (cup, rim, and background) and disc boundary, respectively. Both the in-region and disc-boundary cost functions are created using a machine-learning approach. Features used for in-region cost function computation come from both modalities (a multimodal feature set) and features for the disc-boundary cost function computation are extracted from SD-OCT volumes only. The likelihood maps that are

computed, as described in more detail in Sections 4.1.2 and 4.1.3, are then utilized in the theoretical graph-based approach described in Section 4.1.4 to find the globally optimal (with respect to the cost functions) boundaries of the optic disc and cup.

4.1.1 Intraretinal Layer Segmentation, Registration, and Radial Transformation

The first part of the proposed method includes several steps in preparation for the extraction of features from two modalities for use in the machine-learning cost-function design steps.

4.1.1.1 Intraretinal Layer Segmentation

The intraretinal surfaces are first segmented within the 3D SD-OCT volumes (Fig. 4.2) using the theoretical multi-resolution graph-based approach [16, 44] explained in Chapter 3. The surfaces are segmented to: (1) enable the creation of a 2D SD-OCT projection image to be used for fundus-to-OCT image registration, and (2) to enable layer-based features to be extracted. Three surfaces are used for further computations (although eleven surfaces are originally segmented). The first surface corresponds to the Internal Limiting Membrane (ILM). Surface two is the junction of the inner and outer segments of photoreceptors (IS/OS), and surface three is the outer boundary of the Retinal Pigment Epithelium (RPE), also called the Bruch's membrane surface. Using the method described in [44] a thin-plate spline is fitted to the the third surface in order to flatten the OCT images and to enable a consistent optic nerve head shape across patients. Afterwards, an SD-OCT projection image is created by averaging the voxel intensities in the z-direction between the IS/OS junction and Bruch's membrane surfaces.

4.1.1.2 Registration

In order to benefit from the complementary information of both modalities at a pixel/A-scan level, registration needs to be performed. The 2D projection image

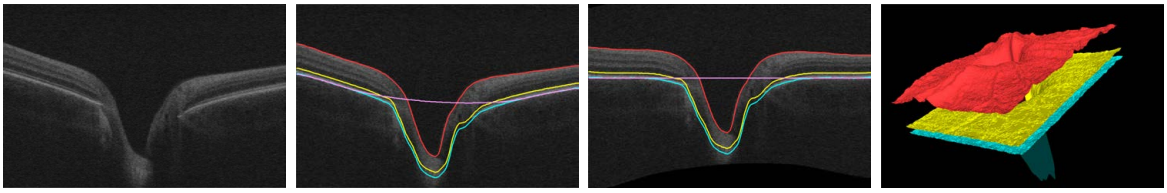

(a) (b) (c) (d)

Figure 4.2: An example of a central B-scan of an SD-OCT volume and intraretinal layer segmentation. (a) The original OCT B-scan. (b) Segmented three layers: the first surface is the ILM (red), the second surface (yellow) is the IS/OS junction, and the third surface (blue) is the lower bound of RPE complex. The pink surface indicates the thin-plate spline fitted to the third surface. (c) Flattened OCT B-scan along with surfaces. (d) 3D view of the three surfaces.

obtained from the 3D SD-OCT volume (Section 4.1.1.1) is utilized to register the 2D fundus photograph to the SD-OCT projection image (Fig. 4.3). The registration is performed on the fundus and the SD-OCT projection vessel maps. A pixel classification based vessel segmentation algorithm is used to obtain the vessel probability maps of fundus photographs [94] and SD-OCT projection images [95]. The fundus image vessel map is subsampled using linear interpolation so that the optic disc is about the same size in both images. Next, a skeletonization algorithm is applied to the binary vessel segmentations to obtain the vessel centerlines. All centerline pixels with more than two neighbors are removed to obtain a set of vessel segments. An Iterative Closest Point (ICP) algorithm [96] is then applied in two phases: a first rough initial alignment and a second fine alignment. The rough initial alignment is performed using the simulated annealing optimization algorithm [97]. The finer alignment is performed using the Powell optimization algorithm [98]. The cost function, F, in (4.1) below for both these steps is the same and consists of the distance between closest points, d (as in a traditional ICP approach), and additionally the difference between the local vessel orientation in radians between the target and the moving

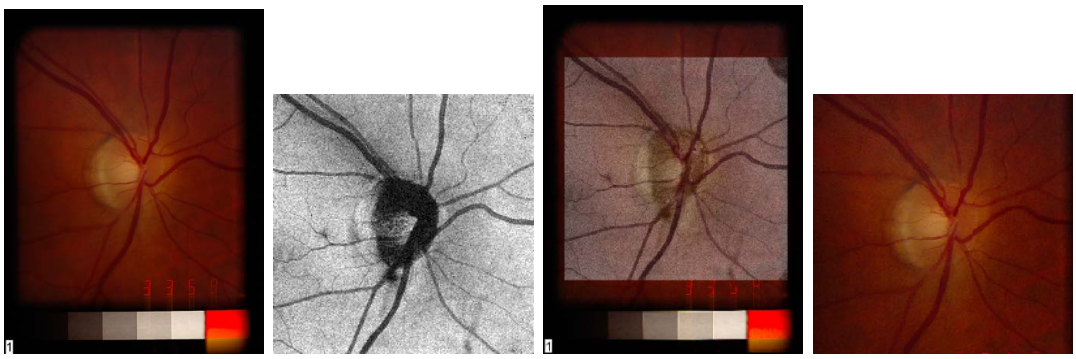

(a) (b) (c) (d)

Figure 4.3: Registration of fundus photograph to projection image of SD-OCT volume. (a) Original fundus photograph. (b) Corresponding projection image of SD-OCT volume. (c) Alignment of fundus photograph to OCT projection image. (d) Registered fundus photograph.

image, d_θ:

$$F = (1 + d) \times (1 + d_\theta) \, . \tag{4.1}$$

The additional term, d_θ, causes the cost function to have a lower value when the centerline pixels are matched and the local orientation of vessels are similar [79].

4.1.1.3 Radial Transformation and Layer Segmentation

As a preliminary step in the creation of the disc-boundary costs (Section 4.1.3), each original SD-OCT volume in the Cartesian domain (xyz) is resampled (with θ-precision = 1°) using bilinear interpolation to create a radial volume ($r\theta z$). With such a transformation, each slice contains two BMO endpoints (whereas in the original volume, BMO points become less obvious in slices approximately tangent to the superior/inferior disc boundary, Fig. 4.4a, and are additionally not present in slices that do not intersect with the disc).

Once the radial scans are created, the same approach as explained in [16] is used to segment the ILM surface, IS/OS junction and RPE-complex lower bound. Since

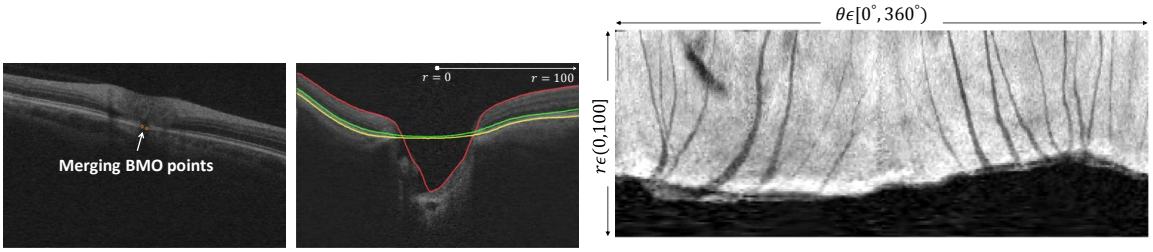

(a) (b) (c)

Figure 4.4: Radial slice segmentation. (a) Example (non-central) scan from original SD-OCT volume demonstrating the how the BMO points may appear close together. (b) Example radial scan (with BMO points appearing as they would in a central scan from the original volume) with segmented surfaces. Interpolation is used to define the second and third surfaces in the neural canal region. (c) The radial projection image.

the RPE-complex ends at the optic disc margin, the RPE layer segmentation inside the optic disc region is not valid. Therefore, an optic disc margin (1.73 mm from the center) which is larger than the typical optic disc size, is assigned to every volume, and within this margin, the second and third surfaces are interpolated (Fig. 4.4b).

A radial projection image (Fig. 4.4c) is then created to reflect the (maximum) intensities of the interpolated RPE-complex surfaces. In particular, for each A-scan, the maximum intensity value in the z-direction 15 voxels above (29.3μm) the second surface and 15 voxels below the third surface is selected and the projection image is reformatted such that radial values (0, 100] appear on the vertical axis and θ values [0°, 360°) appear on horizontal axis. The radial projection image is used in Section 4.1.3.

4.1.2 In-region Cost Function Computation

The flowchart of the algorithm for creating in-region probability maps is depicted in Fig. 4.5. The in-region likelihood maps contain the regional costs associated with each pixel. A lower cost indicates that under feasibility constraints the pixel has

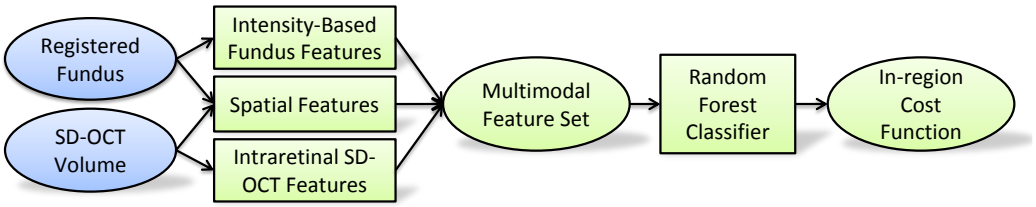

Figure 4.5: In-region cost function design flowchart.

a higher chance to be assigned to the corresponding region. Three in-region cost functions corresponding to three classes of cup, rim, and background are computed by training a random forest classifier [99] using a multimodal feature set.

4.1.2.1 SD-OCT Features

There are eight features extracted for each projected x-y location from SD-OCT volumes (similar to features in [16]). The first one is the intensity of the same projection image used for registering the fundus image to SD-OCT volume. The next features are the average intensities of four subvolumes above the reference spline fitted to the outer boundary of RPE (90-120, 60-90, 30-60, 0-30 voxels above) and the average intensities of two subvolumes below the reference spline (0-30 and 30-60 voxels below). The last feature is the optic disc depth information which is extracted by measuring the distance between the ILM surface and the reference spline. An example set of SD-OCT feature is shown in Fig. 4.6.

4.1.2.2 Fundus Features

As in [7] three intrinsic color channels of red (R), green (G), and blue (B) as well as three color-opponent channels of dark-bright (D-B), blue-yellow (B-Y), and red-green (R-G) are extracted from fundus photographs. The color-opponent channels are computed as in the equations below:

$$I_{\text{dark}-\text{bright}} = \frac{I_{\text{red}} + I_{\text{green}} + I_{\text{blue}}}{3} \tag{4.2}$$

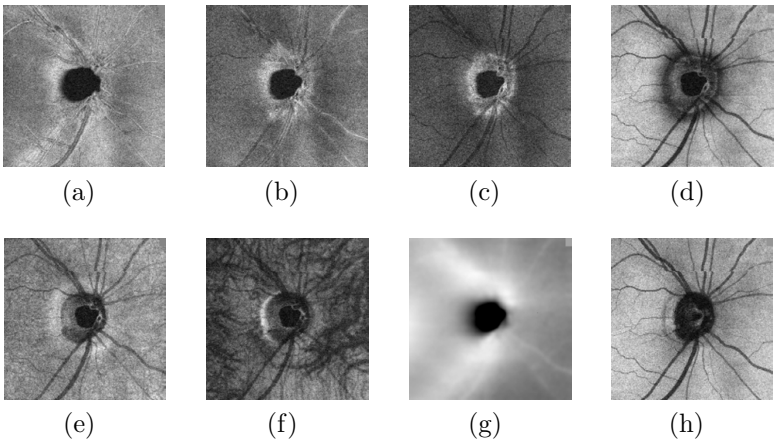

Figure 4.6: OCT features. (a)-(f) Average intensity of subvolumes in z-direction. (g) Distance of first surface to the thin-plate spline fitted to the third surface. (h) The SD-OCT projection image.

$$I_{\text{blue}-\text{yellow}} = I_{\text{red}} + I_{\text{green}} - 2 \times I_{\text{blue}} \tag{4.3}$$

$$I_{\text{red}-\text{green}} = I_{\text{red}} - I_{\text{green}} \tag{4.4}$$

Note that the original use of the color-opponent channels as in [7] is motivated by the theory of color vision [100] where three signals are produced in the retina by three different cone types in response to a light stimulation. These signals are transformed to three opponents before passing to the brain. The first opponent contains illumination information and is achromatic (the "dark-bright" opponent). The other two opponents (the "red-green" and "blue-yellow" opponents) contains color information.

A zero-order Gaussian filter bank (σ=4, 6, 8) is applied to all color channels to extract features in different scales as shown in Fig. 4.7.

4.1.2.3 Spatial Features

In the registered fundus-OCT images, it is more likely that the pixel in the center of the image belongs to optic cup than to rim area or background. Therefore, in order to incorporate the *a priori* expectation of the class of a pixel based on its

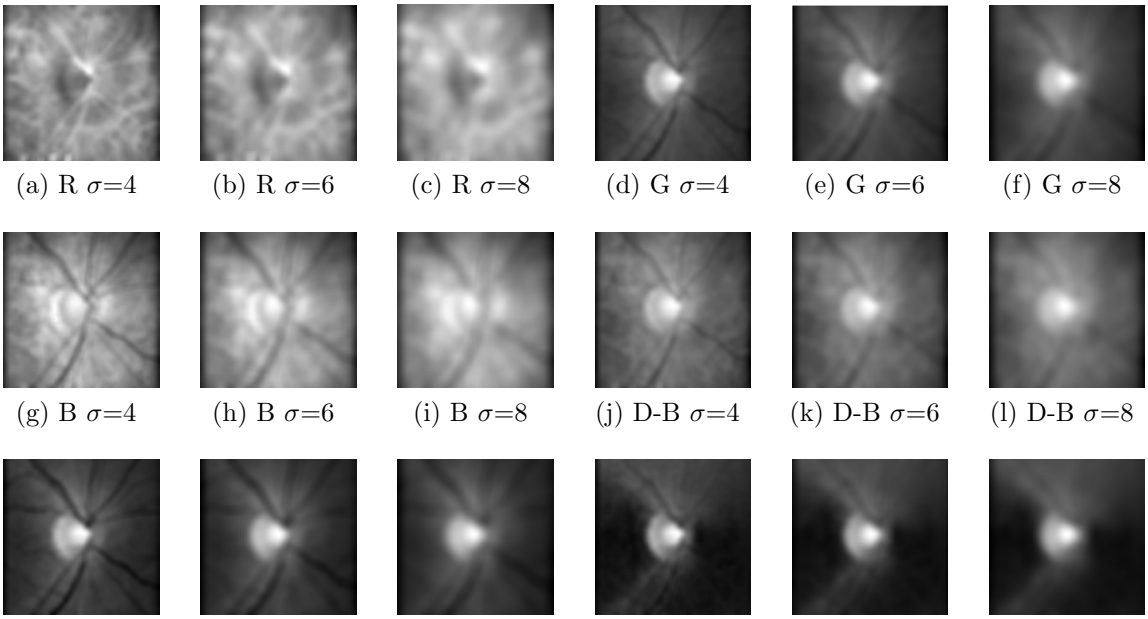

(a) R σ=4 (b) R σ=6 (c) R σ=8 (d) G σ=4 (e) G σ=6 (f) G σ=8

(g) B σ=4 (h) B σ=6 (i) B σ=8 (j) D-B σ=4 (k) D-B σ=6 (l) D-B σ=8

(m) B-Yσ=4 (n) B-Y σ=6 (o) B-Y σ=8 (p) R-G σ=4 (q) R-G σ=6 (r) R-G σ=8

Figure 4.7: Fundus pixel features. From left to right are the filtered image using Gaussian filter bank having sizes σ=4, 6, 8 respectively. (a)-(c) Red channel. (d)-(f) Green channel. (g)-(i) Blue channel. (j)-(l) Dark-bright channel. (m)-(o) Blue-yellow channel. (p)-(r) Red-green channel.

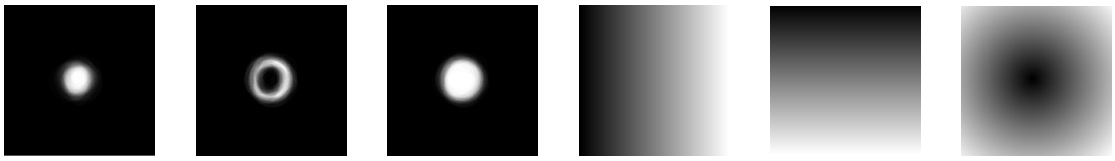

(a) (b) (c) (d) (e) (f)

Figure 4.8: Spatial features. (a)-(c) Three *a priori* maps corresponding to cup, rim, and optic disc regions derived from PCA. (d) Distance of the x position with respect to the optic disc center. (e) Distance of the y position with respect to the optic disc center. (f) Radial distance with respect to the optic disc center.

location in the image, a principal component analysis is performed on all reference standard images in the training set and only the first principal component is kept. The *a priori* expectation of the class maps of the cup and disc are similar to the shapes of 2D Gaussians. An *a priori* map describing the rim area is created by subtracting the *a priori* map of cup from the *a priori* map of optic disc. Three *a priori* maps are shown in Fig. 4.8. In addition to the three *a priori* maps, three optic disc center-based features are extracted. In particular, after defining the lowest point (in the z-direction) of the first intraretinal surface as the center of the optic disc, the distance of the x and y positions, as well as the radial distance of each pixel, are measured with respect to this disc center.

4.1.2.4 Classification

Once the features are extracted from both modalities, a random forest classifier [99] is used to classify each pixel into optic cup, rim, or background. A summary of the 31 multimodal features that are used for training the random forest classifier are listed in Table 4.1.

Random forests are categorized as ensemble classifiers. Once a feature vector is entered to a random forest classifier, all trees (N) in the forest classify the input feature vector based on the specific number (m) of randomly selected features from

Table 4.1: Multimodal feature set used for producing in-region cost functions

Features	Fundus	SD-OCT	Spatial
Features 1-18: Filtered color channels (red, green, blue, dark-bright, yellow-green, and red-blue) using Gaussian zero-order filter bank (σ=4,6,8).	✓		
Feature 19: The pixel intensity in the SD-OCT projection image. The SD-OCT projection image is produced by averaging the voxel intensities between surface two (IS/OS junction) and three (the outer boundary of the RPE) in the z-direction.		✓	
Features 20-25: Average intensities of six subvolumes in the z-direction (120 pixels above and 60 pixels below the fitted reference spline to surface three), each of them representing the average voxel intensity of 30 voxels within the voxel column.		✓	
Features 26-28: Pixel *a priori* expectation map of each class based on pixel location.			✓
Features 29-31: Distance of x and y positions as well as the radial distance of each pixel with respect to the approximate center.			✓

the input feature vector at each decision split. The final classification is determined by taking the majority vote over the entire forest. In addition to robustness, the other advantage of this classifier is the very low number of parameters to be tuned. These are the number of trees in the forest N and the number of features to be randomly selected at each decision split m. Here, we used $N = 500$ trees (larger numbers increased the training time without improving the accuracy) and $m = 10$.

The likelihood map of each class at a pixel is computed by dividing the number of trees voted for each class by the total number of the trees in the forest. In order to convert the likelihood maps to the in-region cost functions, they are inverted (1−probability map) such that a higher probability value in the likelihood map corresponds to a lower cost in the in-region cost function.

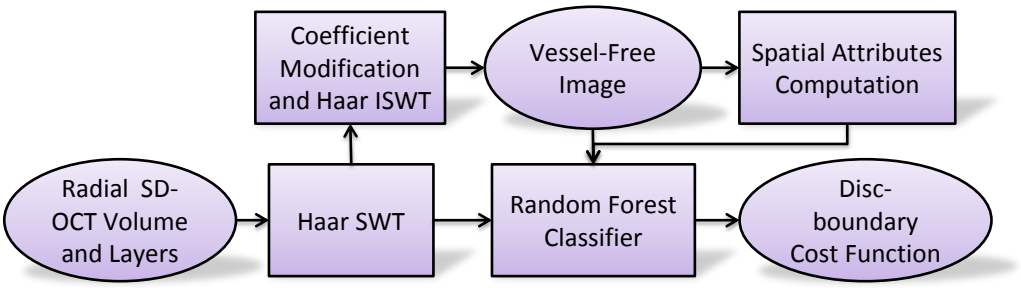

Figure 4.9: Disc-boundary cost function design flowchart.

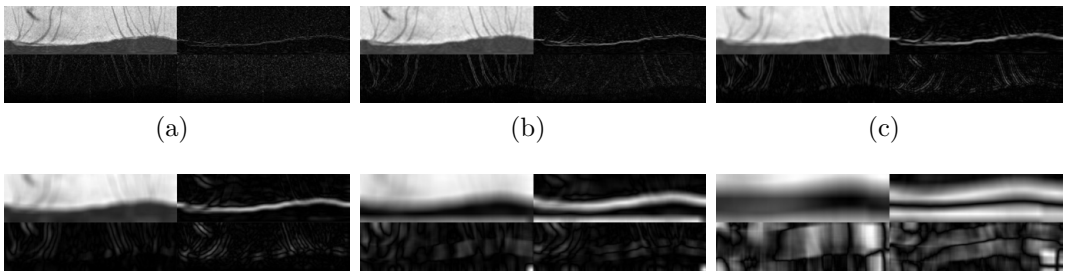

Figure 4.10: SWT decomposition. (a)-(d) SWT 6-level decomposition. In each image, upper left is the approximation, upper right is the horizontal, lower left is the vertical, and lower right is the diagonal SWT coefficient.

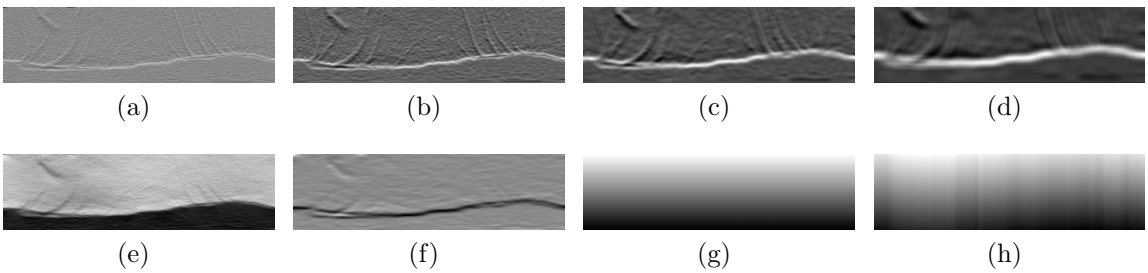

Figure 4.11: On-boundary cost function feature set. (a)-(d) Horizontal coefficients of level 1, 2, 3 and 4. (e) Vessel-free projection image. (f) Result of averaging derivative of Gaussian in the vertical direction. (g) Spatial feature imposing the shape of the optic disc boundary. (h) Spatial feature that has the anatomic information of BMO points.

4.1.3 Disc-Boundary Cost Function Computation

The flowchart of the disc-boundary cost function design is shown in Fig. 4.9. Similar to the in-region cost function design, a machine-learning approach is used to create the disc-boundary cost function. The features come from processing the radial projection image using a stationary wavelet transform (Section 4.1.3.1) and spatial features (Section 4.1.3.2). The reference standard is the projected location of the BMO endpoints so that, after the classification step (Section 4.1.3.3), the disc-boundary cost function will have a low cost at expected boundary positions.

4.1.3.1 Stationary Wavelet Transform

The Haar stationary wavelet transform [101] is a translation-invariant type of digital wavelet transform and can be used to suppress the effects of the shadows of blood vessels that make the boundary of the BMO difficult to detect in projection images. For example, the multi-scale attribute of SWT makes it capable of capturing different sizes of blood vessels in different decomposition levels. Furthermore, since the blood vessels tend to be vertically placed in the radial SD-OCT projection image (Fig. 4.4c) the directionality of the SWT enables it to separate the optic disc boundary (appears in horizontal coefficients) from the blood vessel (appears mostly in vertical and diagonal coefficients).

An example of projection image decomposition using the Haar SWT is shown in Fig. 4.10. The vessels mostly appear in vertical coefficient images whereas the optic disc boundary is easily recognizable in the horizontal coefficient images. Therefore, the intensity of horizontal coefficients of the 1^{st}, 2^{nd}, 3^{rd} and 4^{th} decomposition levels are added to the feature set. The horizontal coefficients in level 5 and 6 are not considered because at higher decomposition levels (coarser levels), the boundary of interest becomes blurrier. Note that the output of each decomposition level in SWT has the same number of samples (coefficients) as the input which makes the SWT an inherently redundant procedure.

Furthermore, a vessel-free projection image is created from the wavelet coefficients by suppressing all the vertical and diagonal coefficients (setting them to zero) at all levels and keeping the approximation and horizontal components at each level. Applying the Inverse SWT (ISWT) to the modified wavelet coefficients creates a vessel-free projection image (Fig. 4.11e). The intensity of the vessel-free projection image along with its derivative (Fig. 4.11f), computed using an averaging derivative of Gaussian filter, are added to the feature set as well.

4.1.3.2 Spatial Features

In addition to the above SWT-based features, there are two spatial features created to learn the position of the optic disc boundary in the radial projection images. The first spatial feature intuitively reflects the radial distance from a rough circular approximation of the optic disc boundary. More specifically, as any circle centered at the optic disc center appears as a horizontal line in the radial vessel-free projection image, P_{radial}, we first locate the first "dark" horizontal line (from the top) $r = r_{\text{dark}}$ in the projection image as follows:

$$r_{\text{dark}} = \min \left\{ r | I_{\text{row}}(r) \leq \mu_{I_{\text{row}}} - \sigma_{I_{\text{row}}} \right\} \ , \tag{4.5}$$

where

$$I_{\text{row}}(r) = \frac{1}{360} \sum_{\theta=0}^{359} P_{\text{radial}}(r, \theta) \ , \tag{4.6}$$

$$\mu_{I_{\text{row}}} = \frac{1}{R} \sum_{r=1}^{R} I_{\text{row}}(r) \ , \text{ and} \tag{4.7}$$

$$\sigma_{I_{\text{row}}} = \sqrt{\frac{1}{R-1} \sum_{r=1}^{R} (I_{\text{row}} - \mu_{I_{\text{row}}})^2} \ . \tag{4.8}$$

Once the first dark row is detected using (4.5), the signed radial distance from this row is considered as the spatial feature. This information helps classifier to narrow

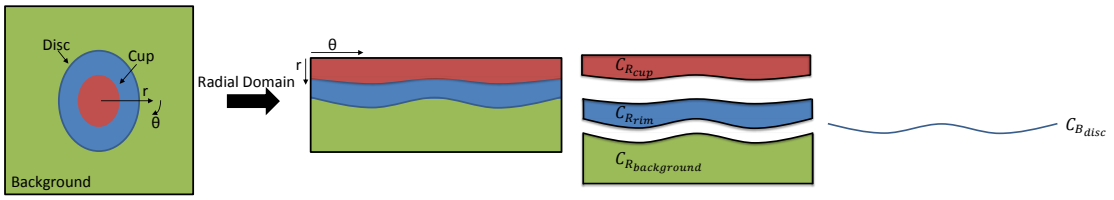

(a) (b)

Figure 4.12: A schematic representation of segmenting the optic disc and cup boundaries using a theoretical graph based approach. (a) Left is the original image and right is the resampled image in radial domain. (b) Example cost of two boundaries for the multiple boundary segmentation problem. The two boundaries divide the images into three regions.

the spatial search region for detecting the optic disc boundary (Fig. 4.11g).

The second spatial feature contains information regarding the *a priori* knowledge of the BM-ILM anatomical relationship that dictates that Bruch's membrane (and correspondingly the BMO), even in the severe cases of glaucoma where there is no rim tissue left, may touch the ILM surface, but not cross with it. In order to include that information in the feature set, the radial distance to the crossing location of ILM at the level of the interpolated surface three is also considered as a spatial feature (Fig. 4.11h).

4.1.3.3 Classification

The summary of the features used for disc-boundary classification is as follows:

1. Features 1-4: The intensity of SWT horizontal coefficients of the 1st, 2nd, 3rd and 4th decomposition levels.
2. Features 5: The intensity of the vessel-free projection image.
3. Feature 6: The intensity of the derivative of the vessel-free projection image.
4. Feature 7-8: The spatial features carrying the information regarding the anatomy and shape of the optic disc boundary.

Once the feature set is completed, a random forest classifier (with $N = 500$ trees and $m = 3$ randomly selected features at each decision split) is trained to learn the position of BMO end points using the extracted features to classify the pixels into two classes of boundary and non-boundary (background). The classes are highly imbalanced as for each radial image (100×360), the size of the background class (99×360) is much larger than the size of the boundary class (360). Therefore, the class priors are presented to the random forest classifier as well.

A probability map with low values at the expected boundary locations needs to be used as the disc-boundary cost function for the graph-theoretic step. Hence, similar to in-region cost function computation, the probability map of optic disc boundary is inverted (1− probability map).

4.1.4 Theoretical Graph Based Boundary Detection

The underlying graph-based method that is used for simultaneously segmenting the optic disc and cup boundaries is similar to what is described in [44]. The problem of multiple boundary segmentation can be considered an optimization problem with the goal of finding the feasible optic disc and cup boundaries with the minimum cost. The feasibility constraints include a *boundary smoothness* constraint to ensure that each individual boundary is smooth and a *boundary interaction* constraint to specify the minimum and maximum allowed distances between the boundaries. A schematic representation of the problem of segmenting optic disc and cup boundaries is shown in Fig. 4.12. The following equations are written in the radial domain. Consider a 2D image in the radial domain $I(r, \theta)$ of size $R \times \Theta$ and assume that the cup and disc boundaries can be defined as $f_{cup}(\theta)$ and $f_{disc}(\theta)$ functions (mapping θ values to r values), respectively. Also, assume the functions use a two-neighbor relationship so that for each column, each boundary intersects with each column (each θ) once (at r). The cup boundary smoothness constraint for neighboring columns $\{\theta_1, \theta_2\}$ in the

θ-direction is defined as below

$$-\Delta_\theta \leq f_{cup}(\theta_1) - f_{cup}(\theta_2) \leq \Delta_\theta \ . \tag{4.9}$$

The smoothness constraint of the optic disc boundary is similar to that of the cup boundary. For the boundary interaction constraints, the minimum allowed distance between the cup boundary and the disc boundary is defined as $\delta^l_{\text{cup}-\text{disc}}$ and similarly the maximum allowed distance is defined as $\delta^u_{\text{cup}-\text{disc}}$.

There are three regions: the optic cup region, the rim region (the region between optic disc and optic cup), and the background. The in-region cost functions associated with the three regions are $C_{\text{cup}-\text{reg}}(r,\theta)$, $C_{\text{rim}-\text{reg}}(r,\theta)$, and $C_{\text{background}-\text{reg}}(r,\theta)$, respectively. $C_{\text{disc}-\text{bound}}(r,\theta)$ is the disc-boundary cost function. The total cost of a set of boundaries, $C_{\{f_{\text{disc}}(\theta),f_{\text{cup}}(\theta)\}}$, can be written as the weighted sum of in-region costs and the disc-boundary cost as given below:

$$\begin{aligned} &C_{\{f_{\text{disc}}(\theta),f_{\text{cup}}(\theta)\}} = \\ &\alpha\, C_{B_{\text{disc}}} + (1-\alpha)\left[C_{R_{\text{cup}}} + C_{R_{\text{rim}}} + C_{R_{\text{background}}}\right] \ , \end{aligned} \tag{4.10}$$

where

$$C_{B_{\text{disc}}} = \sum_{\{(r,\theta)|r=f_{\text{disc}}(\theta)\}} C_{\text{disc}-\text{bound}}(r,\theta) \tag{4.11}$$

and

$$
\begin{aligned}
C_{R_{\text{cup}}} &= \sum_{(r,\theta)\in R_{\text{cup}}} C_{\text{cup}-\text{reg}}(r,\theta) \\
C_{R_{\text{rim}}} &= \sum_{(r,\theta)\in R_{\text{rim}}} C_{\text{rim}-\text{reg}}(r,\theta) \\
C_{R_{\text{background}}} &= \sum_{(r,\theta)\in R_{\text{background}}} C_{\text{background}-\text{reg}}(r,\theta).
\end{aligned}
\tag{4.12}
$$

Note that $C_{B_{\text{disc}}}$ represents the total cost corresponding to pixels on the disc boundary and $C_{R_{\text{cup}}}$ $C_{R_{\text{rim}}}$, and $C_{R_{\text{background}}}$ represents the cost related to pixels belonging to cup, rim, background regions, respectively. In (4.10) $\alpha = 1$ implies using boundary information only and $\alpha = 0$ implies using region information only.

The in-region cost functions and disc-boundary cost function are computed using a machine-learning approach as described in Sections 4.1.2.4 and 4.1.3.3 and transferred to the radial domain (Fig. 4.13). The two globally optimal feasible boundaries are obtained by finding a minimum closure on the vertex-weighted graph. In order to do that, the constructed graph is transferred to a closely related edge-weighted graph and finding a minimum $s-t$ cut gives us the optimal solution [44]. The α value in (4.10) changes over the range of 0 to 1 in increments of 0.1 and the value that produces the lowest segmentation error is selected (here $\alpha = 0.9$). The process is similar to what is outlined in [44]. Moreover, the continuity condition of the boundaries is imposed in constructing the graph by enforcing the constraint that the first and last columns of the image are neighbors.

Once the optimal boundaries are segmented, a postprocessing step is applied to remove any possible remaining errors at the blood vessel locations by fitting a smoothing spline to the optic disc and cup boundaries. The last step is to transfer the segmentation results back to Cartesian coordinates.

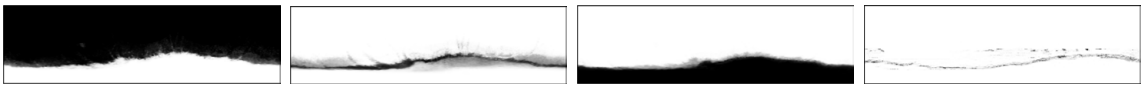

(a) (b) (c) (d)

Figure 4.13: An example of cost functions. (a) The in-region cost function for the background. (b) The in-region cost function for the rim. (c) The in-region cost function for the optic cup. (d) The optic-disc-boundary cost function. Note that there is no cup-boundary cost function.

4.2 Experimental Methods

4.2.1 Data

The dataset for this chapter includes 25 SD-OCT scans of glaucoma patients centered at optic nerve head that were acquired using a Cirrus HD-OCT device (Carl Zeiss Meditec, Inc., Dublin, CA) at the University of Iowa. The size of each scan was 200×200×1024 voxels (in the x-y-z direction, respectively) which corresponds to a voxel size of 30×30×2 μm, and the voxel depth was 8 bits in grayscale. The stereo color photograph pairs of the optic disc corresponding to each SD-OCT scan were taken from each patient the same day using a stereo-base Nidek 3-Dx stereo retinal camera (Nidek, Newark, NJ). The size of the stereo color photographs was 768×1019 pixels, and the pixel depth was 3 8-bit red, green and blue channels.

4.2.2 Reference Standard

The reference standard for the optic cup came from the stereo color photographs. Computer-aided planimetry was performed by three fellowship-trained glaucoma experts on stereo color photographs of the optic disc [7] and the reference standard was obtained based on consensus, meaning that the pixel that has the majority of votes (two of three) for cup region was assigned the optic cup label. The boundary of the region labeled as cup was used as the reference standard of the cup boundary in the evaluation.

To obtain the disc-boundary reference standard, one expert first traced the BMO endpoints on the 3D SD-OCT volume with two additional experts providing corrections resulting in final tracing that was the result of the consensus of three experts through a discussion. The 2D projection of the BMO endpoints produced the optic disc boundary reference standard.

4.2.3 Experiments

Three methods were compared based on the optic disc and cup segmentation performance: 1) optic disc and cup segmentation using region information only for which the in-region cost functions were produced by a classifier trained using a unimodal feature set (SD-OCT features as in [16]); 2) optic disc and cup segmentation using region information only for which the in-region cost functions were produced by a classifier trained using a multimodal feature set (fundus and SD-OCT features); and 3) optic disc and cup segmentation using region and disc-boundary information for which the in-region cost functions were produced by a classifier trained using a multimodal feature set. Note that all three approaches combine use of a machine-learning approach for designing the cost functions for use in a final graph-based step to obtain the final disc/cup boundaries simultaneously. The first two approaches only involve in-region cost function terms (with the first approach using only the SD-OCT features proposed in this work and the second approach using the region-based fundus features in addition to the SD-OCT features), whereas the last approach builds upon the second approach by also incorporating a machine-learned disc-boundary cost function term.

To evaluate the three methods for optic disc and cup segmentation, a leave-one-subject-out experiment (including the training of the classifiers) was carried out on the 25 subjects and the results were compared with the reference standard. Dice similarity coefficient (DSC), as well as unsigned and signed border positioning errors, were used to assess the accuracy of optic disc and cup segmentation. More specifically,

for two regions, A and B, the DSC was given by:

$$DSC(A, B) = \frac{2(A \cap B)}{(A + B)} \, . \tag{4.13}$$

The signed and unsigned border positioning errors of the optic disc and cup were calculated in the radial domain. The unsigned border positioning error was calculated by averaging the distances between all boundary points from the segmentation result and the ones from the reference standard. The signed border positioning error was calculated similarly to the unsigned border positioning error, but the signs of the distances were retained. The sign was considered positive if the algorithm's boundary point was farther away from the optic disc center than the boundary point of the reference standard. Paired t-tests were performed to compare the segmentation results (p-values < 0.05 were considered significant).

The proposed methods were also evaluated based on the CDR values. The mean and standard deviation of absolute difference with the reference standard as well as the Pearson correlation with the reference standard were computed.

4.3 Results

Example segmentation results for patients with different CDRs are shown in Fig. 4.14, Fig.4.15, and Fig.4.16. The DSC values are shown in Table 4.2. Based on DSC values for the optic disc segmentation, the multimodal approaches outperformed the unimodal approach ($p < 0.05$). Also, the multimodal approach with inclusion of the disc-boundary information outperformed the region-only multimodal approach for the optic disc segmentation ($p < 0.05$). For the optic cup boundary, the multimodal approach outperformed the unimodal approach ($p < 0.05$). As expected, since no cup-boundary cost function was used, both multimodal approaches resulted in the same DSC values for the cup.

The unsigned border positioning errors are reported in Table 4.3. The unsigned

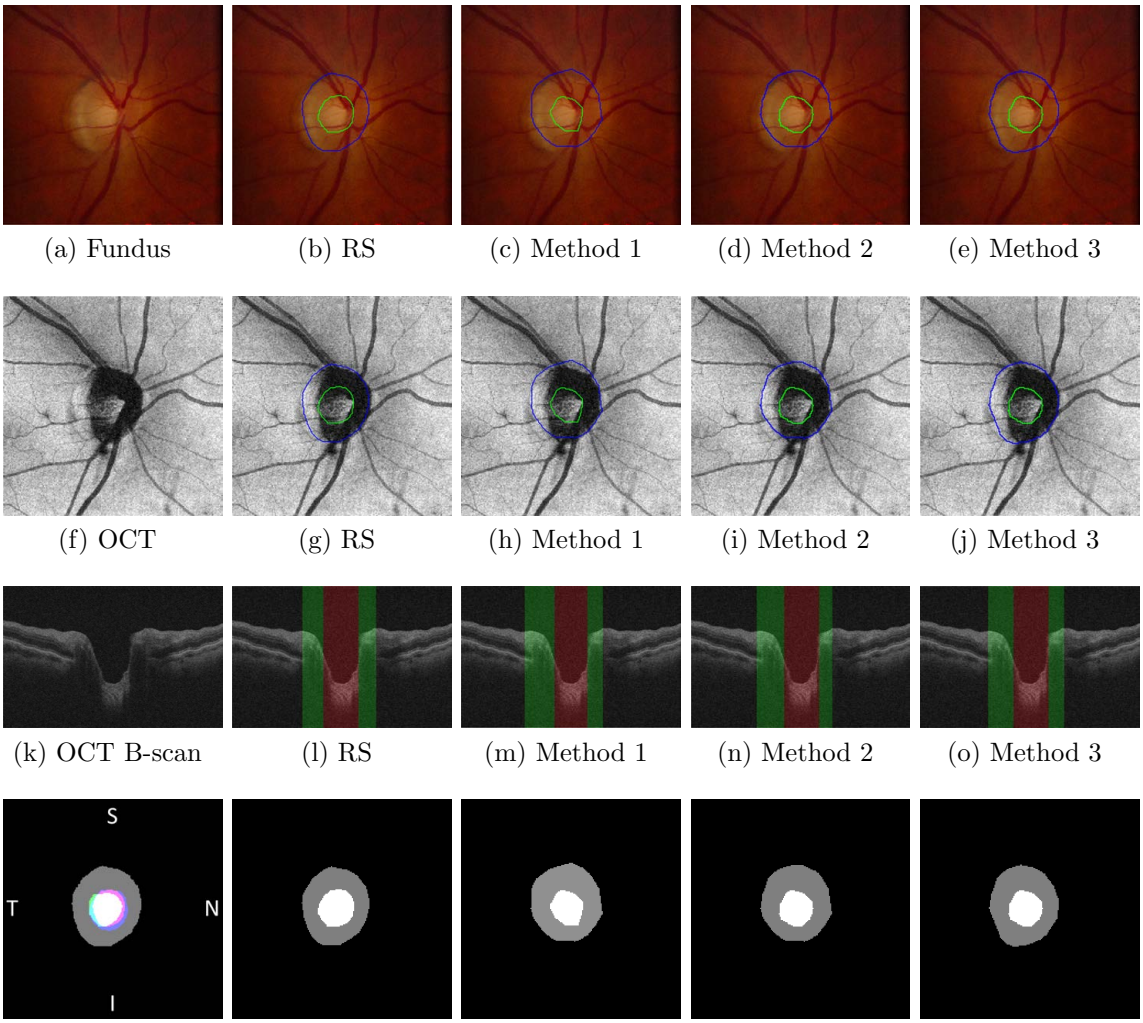

(a) Fundus (b) RS (c) Method 1 (d) Method 2 (e) Method 3

(f) OCT (g) RS (h) Method 1 (i) Method 2 (j) Method 3

(k) OCT B-scan (l) RS (m) Method 1 (n) Method 2 (o) Method 3

(p) Manuals (q) RS (r) Method 1 (s) Method 2 (t) Method 3

Figure 4.14: An example segmentation result with CDR = 0.25. The first row contains the (a) registered fundus photograph with (b) the reference standard boundaries, (c) the boundaries of the first method (using unimodal region costs), (c) the boundaries of the second method (using multimodal region costs), and (d) the boundaries of the third method (using multimodal region plus disc-boundary costs). The blue boundary corresponds to the optic disc boundary and the green boundary corresponds to the cup boundary. The second row contains the boundaries of the methods shown on the SD-OCT projection image. The third row contains a central B-scan of the SD-OCT with green indicating the rim region and red indicating the cup region from the different methods. The last row contains the region-based segmentation results (black = background; gray = rim; white = cup). It is especially noticeable on the inferior (I) and temporal (T) sides of optic disc boundary that the third method has the closest boundary to the reference standard. In addition, the unimodal approach has a relatively smaller optic cup than the multimodal approach in comparison with the reference standard.

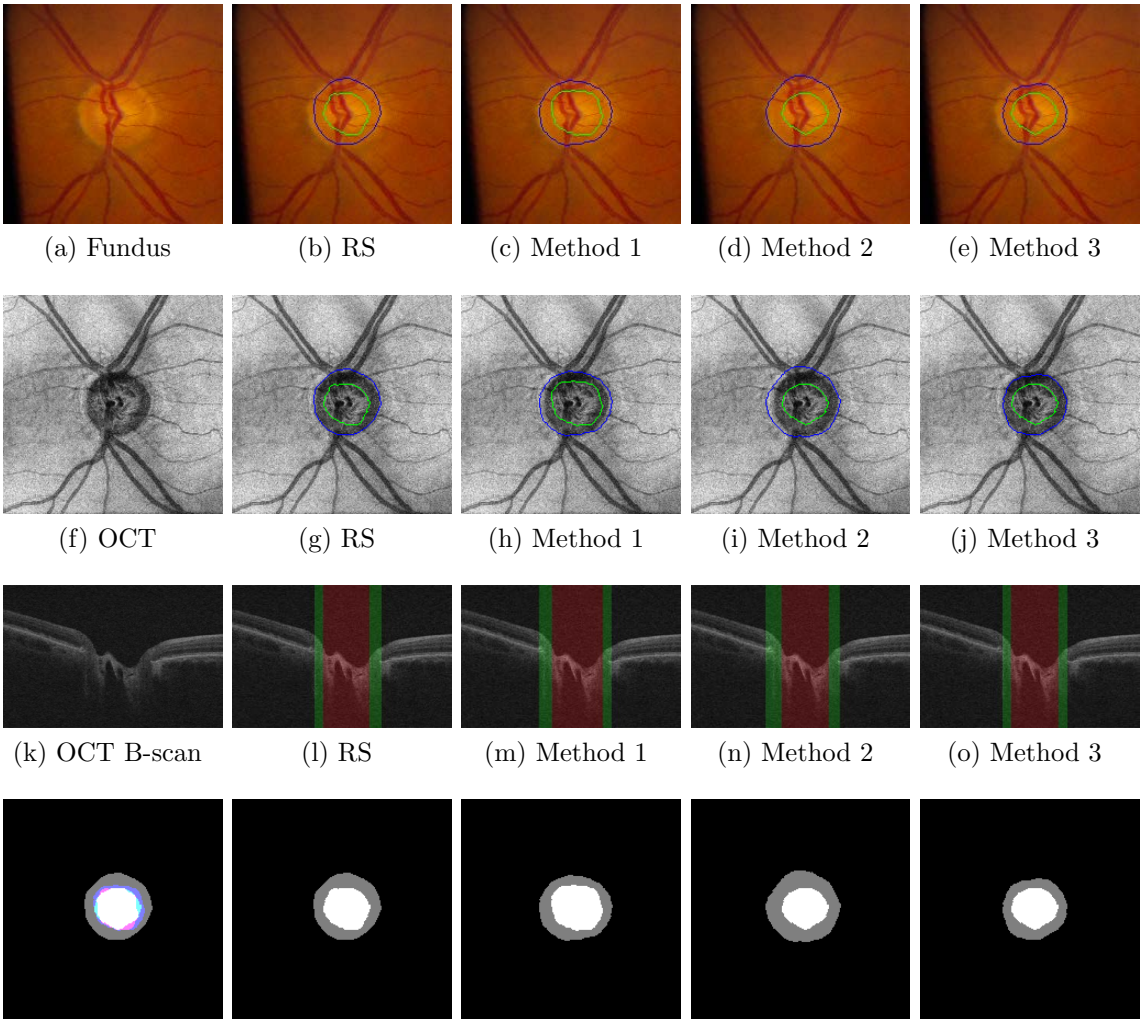

(a) Fundus (b) RS (c) Method 1 (d) Method 2 (e) Method 3

(f) OCT (g) RS (h) Method 1 (i) Method 2 (j) Method 3

(k) OCT B-scan (l) RS (m) Method 1 (n) Method 2 (o) Method 3

(p) Manuals (q) RS (r) Method 1 (s) Method 2 (t) Method 3

Figure 4.15: An example segmentation result with CDR = 0.44.

Table 4.2: Dice Similarity Coefficients (Mean± SD)

Methods	Cup	Disc
in-region (OCT)	0.851±0.031	0.735±0.102
in-region (OCT+Fundus)	0.855±0.009	0.781±0.095
in-region + disc-boundary	0.855±0.009	0.824±0.086

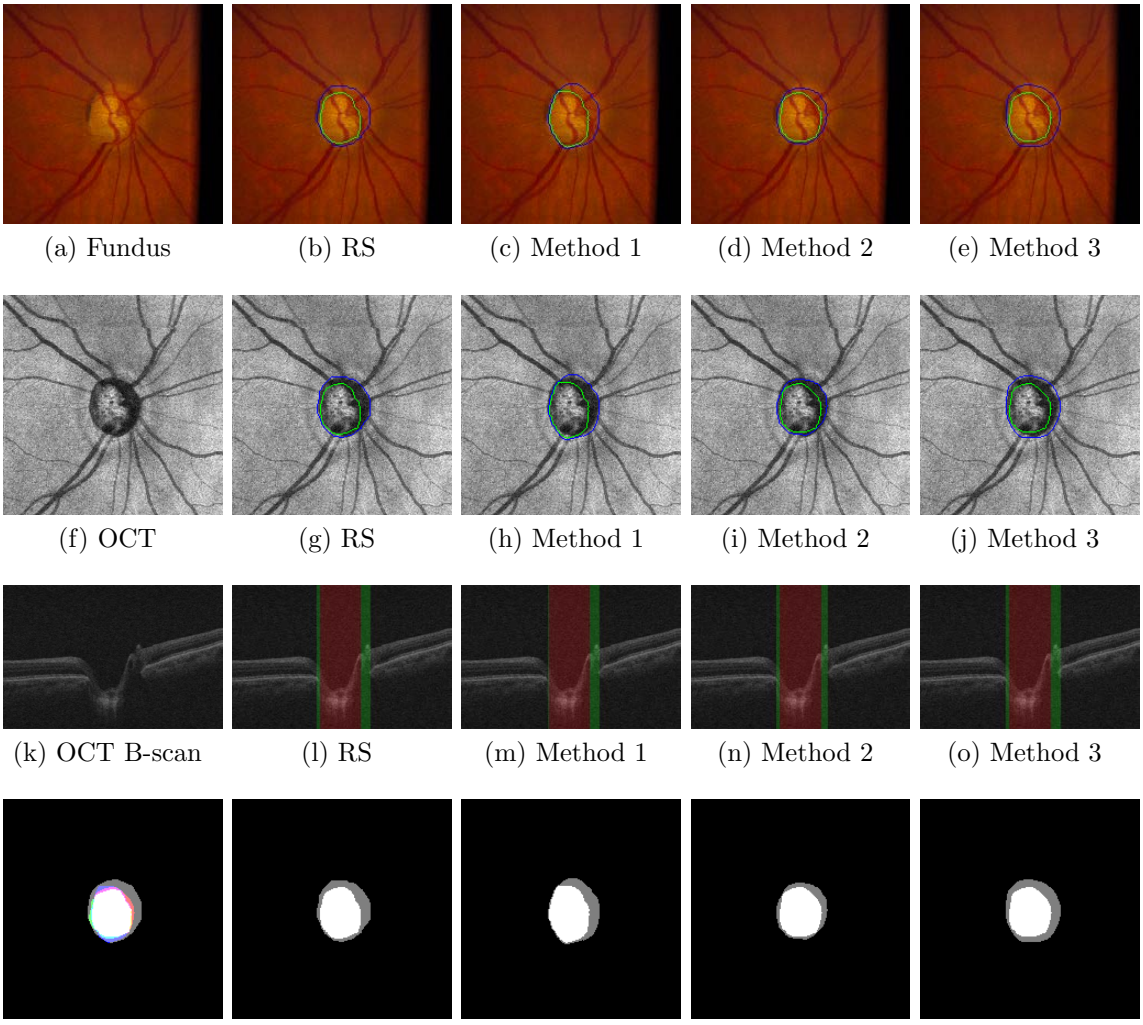

(a) Fundus (b) RS (c) Method 1 (d) Method 2 (e) Method 3

(f) OCT (g) RS (h) Method 1 (i) Method 2 (j) Method 3

(k) OCT B-scan (l) RS (m) Method 1 (n) Method 2 (o) Method 3

(p) Manuals (q) RS (r) Method 1 (s) Method 2 (t) Method 3

Figure 4.16: An example segmentation result with CDR = 0.44.

Table 4.3: Unsigned Border Positioning Error (Mean± SD)

Methods	Cup (pixel)	Cup (mm)	Disc (pixel)	Disc (mm)
in-region (OCT)	2.520±0.723	0.075±0.021	2.053±0.731	0.061±0.021
in-region (OCT+Fundus)	2.262±0.621	0.067±0.018	1.971±0.694	0.059±0.020
in-region + disc-boundary	2.262±0.621	0.067±0.018	1.602±0.587	0.048±0.017

Table 4.4: Signed Border Positioning Error (Mean± SD)

Methods	Cup (pixel)	Cup (mm)	Disc (pixel)	Disc (mm)
in-region (OCT)	0.015±1.08	0.000±0.032	0.351±1.03	0.010±0.030
in-region (OCT+Fundus)	0.017±1.01	0.000±0.029	0.171±0.87	0.005±0.025
in-region + disc-boundary	0.017±1.01	0.000±0.029	0.019±0.61	0.001±0.017

border positioning error of the optic cup segmentation of the multimodal methods was significantly lower than the unsigned border positioning error of the optic cup segmentation of the unimodal method ($p < 0.05$). As with the DSC values, the unsigned border positioning errors for the cup were the same for both multimodal approaches. In addition, the unsigned border positioning error of the optic disc segmentation of the multimodal methods were significantly lower than the unsigned border positioning error of the optic disc segmentation of the unimodal method ($p < 0.05$). Moreover, the multimodal method that used the disc-boundary information outperformed the region-only multimodal method as it had a significantly lower unsigned border positioning error of the optic disc segmentation ($p < 0.05$).

The signed border positioning errors are reported in Table 4.4. The multimodal approaches had a significantly smaller positive bias for the optic disc segmentation than the unimodal approach ($p < 0.05$). Also, the positive bias of optic disc segmentation for the multimodal approach that used the disc-boundary information was significantly less than the region-only multimodal method ($p < 0.05$). However, the positive bias of the optic cup segmentation for the multimodal method and the uni-

Table 4.5: CDR analysis. Pearson correlation (r) with reference standard and the absolute difference from the reference standard (Mean± SD)

Methods	Correlation	Difference
in-region (OCT)	0.890	0.101±0.082
in-region (OCT+Fundus)	0.899	0.097±0.076
in-region + disc-boundary	0.928	0.082±0.048

modal method weren't significantly different ($p > 0.1$).

The CDR correlations (Table 4.5) of the first and second methods with the reference standard were not significantly different ($p = 0.27$). However, the correlation of the third method with the reference standard was significantly better than the correlations of the other two approaches with the reference standard ($p < 0.05$). Similarly, the absolute CDR differences (with the reference standard) of the first and second methods were not significantly different ($p = 0.15$), whereas, the third method had significantly smaller absolute CDR differences with the reference standard than that of the first and second methods.

4.4 Discussion and Conclusion

In this chapter, we presented a unimodal (from SD-OCT volumes only) and two multimodal (from SD-OCT volumes and color fundus photographs) machine-learning graph-based approaches for automated segmentation of the optic disc and cup. Our results showed that both multimodal approaches outperformed the unimodal approach and that the multimodal approach that incorporated an additional disc-boundary cost term outperformed the multimodal approach that only incorporated region-based terms. Our multimodal approaches differ from prior work that has focused on segmenting the optic disc/cup in color fundus images alone [7–15] or SD-OCT images alone [16–18]. Another difference from prior work is our combined use of a machine-learning approach with a graph-theoretic approach to simultane-

ously find the globally optimal disc- and cup-boundary pair (with respect to the cost function). Thus, in addition to the novelty of the two multimodal approaches for optic disc/cup segmentation, the unimodal (SD-OCT only) approach was novel as well as prior SD-OCT-only approaches were either classification-based without a graph-based step [16,17] or focused on only finding the projected BMO using a graph-based approach without any incorporation of machine-learned costs [18]. An additional, more subtle, difference from prior work is that our reference standard for the disc boundary was defined based on the projective location of the BMO from SD-OCT volumes rather than the fundus-based disc boundary to reflect the current understanding of the most appropriate boundary to use for SD-OCT-based definitions of optic-nerve-head structures.

While our results demonstrated the improved performance using a combined machine-learning and graph-based multimodal approach over that using a combined machine-learning and graph-based SD-OCT-only approach, our results did not explicitly demonstrate the extent the multimodal approach would provide an improvement over a fundus-only approach. However, this comparison is perhaps somewhat less interesting given our prior experience in the improved segmentation results one can obtain using SD-OCT-only information from that of fundus-only information [7,88]. For example, in the dataset used in this work, at the intermediate classification stage (i.e., before use of the graph-based step), using the fundus-only and SD-OCT-only defined features in this work, the fundus-only approach has a significantly smaller ($p < 0.05$) pixel-based classification accuracy (overall: 86%; cup: 78%; rim: 72%; background: 89%) compared to the SD-OCT-only approach (overall: 95%; cup: 85%; rim: 83%; background: 96%). While it is possible that use of a different approach or a different set of fundus-based features could result in higher fundus-only accuracies than those resulting from the fundus-only features used in this work, the fact that the additional inclusion of the fundus features provides an improvement over the

SD-OCT-only approach is important.

Hu *et al.* previously described a multimodal approach for the segmentation of retinal vessels in color-fundus photographs and SD-OCT volumes and also demonstrated that multimodal approaches outperform SD-OCT-only approaches [93]. In that work, multimodal information was most beneficial for the segmentation of the vessels in the optic-nerve-head region. This is not surprising as the visibility of retinal vessels in SD-OCT projection images is often drastically reduced inside the disc region because of the lack of RPE tissue to offer contrast with the vessel shadows. Correspondingly, the addition of complementary color fundus information to the SD-OCT information was particularly beneficial in the disc region. Our present work is consistent with this prior work as we again find that the complementary color information from fundus photographs to be particularly helpful in the segmentation of structures (rim/cup in this case) in the disc region.

As in the multimodal work of Hu *et al.* for vessel segmentation [93], this work includes a registration step to register the fundus photograph to the SD-OCT projection image so that multimodal features can be computed at each projected location. While a modified ICP algorithm was used for registration in this work, it can be expected that other successful fundus-OCT registration approaches could be used as well. However, one potential limitation of the registration step is that any registration errors (e.g., due to motion artifacts) may limit the local accuracy of the multimodal features. While registration errors were not a problem in our dataset, it may be useful in future work to consider developing an approach to automatically assess the quality of the registration to help provide an estimate of the reliability of the multimodal features. In cases where the image registration is deemed unreliable, the approach could depend more on SD-OCT-only features.

The presence of blood vessels near the optic nerve head traditionally presents a challenge for disc/cup segmentation approaches [18, 93, 102]. The vessels in this area

are wider, and their location near the optic disc/cup boundaries could potentially cause a disturbance of the local geometry and depth measurements (causing misclassification of the A-scans on the vessels used in the cost-function terms or affecting the layer segmentation locally). In this work, the use of smoothed fundus photographs in which the blood vessels are less pronounced in addition to our use of a vessel-free radial projection as a feature for computing the disc-boundary cost function, helped to minimize the impact of the blood vessels. However, development of alternative strategies for dealing with blood vessels may prove beneficial in future work.

Because of the ability of random forests to more naturally deal with low-quality or redundant features during training (compared to other candidate approaches, such as k-nearest-neighbor approaches), a feature selection stage was not incorporated for the design of the in-region and disc-boundary cost terms in this work. However, there of course is still potential value in using a smaller subset of features (e.g., a lower computation time). Thus, it may useful in future work to evaluate the accuracy with smaller subsets of features. As a start in this direction, the seven most discriminative features for the classifier used for generating the multimodal in-region costs included the optic disc depth information, the outputs of the Gaussian filter ($\sigma = 6$) on dark-bright and ($\sigma = 8$) on red-green channels, the *a priori* probability of pixel being cup and disc, the OCT projection image, and the average of the intensities of the first SD-OCT sub-volume above the fitted BM spline surface. The three least discriminative features included the average of the intensities of the second SD-OCT sub-volume below the fitted BM spline surface and the outputs of the Gaussian filter ($\sigma = 4$) on the red and blue channels.

While we have only applied our approach to the SD-OCT volumes from a single manufacturer, it is expected that the general scheme of the proposed method (i.e., use of multimodal information and combining a machine-learning with a graph-theoretic approach) would be applicable to other SD-OCT machines as long as the B-scans in

the y-direction are dense enough to allow the registration of the fundus photograph to the SD-OCT projection image. Moreover, if the B-scans are too sparse, the SD-OCT features proposed in this work may not be meaningful or be possible to extract.

In summary, we showed that we can benefit from use of complementary information from both modalities instead of unimodal information for segmenting the optic disc and cup boundaries. Different features were extracted from registered fundus photographs and SD-OCT volumes to create a multimodal feature set. A random forest classifier was trained using the multimodal feature set to produce three in-region cost functions associated with cup, rim, and background regions. A set of SWT-based features were extracted from SD-OCT volumes to be utilized in training a random forest classifier for producing the disc-boundary cost function. The graph-theoretic approach was able to well-define the boundaries of interest using the cost functions and enabled us to impose the desired constraints to the boundaries. Use of a similar multimodal graph-based strategy is expected to be beneficial in other application areas as well.

CHAPTER 5
COMPUTING RIM-WIDTH-BASED PARAMETERS IN THE PRESENCE OF EXTERNALLY OBLIQUE BORDER TISSUE (EOBT)

The content of this chapter is presented in [103,104]. Traditionally, the characteristic structural changes occurring at the optic nerve head in glaucoma have primarily been assessed through direct funduscopic observation or examination of digital color (stereo) fundus photographs, and more recently, optical coherence tomography. However, standard fundus-photograph disc-based measurements, such as the cup-to-disc ratio, are limited by the ability to reliably delineate clinically meaningful disc and cup margins [2,5,19,105–107]. Recent work in co-localizing fundus-photograph-based clinical disc margins with underlying structures in optical coherence tomography volumes has demonstrated that the disc margin as visualized on indirect ophthalmoscopy and biomicroscopy does not co-localize with a consistent anatomic structure, due, in part, to variability in presence of externally oblique border tissue (EOBT) and invisibility of Bruch's membrane extensions [2–4, 6, 19].

In spectral domain-optical coherence tomography (SD-OCT), the three-dimensional nature allows for the computation of alternative structural parameters such the Bruch's membrane opening-minimum rim width (BMO-MRW) [2, 3, 108]. BMO-MRW accounts for different trajectories of the rim tissue [108] and also correlates with retinal nerve fiber layer thickness (RNFLT) and visual field mean deviation significantly better than the traditional clinical disc margin [109]. Furthermore, BMO-MRW is superior to other structural parameters such as BMO-horizontal rim width (BMO-HRW), defined as the horizontal distance of the BMO to the ILM surface computed in the reference plane of the BMO (Fig. 5.1), for diagnosing open-angle glaucoma [3]. Since BMO-HRW is not always the shortest distance from BMO to the ILM surface (Fig. 5.1b), it is possible that BMO-HRW overestimates the remaining neuroretinal rim.

However, the development of automated algorithms for determining BMO-MRW

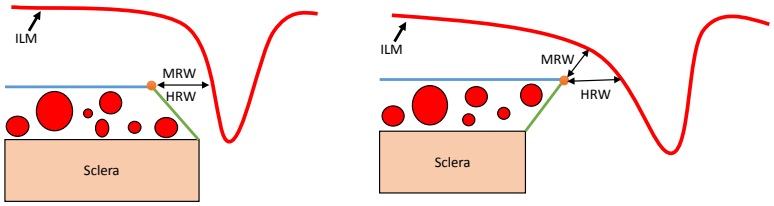

(a) (b)

Figure 5.1: Comparing BMO-HRW and BMO-MRW measurements. (a) Example where BMO-HRW reflects the same distance as BMO-MRW and (b) example where BMO-HRW does not reflect the shortest distance to the ILM surface (BMO-MRW).

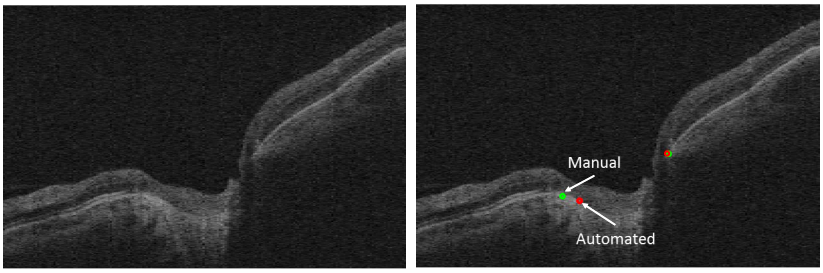

(a) (b)

Figure 5.2: EOBT B-scans where the automated approach [24] is confused between the BMO and the extension of border tissue (right side); the manual tracing, however, marks the BMO point.

presents challenges. For example, the anatomy of the border tissue with respect to the anterior edge of the sclera (e.g. in presence of EOBT [19]) not only could cause disparity between the traditional clinical disc margin and the BMO-MRW [2] but also could cause difficulty in detecting the BMO points [24]. As EOBT attaches to the end of BM surface and merges with BMO, automated approaches [24], and even humans, may be confused between BMO and the extension of border tissue (Fig. 5.2).

In cases of EOBT, rather than using a point-to-surface shortest distance (BMO-MRW) that may be subject to difficulties in precisely defining the BMO, in this work,

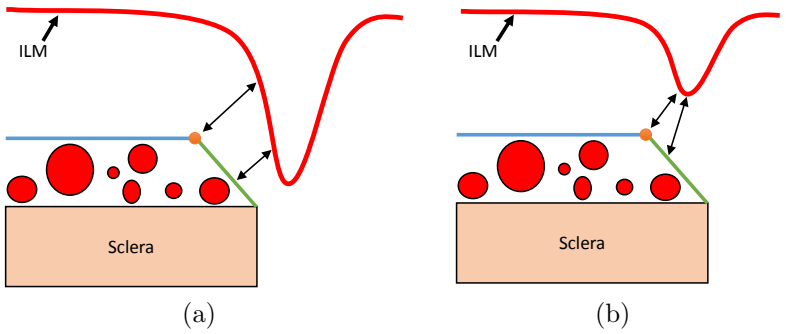

Figure 5.3: (a) EOBT case where the closest point to the ILM surface falls on the anterior surface of border tissue. (b) EOBT case where the closest point to the ILM surface is BMO (the orange dot).

we propose to instead use the surface-to-surface shortest distance (EOBT-MRW, defined as the distance between the closest point along the extension of the border tissue to the ILM). In addition to being an easier measure to define (especially for automated algorithms) in cases of ambiguity between the BMO and EOBT, there are also situations where the closest point to the ILM surface does not fall on BMO; rather it falls on the anterior surface of the border tissue (Fig. 5.3). We demonstrate that relaxing the definition of the BMO-MRW to allow for a surface-to-surface shortest distance (EOBT-MRW) in cases of EOBT will still allow for similar structure-structure correlations. Furthermore, we demonstrate that RNFLT correlations with the *surface*-to-surface shortest distance (EOBT-MRW) are significantly higher than correlations with a point-to-surface distance measure from an arbitrary point (e.g. the ending point of the border tissue) on the EOBT to the ILM (EOBT_{E}-MRW), further demonstrating the importance of the proposed *surface*-to-surface measure rather than a *point*-to-surface measure.

In particular, the purpose of this chapter is to compare two structural parameters (BMO-MRW and the new surface-to-surface measure, EOBT-MRW) in presence of EOBT through structure-structure correlations of these measurements with RNFLT.

Additionally, in order to examine which measurement better reflects the remaining neuroretinal rim, the correlation of RNFLT with BMO-MRW and BMO-HRW are compared.

5.1 Methods

5.1.1 Data

The dataset includes SD-OCT scans of 44 glaucoma patients in different stages of glaucoma. The 44 subjects were selected so that the distribution of visual field severities matched that in the complete dataset used in [110]. Briefly, patients aged 45-80, diagnosed with glaucoma suspect or open-angle glaucoma were recruited prospectively. Patients with a history of angle closure or combined mechanism glaucoma, or any non-glaucomatous optic neuropathy, corneal or retinal diseases that could affect visual field, cataracts or any other disease with visual acuity $< 20/40$ were excluded. Based on the mean deviation (MD) of 24-2 HVF threshold testing, the patients were recruited in an age-matched fashion in one of three approximately equally sized severity groups including mild glaucoma (including glaucoma suspects) with MD < 6 dB loss (17 patients), moderate glaucoma with $6 \leq$ MD ≤ 12 dB loss (14 patients), and severe glaucoma with MD > 12 dB (13 patients). Optic nerve head (ONH)-centered SD-OCT volumes (Cirrus, Carl Zeiss Meditec, Inc.; $200\times200\times1024$ voxels corresponding to $6\times6\times2$ mm^3) were obtained in one eye of each patient. The original study was approved by the Institutional Review Board of the University of Iowa and adhered to the tenets of the Declaration of Helsinki. A written informed consent was given to all participants.

5.1.2 Rim-Width Based Measurements

The internal limiting membrane (ILM) was automatically segmented in each SD-OCT volume using a graph-theoretic approach [16, 44] and, along with the SD-OCT volume, transferred to the radial domain using bilinear interpolation (Fig. 5.4). The

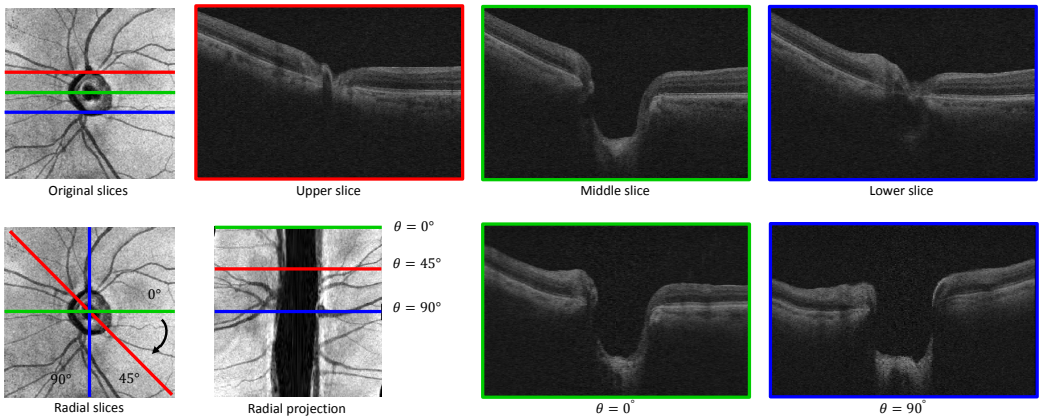

Figure 5.4: Top row shows the red, blue, and green lines on the projection image and corresponding B-scans in the original Cartesian domain. The BMO identification in the upper and lower part of the optic disc (red and blue) is difficult. The bottom row shows how the radial B-scans are acquired and the corresponding projection image in the radial domain.

radial transformation resulted in 180 radial slices (in increments of 1 degree) such that the ILM surface was defined and two BMO points were visible on each slice. The BMO points were identified on each slice using a manual (BMO_M) as well as an automated approach (BMO_A). In the manual approach, the BMO_M points on 20 evenly spaced radial slices were obtained by consensus manual delineations from three experts. The locations of BMO_M points on the remaining 160 radial B-scans were defined using piecewise cubic interpolation. For defining the automated BMO_A points, a graph-theoretic algorithm [24] was used which simultaneously segmented the BMO_A points; the surface representing the junction of the inner and outer photoreceptor segments; and Bruch's membrane surface (Fig. 5.5). BMO_M-MRW and BMO_M-HRW were computed using the manual BMO_M points and BMO_A-MRW was computed using the automated BMO_A points.

In the cases of EOBT, the extension of border tissue was segmented in order to be able to compute the EOBT-MRW. In this study, we were interested in examining

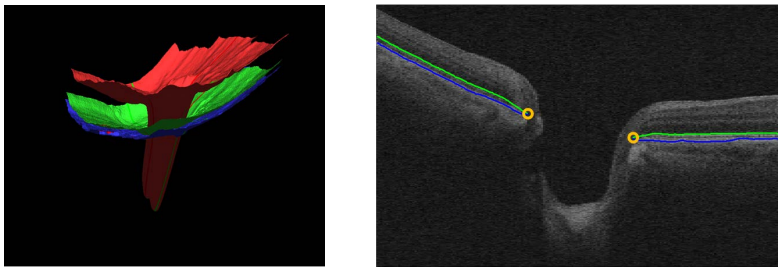

(a) (b)

Figure 5.5: The intraretinal layer segmentation. (a) The 3D layer segmentation of ILM surface (red), photoreceptors inner segments/outer segments (green) and BM surface (blue). (b) The result of surface + hole segmentation algorithm [24], considering the opening as the shared hole (yellow circles).

EOBT cases because in presence of EOBT, the closest point to the ILM may fall on the anterior surface of the border tissue rather than on the BMO (Fig. 5.3). In particular, in cases of EOBT, the ending point of the EOBT was manually marked and the anterior surface of EOBT was defined by extending the BM surface to pass through the BMO point and the EOBT end point. This was performed using a piecewise cubic interpolation. Hence, EOBT-MRW, as opposed to BMO-MRW, is a surface-to-surface measure and is computed as the shortest distance between the ILM surface and the anterior surface of border tissue. If the closest point to the ILM on EOBT was less than 30 μm away from the BMO, the point was omitted and instead the MRW was computed from the BMO_M point. In addition, EOBT_E-MRW was measured as the distance of the ending point of EOBT to the ILM surface.

To summarize, for each side of each radial scan, the following rim-width measures were computed:

- BMO_M-HRW (horizontal rim width computed based on the manual BMO_M points).
- BMO_M-MRW (minimum rim width computed based on the manual BMO_M

points).

- BMO_A-MRW (minimum rim width computed based on the automated BMO_A points).
- When EOBT was present, surface-to-surface measure, EOBT-MRW (minimum rim width computed from the anterior surface of border tissue).
- When EOBT was present, $EOBT_E$-MRW (minimum rim width computed from the ending point of the anterior surface of EOBT).

5.1.3 Structure-Structure Correlations of MRW and HRW with RNFLT

In order to evaluate the measurements, the structure-structure correlation of each measurement with RNFLT was computed. The polar plane was divided into four regions of temporal, nasal, superior, and inferior and all the measurements associated with a subject were averaged for each of the four regions. The grid was also rotated 7 degrees to take into account the angle of the line connecting the macula and the center of the optic disc [111]. In addition, all left eyes were flipped to have the same orientation as right eyes. The RNFLT was measured on a wedge-shape portion of each region. The wedge-shaped region was bounded by two radii (1.58 mm and 1.88 mm) around the standard peripapillary radius (1.73 mm) in the radial direction (Fig. 5.6). The mean value of RNFLT was computed in each wedge-shaped region and was correlated using Pearson correlation with the corresponding mean values of rim-width measurements.

5.2 Results

Out of 44 patients in the dataset, 27 patients (61%) showed EOBT in at least one radial B-scan. The distribution of B-scans having EOBT is shown in Fig. 5.7a which shows that EOBT was more common on the temporal side than on the nasal side. In 45% of the radial B-scans with EOBT, the closest point to the ILM fell on

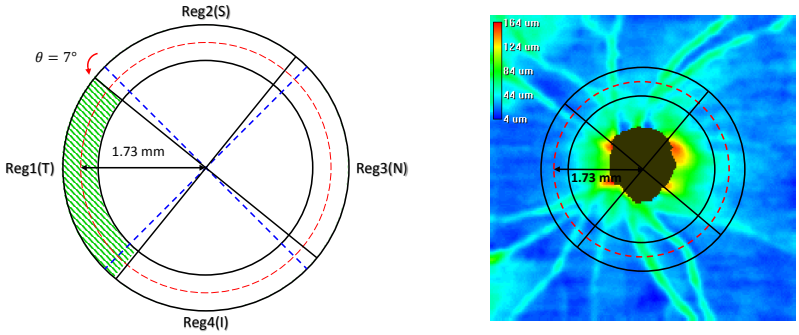

(a) (b)

Figure 5.6: The shaded region shows where the mean RNFLT is calculated for the temporal region. (b) The mask created in (a) on top of an RNFLT map.

the anterior surface of EOBT rather than on the BMO for which the distribution is illustrated in Fig. 5.7b. In EOBT cases where the closest point fell on the EOBT, the average distance of this point from the BMO was 100 ± 161 μm.

All structure-structure Pearson correlations of RNFLT with BMO_M-MRW, BMO_A-MRW, EOBT-MRW, and $EOBT_E$-MRW in the presence of EOBT are shown in Table 5.1. The method proposed by Zou *et al.* [112] for comparing two overlapping correlations based on two dependent groups was utilized to compare all Pearson correlations reported in Table 5.1. The results showed no significant difference between the Pearson correlation of BMO_M-MRW with RNFLT and that of BMO_A-MRW and EOBT-MRW ($p > 0.05$). However, the Pearson correlation of $EOBT_E$-MRW with RNFLT was significantly lower than that of BMO_M-MRW ($p < 0.05$).

The Pearson correlations of RNFLT with BMO_M-MRW, BMO_A-MRW, and BMO_M-HRW where all B-scans were included, are reported in Table 5.2. No significant difference was found [112] between structure-structure correlations of BMO_M-MRW and BMO_A-MRW with RNFLT ($p > 0.05$). However, the Pearson correlation of RNFLT with BMO_M-MRW was significantly higher than that of BMO_M-HRW with

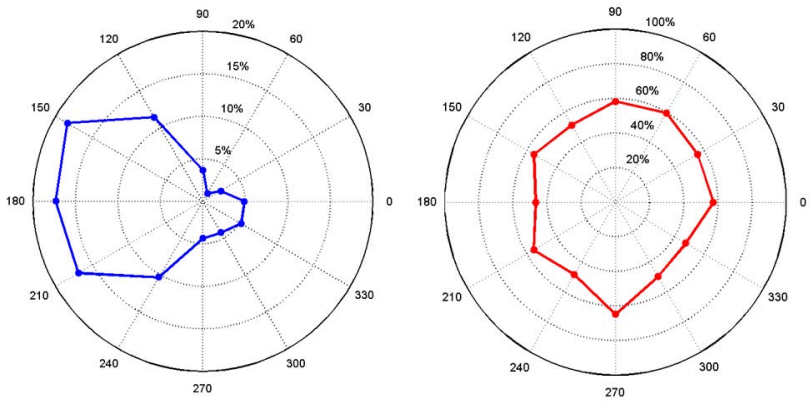

(a) (b)

Figure 5.7: (a) The distribution of EOBT B-scans and (b) the distribution of EOBT cases where the closest point to the ILM surface fell on the anterior surface of the border tissue.

Table 5.1: The Pearson correlation coefficients of RNFLT and different MRW measurements in all regions where only B-scans containing EOBT were included.

Region	RNFL–BMO_M	RNFL–BMO_A	RNFL–EOBT	RNFL–$EOBT_E$
Temporal	0.77	0.73	0.76	0.52
Superior	0.66	0.64	0.63	0.41
Nasal	0.40	0.43	0.40	0.35
Inferior	0.63	0.64	0.60	0.47

RNFLT ($p < 0.05$).

5.3 Discussion and Conclusions

While recent work has demonstrated benefits in using Bruch's membrane opening-minimum rim width (BMO-MRW) for the assessment of glaucoma, the frequent ambiguity in automatically detecting Bruch's membrane opening in the presence of externally oblique border tissue (EOBT) motivated us to define an alternative rim-width-based parameter in the presence of EOBT – externally oblique border tissue-minimum rim width (EOBT-MRW) – and to compare it with existing rim-width parameters. More specifically, in this chapter, we examined the structure-structure correlations of two recently proposed rim-width-based measures (Bruch's membrane opening-minimum rim width, BMO-MRW, and Bruch's membrane opening-horizontal rim width, BMO-HRW) and our newly proposed rim-width-based measure (EOBT-MRW) with retinal-nerve-fiber-layer thickness (RNFLT). Our experiments showed that in presence of EOBT, there was no significant difference between structure-structure correlations of BMO-MRW and EOBT-MRW with RNFLT. Furthermore, the correlation of BMO-MRW with RNFLT was higher than that of BMO-HRW, which indicates BMO-MRW better demonstrates the remaining neuroretinal rim tissue than BMO-HRW. This was expected as BMO-HRW, by definition, is not always the shortest distance to the ILM surface, which makes this measurement prone to overestimating the neuroretinal rim tissue. Our results are also consistent with the results of previous works [3, 109] that showed MRW is superior to for diagnosis of open-angle glaucoma [3].

Being able to use EOBT-MRW (a surface-to-surface measure) rather than BMO-MRW (a point-to-surface measure) is especially important when considering the options for providing automated MRW measurements (and for the evaluation of associated automated algorithms). In particular, if an algorithm is able to find the entire BM surface (including the EOBT extension), our data suggests that this should be

Table 5.2: The Pearson correlation coefficients of RNFLT with HRW and two MRW measurements in all regions where all B-scans were included.

	MRW		HRW
Region	**RNFL–BMO$_M$**	**RNFL–BMO$_A$**	**RNFL–BMO$_M$**
Temporal	0.64	0.65	0.43
Superior	0.61	0.66	0.55
Nasal	0.71	0.66	0.52
Inferior	0.62	0.62	0.44

sufficient for computing the MRW (as long as the MRW is computed by finding a surface-to-surface distance) rather than needing to precisely locate the BMO point. Because it is our experience that finding the entire surface (to include the EOBT extension) can sometimes be easier (for computers and humans) than finding the BMO endpoint, this is encouraging to allow for alternative means for automating the computation of the MRW. This also has implications for carefully considering how one should evaluate automated algorithms to segment the BMO when the final desired measurement is the MRW. For example, our automated approach detects the BM surface along with the opening (BMO_A) using a graph-theoretic approach [24]. This approach occasionally, when EOBT exists, segments the extension of border tissue as part of the BM surface and identifies the BMO_A along the anterior surface of border tissue (because of merging the BM surface endpoint with the extension of border tissue). In order to examine the MRW measure of the automated approach, we compared the MRW measures computed using manually identified (BMO_M) and automatically identified (BMO_A) BMO points. While all B-scans were included no significant difference was found between the structure-structure correlations of RNFLT with BMO_M-MRW and BMO_A-MRW.

It is important to note that our results are not suggesting that one can arbitrarily compute the MRW from any point along the EOBT and expect to have a measure

that is similar to that of the BMO-MRW; rather it should be measured at the point where the EOBT and ILM surfaces have the shortest distance from each other. To further demonstrate this, we measured the distance of the ending point of the border tissue (as an arbitrary point on the anterior surface of EOBT) to the ILM surface and compared the correlation with RNFLT of this measurement with that of BMO_M-MRW with RNFLT. The BMO_M-MRW had a significantly higher correlation than $EOBT_E$-MRW with RNFLT which indicates that the new MRW cannot be measured from an arbitrary point along the anterior surface of EOBT; rather, it must be computed from the shortest distance between two surfaces.

After all, as RNFLT is an imperfect indicator of true retinal ganglion cell axon tissue, utilizing RNFLT might not be the best way to compare the performance of different MRW measurements. Therefore, the current study does not suggest that EOBT-MRW has an equivalent glaucoma diagnostic performance to that of BMO-MRW. In addition, having a larger dataset containing greater number of scans with EOBT might enable us to find a significant difference between two MRW measurements.

In conclusion, although identifying the exact location of BMO for computing the point-to-surface shortest distance parameter (BMO-MRW) in presence of EOBT is difficult, the surface-to-surface shortest distance (EOBT-MRW), could be considered as a relaxed substitute for BMO-MRW as both parameters share the same intent of measuring the remaining neuroretinal rim tissue. This is expected to lead to more consistent and reliable automated approaches for computing minimum-rim-width in a clinical setting.

CHAPTER 6
MULTIMODAL REGISTRATION OF SD-OCT VOLUMES AND FUNDUS PHOTOGRAPHS USING HISTOGRAM OF ORIENTED GRADIENTS

Fundus imaging and spectral domain-optical coherence tomography (SD-OCT) are two common types of imaging modalities that provide different information about the human retina. Fundus imaging is referred to as the process of acquiring a 2D representation of the 3D retina by means of reflected light. With this definition, the broad category of fundus imaging includes modalities/techniques such as *red-free fundus photography*, *color fundus photography*, *stereo fundus photography*, *scanning laser ophthalmoscopy (SLO)*, and *fluorescein angiography* [50]. On the other hand, spectral-domain OCT, despite its recent appearance (the first SD-OCT device became commercially available less than 10 years ago [113]), has been the clinical standard of care for several eye diseases [50]. Both fundus and OCT imaging techniques are vastly utilized in diagnosis and management of eye diseases such as diabetic retinopathy, glaucoma, and age-related macular degeneration (AMD). Moreover, studies have shown that combining complementary information from both sources is beneficial for automated segmentation of retinal structures such as blood vessels [93] and optic disc and cup boundaries as discussed in Chapter 4. However, the performance of these multimodal segmentation approaches is dependent on the quality of the registration. For instance, in [93], a few scans were excluded from the test set due to relatively large registration errors.

As mentioned above, there are various techniques for retinal imaging each of which produces different types of images (i.e. with different size, resolution, and intensity profile) from the retina. There has been a great deal of effort through a variety of techniques on registering retinal images generated by different modalities [78–84, 86, 114–119]. Some of the previous works focused on stitching (mosaicing) images of the same modality with the aim of obtaining a broader field of view [85, 86, 115].

In contrast, there are works that attempted to register multimodal retinal images including fluorescence angiogram and red-free fundus pairs [78, 116, 120], SLO and color fundus photographs [90, 121], SD-OCT and color fundus photographs [22, 90–92, 122]. The focus of current work is on multimodal registration of fundus and SD-OCT modalities.

Generally, the pixel intensities between multimodal retinal image pairs might be different; however, compared to other types of multimodal retinal imaging, the intensity profiles of color fundus photographs and SD-OCT images are substantially different. Hence, in order to benefit from the most dominant structural information that both modalities share (i.e. retinal blood vessels), the current color fundus and OCT registration methods [22, 91, 92, 122] include a vessel segmentation step as part of their algorithms. The retinal vasculatures are the best candidates for identifying the corresponding points (e.g. blood vessel bifurcations and crossing points or blood vessel ridges) between two modalities.

However, the vessel segmentation errors, in either modality, could potentially introduce some errors to the registration process as the corresponding points between image pairs are identified from the blood vessel maps. For instance, the method proposed in [95] for blood vessel segmentation from SD-OCT modality could produce false positives due to the presence of the optic nerve head region [93]. Additionally, segmenting the blood vessels from both modalities is a time-consuming task which necessitates additional considerations (e.g. parameter tunning) when the dataset contains different fundus photographs (stereo and non-stereo fundus photographs) with different scales and sizes such as the one used in this work. The purpose of this work is to propose a feature-based registration method that is capable of aligning fundus and SD-OCT modalities without requiring blood vessel segmentation.

Feature-based registration methods have been used for aligning retinal images and demonstrated successful results [58, 85, 86, 119]. Control points detection is a

very important step in feature-based registration algorithms as the final landmarks that are used for computing the registration transformation, are selected from the CPs. We propose to identify the CPs by detecting the corners (i.e. points for which there are two different dominant edge directions in a local neighborhood of the point) in the images using features from accelerated segment test (FAST) corner detection approach [123, 124] which, as its name suggests, is very fast and computationally efficient.

In particular, the proposed method starts with a few preprocessing steps including: 1) creating a 2D projection image from the 3D SD-OCT volume, 2) enhancing the contrast of the images, and 3) rescaling the fundus photographs. Next, the control points, which are identified by FAST corner detection, are represented by a descriptor. More specifically, in order to avoid the use of intensity information and benefit from the structural features (i.e. retinal vasculature) without attempting to segment the blood vessels, histogram of oriented gradients (HOG) [125] is employed as the CP's descriptors. The approximate nearest neighbor method [126] is utilized in a forward-backward fashion to identify the matching descriptors. Finally, after removing the incorrect matches, the registration transformation is calculated using random sample consensus (RANSAC) method [127].

6.1 Methods

The overall flowchart of the proposed method is depicted in Fig. 6.1 and can be summarized in five major steps as follows: 1) a preprocessing step including SD-OCT projection image computation, contrast enhancement, and fundus images rescaling (Section 6.1.1), 2) identifying the control points (Section 6.1.2), 3) computing gradient-based features (Section 6.1.3), 4) feature matching (Section 6.1.4), and 5) calculating the transformation (Section 6.1.5).

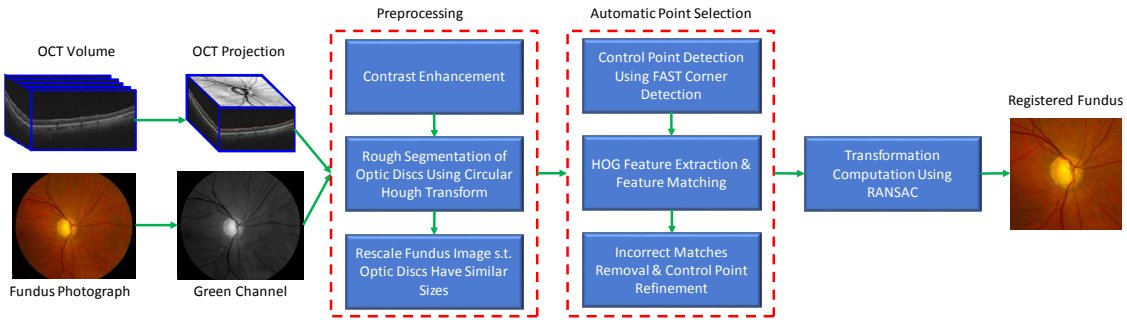

Figure 6.1: Flowchart of overall method.

6.1.1 Preprocessing

In order to be able to register the 2D fundus photographs to the 3D SD-OCT volumes, a 2D projection image of the volume is required. The OCT projection image is obtained using the method proposed in [16] where a multi-resolution graph-theoretic approach is employed to segment the intraretinal surfaces within the 3D SD-OCT volumes [16, 44] as discussed in Chapter 3. In order to obtain the projection image, two intraretinal surfaces are segmented: the junction of the inner and outer segments of photoreceptors (IS/OS) and the outer boundary of the Retinal Pigment Epithelium (RPE), also called the Bruch's membrane (BM) surface. A thin-plate spline is fitted to the BM surface from which the OCT volume is flattened to obtain a consistent optic nerve head shape across patients [44]. The SD-OCT projection image is computed by averaging the voxel intensities in the z-direction between the IS/OS junction and BM surfaces (Fig. 6.2).

Two types of color fundus photographs exist in the dataset used in this work: 1) stereo fundus images (Fig. 6.3a covering almost 20 degrees field of view), where the optic nerve head region of the retina is imaged from two different angles and placed side by side, and 2) ONH-centered non-stereo fundus photographs (Fig. 6.3b), which cover a broader field of the retina (35 degrees). For the stereo fundus photograph pairs, the image that has higher quality and less imaging artifact is selected to be

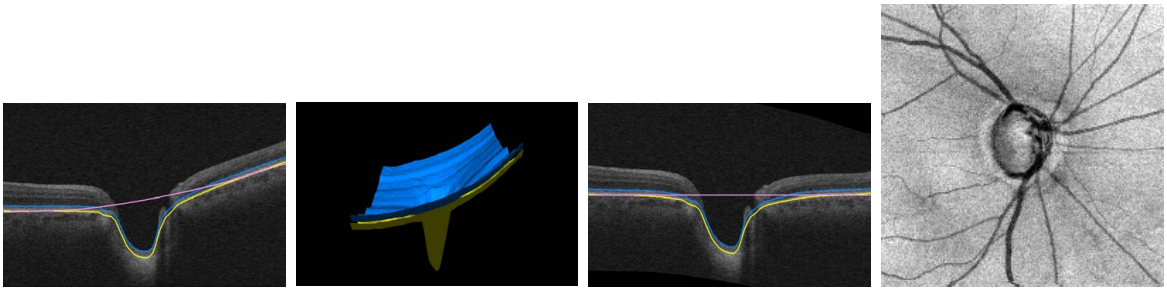

(a) (b) (c) (d)

Figure 6.2: An example of intraretinal surface segmentation. (a) The central OCT B-scan and the segmented surfaces: blue is the IS/OS junction, yellow is the BM surface, and pink is the thin-plate spline fitted to the BM surface. (b) The 3D view of the segmented surfaces. (c) The flattened OCT B-scan. (d) The corresponding OCT projection image.

considered for the registration. In addition, there is extra information included on the fundus photographs (e.g. dates, text, and color bars) which produce strong corners which could distract the registration process and so were automatically removed from the images. Here, a binary mask indicating the region of interest of each image was produced by thresholding the images following by a morphological opening operator (Fig. 6.3).

Furthermore, the blood vessels have the highest contrast in the green channel of the fundus photographs; hence only the information of the green channel was used in our method. The control points in the images were detected by looking for the corners, which are sensitive to the pixel intensities; therefore, in order to increase the chance of finding the best matching points, the number of CPs needs to be maximized. Consequently, the contrast of both fundus photographs (green channel) and the OCT projection images were enhanced and normalized using the contrast limited adaptive histogram equalization (CLAHE) method [128].

Since the images are from different modalities, they differ in size and resolution.

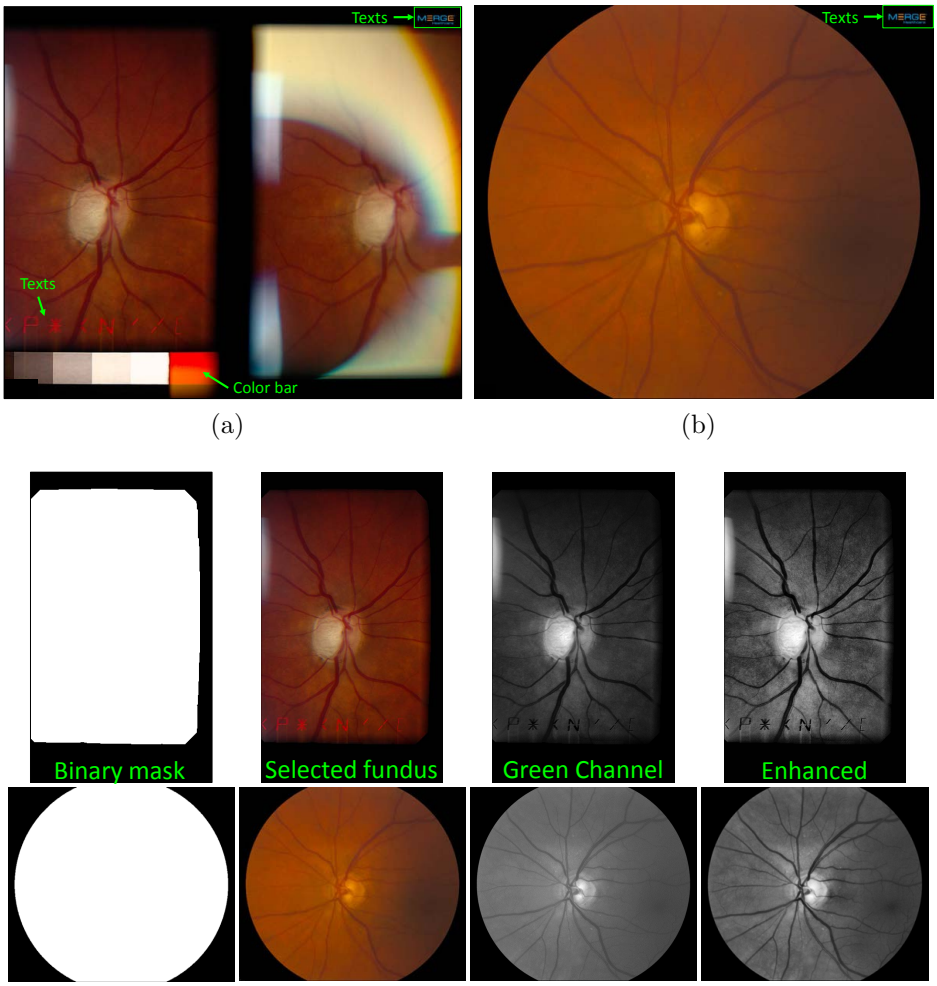

Figure 6.3: Example preprocessing steps on two types of fundus photographs in the dataset. The interfering details included on the images are shown with green arrows. Dates are covered for privacy. (a) Stereo fundus photographs containing large imaging artifact due to which the left-side photo was selected for further processing in (c). (b) A low-contrast regular fundus photograph. (c) The binary masks that remove the interfering details, the selected fundus image, the green channel, and the enhanced-contrast images corresponding to the examples shown in (a) and (b).

Moreover, the size and resolution of two types of fundus photographs in the dataset are completely different from each other. In order to bring all the images to a similar scale and resolution, the fundus photographs are scaled such that their optic disc has a similar size as the optic disc in their corresponding OCT projection image. Since the optic disc has roughly a circular shape, the location and size of optic disc in both modalities is approximated using a circular Hough transform. First, a grayscale morphological closing operator with a ball-shaped structuring element is applied to both enhanced images in order to remove the blood vessels (attenuate the dark features in the images). Subsequently, the gradient of the closed image is computed and the circular Hough transform is applied to the gradient magnitude image. The center and radius of the most dominant circle in the fundus (c_f, r_f) and OCT (c_o, r_o) images estimates the optic disc location and size in both modalities, respectively (Fig. 6.4). Since the resolution of the OCT projection images are consistent in the entire dataset, both stereo and non-stereo fundus photographs are scaled (according to their corresponding OCT projection images) such that $r_f = r_o$.

6.1.2 Control Point Detection

A control point (aka *interest point*) is a pixel which has a well-defined position and can be robustly detected. Two properties of interest points are having high local information content and repeatability between different images. Identifying sufficient number of CPs in images is a key in feature-based registration methods as lack of a sufficient number of CPs increases the risk of unsuccessful registration or decreases the robustness of the method significantly. Bifurcations are reasonable candidates to be utilized as CPs due to the fact that the blood vessels structure remain unchanged between modalities. However, obtaining bifurcations requires segmenting the blood vessels from both modalities which could be challenging in poor quality images. Hence, instead of looking for bifurcations, we proposed to utilize corners in images as the CPs. Features from accelerated segment test (FAST) [123, 124] was

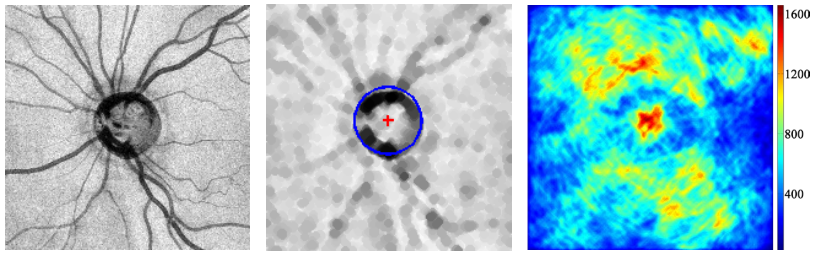

(a)

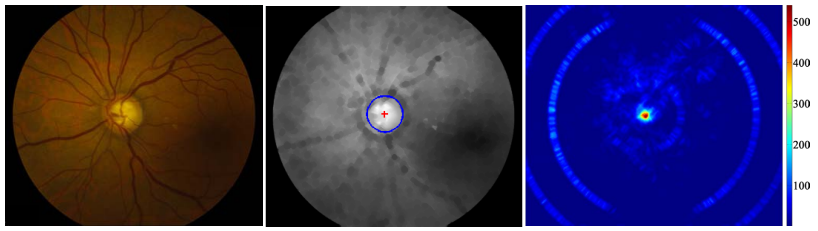

(b)

Figure 6.4: An example of optic disc localization using circular Hough transform. (a) From left to right are the enhanced OCT projection image, the blue circle representing the optic disc overlaid on top of the closed image, and the Hough map from which the dominant circle is identified, respectively. (b) The same sequence of images as in (a) showing identifying the optic disc from the fundus photograph.

employed to detect corners in the image as this method has a high accuracy and robustness and is able to find the corners very fast. Consequently, there is no need for vessel segmentation and by detecting corners, most of the bifurcations are also detected as they resemble corners in the images.

The FAST corner detection algorithm determines whether a pixel is a corner utilizing its neighboring pixel intensities. More specifically, consider an image I and a query pixel p, which is to be identified as a corner or not, with the intensity of I_p and also consider a Bresenham circle of radius 3 containing 16 pixels surrounding the pixel p [124]. The pixel p is identified as a corner if the intensities of N contiguous pixels out of the 16 are either above ($I_{\{N\}} > I_p + T$) or below ($I_{\{N\}} < I_p + T$) the intensity of the query pixel, I_p. T is a predefined threshold value and $I_{\{N\}}$ is the intensity of N contiguous pixels where $N \in \{9, 10, 11, 12\}$. The algorithm quickly rejects the pixels that are not a corner by comparing the intensity of pixels 1, 5, 9 and 13 of the circle with I_p (Fig. 6.5). If the intensities of at least three of these four locations are not above $I_p + T$ or below $I_p - T$, then p is not a corner, otherwise, the algorithm checks all 16 points. This procedure repeats for all pixels in the image. In order to avoid the distraction caused by the magnified background noise (produced in the contrast enhancement step) and obtaining so many corners on the background (especially for OCT projection image), a smoothing Gaussian filter is applied to the images before corner detection (Fig. 6.6).

6.1.3 Gradient-Based Feature Computation

The method proposed in this work for extracting features has similarities with SIFT descriptors and is inspired by the descriptor proposed in [125] for human detection. The basic idea behind the feature computation method is characterizing the local appearance of each CP's neighborhood by distribution of local intensity gradients or edge directions. More specifically, the neighborhood of size $MN \times MN$ around each control point is defined using small spatial *block* which is divided into

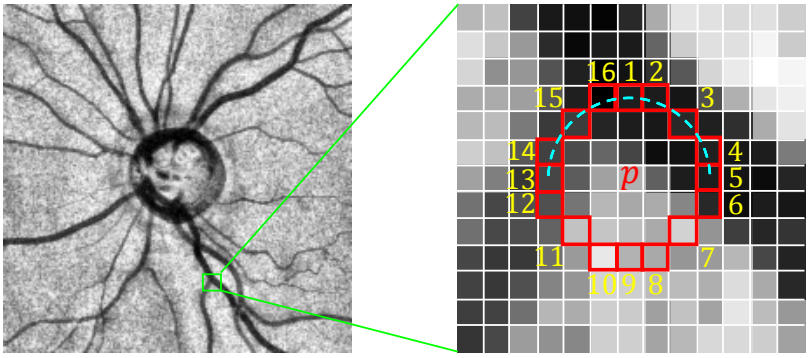

Figure 6.5: Illustration of Bresenham circle containing 16 pixels (the red boxes) around the query point p. An example of N contiguous pixels (for $N = 9$) is shown with the cyan dashed line [123].

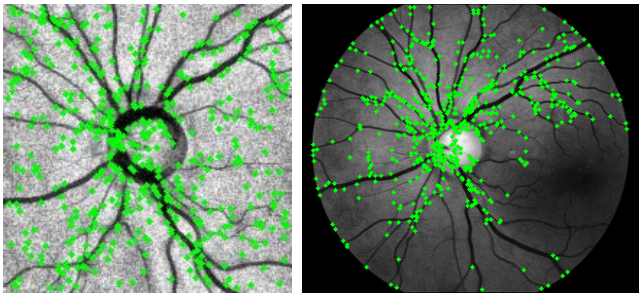

(a) (b)

Figure 6.6: An example of control point (corner) detection from (a) OCT projection and (b) fundus images using FAST corner detection method.

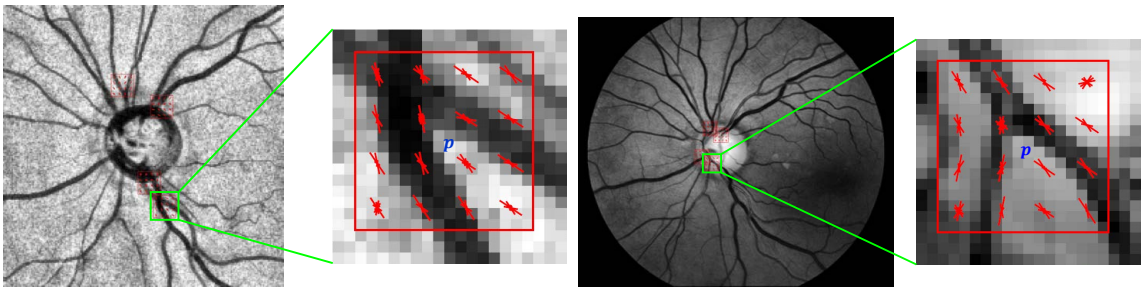

(a) (b)

Figure 6.7: An example of HOG descriptor computation from (a) OCT projection and (b) fundus images for a block size of 4×4 and a cell size of 4×4. The four strongest control points and their corresponding HOG blocks are shown on the left and for better visualization a zoomed-in illustration of one of the blocks with its corresponding CP (in blue) is shown on the right.

$N \times N$ smaller *cells* of size $M \times M$. The gradient direction and magnitude of all pixels inside each block are computed and for each cell in the block, a histogram of gradient directions (i.e. edge orientation) are computed such that the gradient directions are weighted by their corresponding gradient magnitudes. The gradient directions are limited to $[0°, 180°)$ and binned into 8 bins of $[0°, 22.5°, \ldots, 157.5°]$ (Fig. 6.7). Constraining the directions to 180° instead of 360° causes the histogram to be less distinctive, but at the same time, more robust to the intensity change which is quite possible between multimodal images. The histograms from all cells in the block are concatenated to form a 1-D vector of size $8 \times N \times N$. In order to further the invariance to affine changes in illumination and contrast, all histograms in a block are normalized such that the concatenated feature vector has a unit size. Therefore, the normalized concatenated vector, which includes the components of all normalized cell histograms in a block, is called the histogram of oriented gradient (HOG) descriptor and represents the local shape characteristics (e.g. gradient structure) of each CP's neighborhood.

6.1.4 Feature Matching

In order to find the best matching CPs between a pair of multimodal images, the method in [126] for identifying the approximate nearest neighbors in high dimensions was employed. The method eliminates ambiguous matches in addition to using the match threshold. A match is considered ambiguous when it is not remarkably better than the second best match. Assume $H_f = \{h_{f,1}, h_{f,2}, \ldots, h_{f,N}\}$ and $H_o = \{h_{o,1}, h_{o,2}, \ldots, h_{o,M}\}$ represent the sets of HOG feature vectors from fundus and OCT images, respectively. Here is how the best matching feature from H_o corresponding to $h_{f,1}$ is identified:

- First, the sum of squared differences between $h_{f,1}$ and all vectors in H_o is computed as in Eq. 6.1. The feature vectors having a distance larger than a match threshold (here 0.2) are eliminated from further investigation.

$$D_{FO}(1,i) = \sum_{j=1}^{128} \left[h_{f,1}(j) - h_{o,i}(j)\right]^2 \ , \ i = 1, 2, \cdots, M. \tag{6.1}$$

- The ambiguous match ratio is calculated by dividing the distance of second nearest neighbor feature vector by the distance of first nearest neighbor feature vector.
- If the match ratio between the two distances is smaller than a predefined ratio threshold, the match is considered ambiguous and eliminated.

The method iterates over H_f until all feature vectors are examined. Even though this approximate nearest neighbor method produces more reliable matches, if the images contain repeating patterns (which is not the case for retinal images), the corresponding matches are likely to be eliminated as ambiguous. In order to be more conservative, the ratio threshold was set to 0.8 in this study.

Identifying the match pairs utilizing the method described above had the potential to result in assigning a feature vectors from H_o to multiple feature vector from H_f

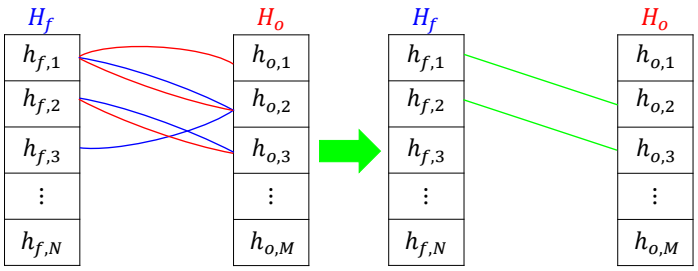

Figure 6.8: Illustration of feature vector matching using approximate nearest neighbor method in forward (blue) and backward (red) modes. The final matching feature vectors set (green) only includes the common pairs between forward and backward modes.

due to the fact that the iterations are performed independently from each other. In order to solve this issue and identify unique matches, a forward-backward search is performed. Hence, in the backward mode, the same procedure applies to H_o and the best matching feature vectors from H_f are identified. The set of final matching pairs, $\mathcal{S}$, includes only the unique matches which are common between forward and backward modes (Fig. 6.8).

6.1.5 Transformation Computation

The set of matching CP pairs detected in Sec. 6.1.4 are utilized to compute the transformation matrix. However, the algorithm does not guarantee 100% accuracy in matching CPs which results in possible incorrect matches. Therefore, the incorrect matching pairs are identified using the geometrical distribution of all matching pairs. Assume $\mathcal{S}^{1\times L} = \left\{ \left(p_f(x_1, y_1), p_o(x_1, y_1)\right), \ldots, \left(p_f(x_L, y_L), p_o(x_L, y_L)\right) \right\}$. Then, the Euclidean distance between all CP pairs, $dist^{1\times L}$, in the image domain as well as the mean, $dist_m$, and standard deviation, $dist_{sd}$, of the distance vector are computed. Consider a pair, $(p_f(x_i, y_i), p_o(x_i, y_i))$, and its corresponding distance, $dist^{(i)}$. If the points are too close to each other ($dist^{(i)} < dist_m - dist_{sd}$) or too far from each other ($dist_m + dist_{sd} < dist^{(i)}$), the pair is marked as an incorrect matching pair (Fig. 6.9). Here, in order to be more conservative and keep the high quality matches, the points

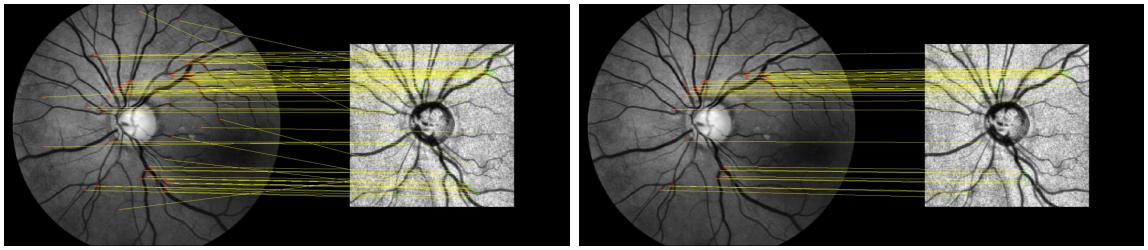

(a) (b)

Figure 6.9: An example of incorrect pair removal. (a) Shows the yellow lines connecting the corresponding matching pairs between images identified using the approximate nearest neighbor described in Sec. 6.1.4. The incorrect pairs are eliminated in (b).

with the distance of only one standard deviation from the average distance, $dist_m$, were marked as outliers. Identifying the incorrect matching pairs using this procedure is achievable under the assumption that the number of correct pairs are more than incorrect pairs and the images are in similar scales, there is no reflection involved, and the rotation needed to align the multimodal retinal images is minimal.

In addition to removing the incorrect matches, a refinement step is applied to the CP pairs which allows for small adjustments of CP locations within a small neighborhood of each CP (5×5 window). The refinement step exists for two reasons: 1) to account for possible errors in corner (CP) detection due to presence of noise, imaging artifacts and low contrast and 2) since the images come from two different modalities with significantly different intensity profiles, it is possible that pixels in the neighborhood of the CP are actually better matching candidates than the CP itself. Thus, the HOG feature vector is computed for all 25 pixels inside each CP's neighborhood (in both modalities) and the two feature vectors with minimum distance in the feature space are identified and their corresponding pixels are considered as the *new* CPs. Note that, both, one, or none of the CPs could be updated through the refinement step.

Table 6.1: Quantitative evaluation of the registration using RMS error. All cases are included.

Methods	mean±SD (mm)	mean±SD (p)	max (mm)	max (p)
ICP registration [22]	0.110±0.063	3.67±2.13	0.406	13.54
Manual	0.030±0.025	1.02±0.85	0.157	5.23
Proposed method	0.055±0.039	1.85±1.29	0.264	8.81

In order to estimate the affine transformation, random sample consensus (RANSAC) method is utilized [127]. Despite removing the incorrect matches from the matching set, the chance of presence of incorrect matching CPs is not zero. Therefore, the objective is to robustly calculate the transformation from $\mathcal{S}$ which may contain outliers (i.e., low-quality or incorrect matches). The algorithm performs as follows:

1. Randomly select a subset of three pairs s from $\mathcal{S}$ and instantiate the affine transformation from this subset. Here, the sampling is with replacement.
2. Apply the transformation to the rest of pairs in the set and determine the set of pairs $\mathcal{S}_i$ which distance of the transformed control point in fundus image, $\hat{cp}_f$, from its corresponding control point in OCT image, cp_o, is less than a predefined threshold. The set $\mathcal{S}_i$ is the consensus set of the sample and defines the inlier pairs of $\mathcal{S}$.
3. Repeat the previous two steps a large number of times and select the largest consensus set $\mathcal{S}_i$. The affine transformation is re-estimated utilizing all the CP pairs in the subset $\mathcal{S}_i$ [127].

6.2 Experimental Methods

6.2.1 Data

The performance of the proposed method was evaluated on a multimodal dataset including color fundus photographs and the SD-OCT volumes of of 44 open-angle glaucoma or glaucoma suspect patients. The optic nerve head (ONH)-centered SD-

OCT volumes were acquired using a Cirrus HD-OCT device (Carl Zeiss Meditec, Inc., Dublin, CA) in one eye (per patient) at the University of Iowa. Each scan has a size of 200×200×1024 voxels (in the x-y-z direction, respectively) which corresponds to a volume of size 6×6×2 mm^3 in the physical domain, and the voxel depth was 8 bits in grayscale. Additionally, the optic disc region of each patient's retina was also imaged using a fundus camera. Almost half of the patients (twenty-four) were imaged using a stereo-base Nidek 3-Dx stereo retinal camera (3072×2048 pixels). The remaining twenty patients had regular color fundus photograph acquired using a Topcon 50-DX camera (2392×2048 pixels). The pixel depth was 3 8-bit red, green and blue channels. Some of those pairs were taken at the same day, while others were taken months or even more than a year apart.

6.2.2 Experiments

Since we are registering multimodal images with completely different intensity profiles, in order to quantitatively evaluate the proposed method, the intensity-based metrics are avoided and the evaluation is performed using point-based metrics. The reference standard needed for the point-based evaluation is obtained by identifying a set of landmark pairs from the original images manually. In order to assure the collection of appropriate landmarks capable of a fair evaluation, we marked five pair of points that were not too close to each other and as much as possible were fairly distributed. The manual landmarks are mostly selected from the vasculature regions that create unique and recognizable points in both images such as corners and bifurcations. The manual registration was performed by computing the affine transformation using three randomly selected pairs from the set of landmarks identified for the evaluation purpose.

In order to present comparative results, in addition to the manual registration, the performance of the proposed method was also compared to our previous iterative closest point (ICP) registration approach reported in [22] and used in Chapter 4.

The ICP-based method does not use the intensity information; however, as part of the algorithm, blood vessels need to be extracted and the registration transformation is actually computed using the vessel maps. The registration accuracy was evaluated using root mean square (RMS) error which measures the amount of misalignments between the manual landmarks of OCT images and their corresponding transferred landmarks of fundus photographs:

$$RMS = \sqrt{\frac{1}{5}\sum_{i=1}^{5}\left\|p_{o,i} - \hat{p}_{f,i}\right\|^2}\ , \tag{6.2}$$

where $p_{o,i}$ and $\hat{p}_{f,i}$ are the i-th manual point in OCT image and its corresponding transferred manual point in the fundus photograph, respectively. The mean, standard deviation, and the maximum of RMS errors of the manual and automated approaches were compared. Furthermore, the running time and the success rate of the registration methods were compared to each other. The registration was considered successful if the RMS error was less than or equal to 10 pixels (0.3 mm). The running time of the manual registration includes the required time for manual landmark identification and transformation computation. All experiments were performed using a PC with Windows 7 64-bit OS, 64 GB RAM, and Intel(R) Xeon(R) CPU 3.70 GHz.

6.3 Results

Fig. 6.10 shows the comparative results of registering two pairs of fundus (stereo and non-stereo) and OCT images using ICP, manual, and the proposed methods. The checkerboard images are provided for qualitative comparison of the registration results. Quantitatively, the mean, standard deviation, and the maximum RMS error calculated using the entire dataset is reported in Table 6.1. Based on the RMS values, the manual registration and the proposed method had significantly smaller errors than the ICP registration method ($p < 0.05$). However, the RMS errors of the manual registration were not significantly different from the proposed method

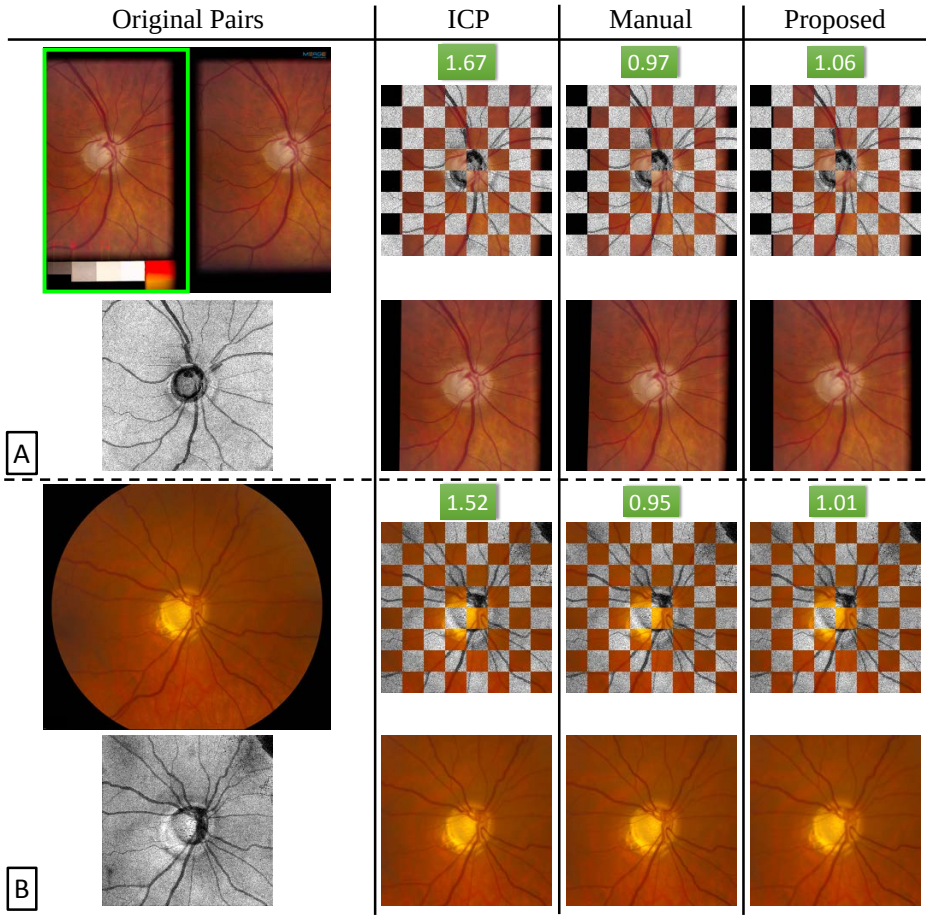

Figure 6.10: Examples of successful registration results using ICP [22], the manual, and the proposed methods. The green frame in (A) indicates the left image was selected for the registration. The checkerboard of the registered pairs are also provided for qualitative comparison of the registration results. The corresponding RMS errors of the methods are also shown in the green boxes.

($p < 0.05$).

The success rate and the running time of the registration methods are reported in Table 6.2. Similar to the manual registration, the proposed method achieved a 100% success rate; however, the ICP registration method failed to successfully register five cases. The running time of the proposed method was significantly lower than the manual and the ICP registration methods ($p < 0.5$). Similarly, the running time of the ICP registration method was significantly smaller than the manual registration

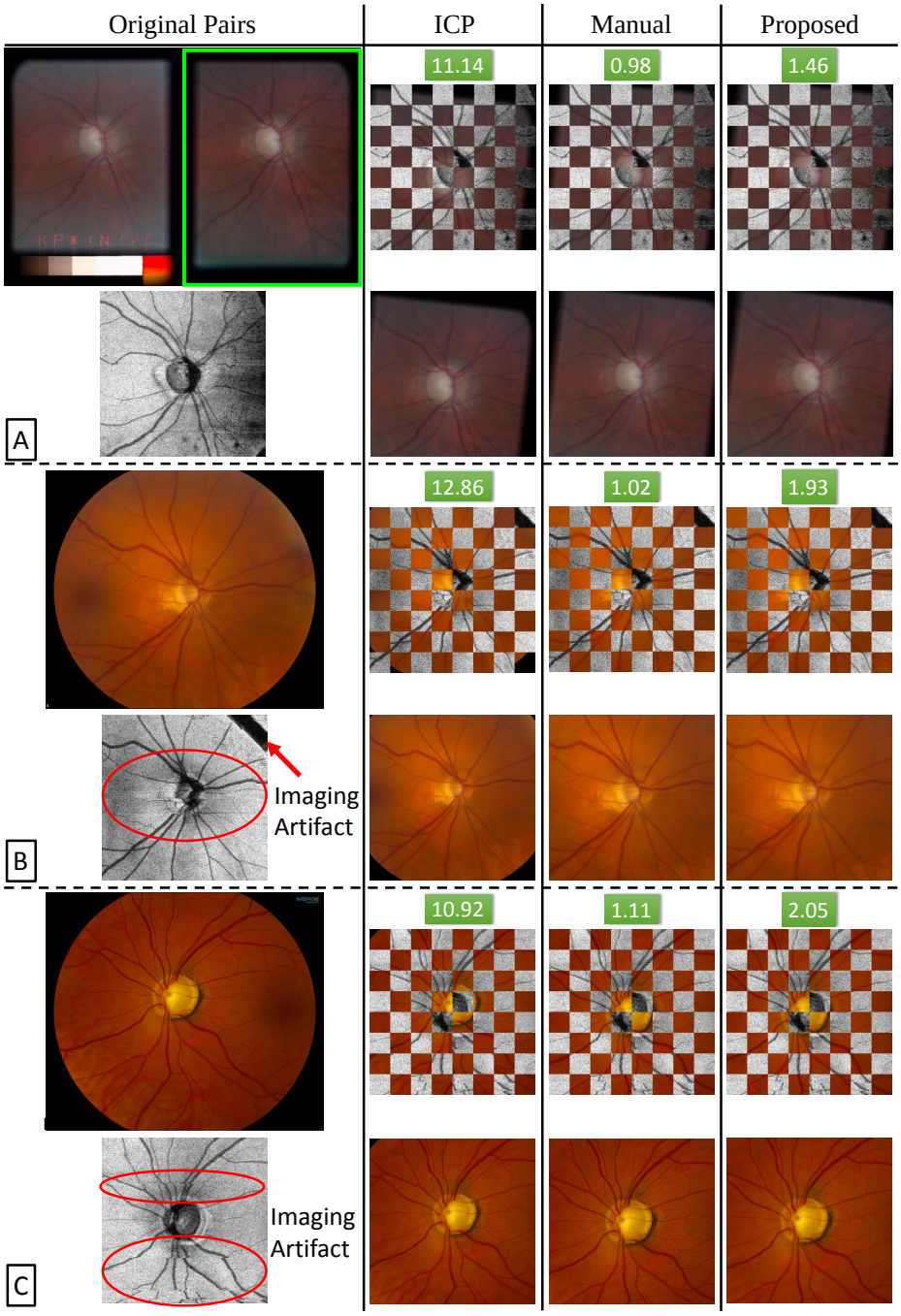

Figure 6.11: Examples of failed registration (RMS error > 10) using ICP method where the manual and proposed methods did not fail. Low imaging quality in (A) and the motion artifacts (located inside the red ovals) in (B) and (C) also caused a larger registration errors for the proposed methods. The corresponding RMS errors of the methods are also shown in the green boxes.

Table 6.2: The success rate and running time (s) computation.

Methods	success rate (%)	running time (s)
ICP registration [22]	88.64	28.45
Manual	100	75.71
Proposed method	100	2.34

($p < 0.05$). Additionally, Fig. 6.11 shows ICP registration failures (i.e. the RMS error was greater than 10 pixels) due to having low imaging quality and presence of motion artifact in OCT projection image. The manual and the proposed methods did not fail; however, they produced slightly larger registration errors.

6.4 Discussion and Conclusion

In this chapter, we proposed a feature-based registration method for aligning optic nerve head-centered SD-OCT volumes and fundus photographs. Since the intensity of the images are substantially different, the registration needs to rely only on the structural features that the image pairs have in common. Whereas previously proposed fundus and SD-OCT registration approaches often include a vessel segmentation step as part of their algorithms where the errors in vessel segmentation could potentially propagate into the registration process as well, in this work, we employed the histogram of oriented gradient features to capture the structural information in the images so as not to require the segmentation of blood vessels. Eliminating the vessel segmentation step is beneficial as it prevents propagating the possible segmentation errors (e.g. false positives in the vessel maps near the optic disc [93]) to the registration process. Additionally, removing the vessel segmentation step reduces the required time for registering the fundus and OCT image pairs.

In addition to significant intensity change between image pairs, which is one item that differentiates fundus/SD-OCT registration from other types of retinal image

registration, existing very low-contrast fundus photographs and presence of extra text information on the stereo fundus photographs when the second pair is not available (Fig. 6.10.A) and the presence of imaging artifacts in SD-OCT projection images cause the registration to be more challenging. Since acquiring SD-OCT volumes takes a few seconds, the OCT projection images could suffer from motion artifact (Fig 6.11.B and 6.11.C). Volume truncation is another type of SD-OCT imaging artifact which appears as a black region in the projection image (Fig 6.11.B) and causes the registration to be difficult. However, since the transformation matrix is computed using RANSAC algorithm with enough number of matching CPs between two modalities, our proposed method was able to successfully manage the imaging artifacts.

Additionally, our proposed method needs on average less than 3 seconds to perform the registration which is considerably fast. The most time consuming part of typical feature-based registration algorithms is identifying the control points for which all pixels in both images need to be examined. However, utilizing FAST corner detection for identifying the control points in our proposed method has the advantage of quickly rejecting the pixels that are not corners using a computationally efficient test on the neighboring pixels of the query pixel.

Furthermore, the proposed method is capable of registering the macular-centered OCT volumes and fundus photographs which do not contain the optic nerve head region. Since the optic disc appears differently in OCT projection images and fundus photographs, absence of optic disc makes registering the macular-centered retinal images less challenging. Moreover, the applications of the proposed method could potentially be extend to retinal mosaicing and registering other multimodal retinal images such as fluorescein angiography, SLO, and red-free fundus photographs. Our proposed method could also be extended for the registration of other image pairs, such as corneal nerve images.

Even though the histogram of orientated gradient features are not rotationally invariant, they were suitable for registering the multimodal retinal images in our dataset, due to the fact that both modalities are acquired in the optic nerve head-centered mode and therefore, significant rotations are not required for aligning image pairs. However, employing the proposed method in other applications, where rotation is necessary to register two images, requires replacing HOG with relative HOG (RHOG) features which are rotationally invariant as they are computed with respect to the main orientation of the control points. The main direction of each CP is obtained by computing the resultant of gradient directions of all pixels inside the neighborhood of each CP using a 2D Gaussian kernel.

In summary, our proposed feature-based registration method was capable of registering stereo and color fundus photographs to their corresponding SD-OCT projection images. In particular, after creating the 2D projection image from the SD-OCT volume, the contrast of the both modalities were enhanced and the fundus photographs were scaled such that the size of optic discs, which was approximated using a circular Hough transform, in both images became similar. Next, FAST corner detection was utilized to identify the control points in both images. The histogram of oriented gradients was capable of capturing the structural profile of each CP's neighborhood without segmenting the blood vessels. In order to identify the best matching CPs, an approximate nearest neighbor method was utilized in the forward-backward mode which determines the best matching CPs by calculating the distances descriptors in the feature space. After removing the incorrect matches and refining the CP locations, the best affine transform that registered the image pairs was calculated using RANSAC algorithm. Our feature-based registration method is very fast and outperformed our previous ICP registration method described in Chapter 4.

CHAPTER 7
INCORPORATION OF GRADIENT VECTOR FLOW FIELD IN A MULTIMODAL GRAPH-THEORETIC APPROACH FOR SEGMENTING THE INTERNAL LIMITING MEMBRANE FROM GLAUCOMATOUS OPTIC NERVE HEAD-CENTERED SD-OCT VOLUMES

The content of this chapter is presented in [129]. The top surface of the retina and optic nerve head is called the internal limiting membrane (ILM) and is utilized for measuring several structural parameters such as Bruch's membrane opening-minimum rim width (BMO-MRW), total retinal thickness, and cup volume. Besides computing structural parameters from SD-OCT volumes, having a precise ILM surface segmentation is also necessary for extracting different features from SD-OCT volumes in approaches that utilize machine learning-techniques for segmenting different retinal structures such as retinal blood vessels, BMO points, optic disc, and optic cup [16, 22, 88, 102].

There has been a great deal of research in segmenting the intraretinal surfaces including machine-learning based approaches [34–36], model based approaches [38, 40], and graph-based approaches [16, 24, 41, 44, 130]. However, precisely segmenting the ILM surface in optic nerve head (ONH)-centered OCT, as needed for computing parameters such as the BMO-MRW of glaucoma patients, is more challenging than segmenting the ILM from a macular-centered OCT volume. The reason is that, due to the presence of deeper cups in glaucoma patients, the morphology of the ILM surface in the ONH region is very different from that of the macular region. Hence, many graph-based segmentation approaches [16, 44] initially designed to segment the intraretinal layers of the macula or the peripapillary region surrounding the ONH cannot catch the deep, steeply sloped cups which are characteristics of a glaucomatous ONH. This is due to the fact that the corresponding graph of the OCT volume is constructed such that each A-scan corresponds to a column in the graph and the ILM surface must intersect with each column only once. However, precise segmentation of

the ILM surface inside the large and deep cups, present in glaucomatous OCT volumes, requires to intersect with each A-scan multiple times or to allow for sharp and large transitions (Fig. 7.1a). Shah *et al.* proposed a graph-theoretic segmentation method using the range expansion algorithm such that the sharp transitions were not penalized heavily [130]. More specifically, a truncated convex function was utilized for controlling the surface smoothness which allowed to preserve the discontinuity of the ILM surface while encouraged the smoothness. Even though this method improved the performance of its previous generations (i.e. [16, 44]) in segmenting the ILM surface within deeper cups, however, there is a trade-off between preserving discontinuity and obtaining a smooth ILM segmentation. Furthermore, the approach did not allow for multiple intersections with A-scans. Consequently, in the presence of steep slopes, many current ILM segmentation approaches would lead to underestimation of measurements such as cup volume (the volume between the ILM surface and the BMO reference plane) as shown in Fig. 7.1b and overestimation of measurements such as minimum-rim width.

In addition to the presence of steep slopes, the presence of large retinal blood vessels, which is characteristic of the ONH region, causes the accurate segmentation of the ILM surface to be difficult. The large blood vessels located closer to the top surface of the retina are able to change the topology of the ILM surface. Since the current segmentation approaches include the retinal blood vessels as part of the ILM surface, as a result, the gaps surrounding the blood vessels may include as part of the ILM surface as well which leads to overestimating the BMO-MRW or underestimating the cup volume (Fig. 7.2b).

In order to address the segmentation errors mentioned above, we incorporated the gradient vector flow (GVF) field [131] in a multimodal graph-theoretic approach to enable dealing with deep cupping as well as retinal blood vessels. In another application domain, Oguz *et al.* benefited from GVF field by proposing a graph-

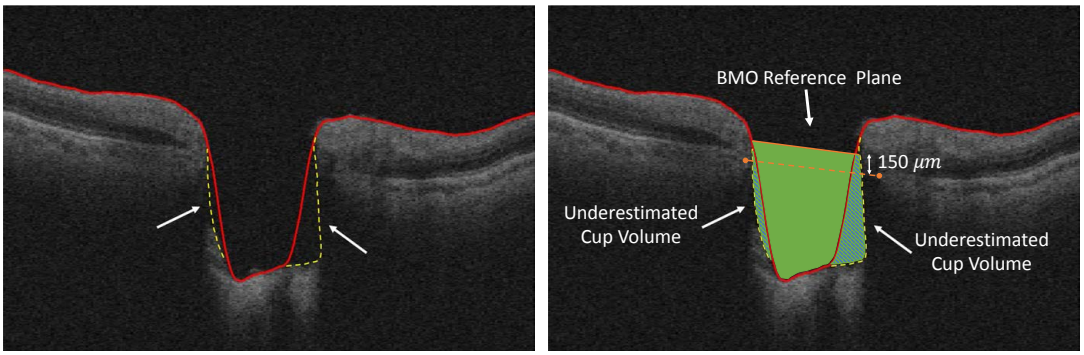

(a) (b)

Figure 7.1: (a) ILM segmentation error due to the steep slopes as well as low signal strength. The red lines indicate segmentation results using the approach of Lee *et al.* [16] and the yellow dashed lines indicate the desired segmentation. (b) The resulting underestimated cup volume. The solid green region is the measure cup volume using automated ILM segmentation and the underestimated regions are shown with shaded patterns.

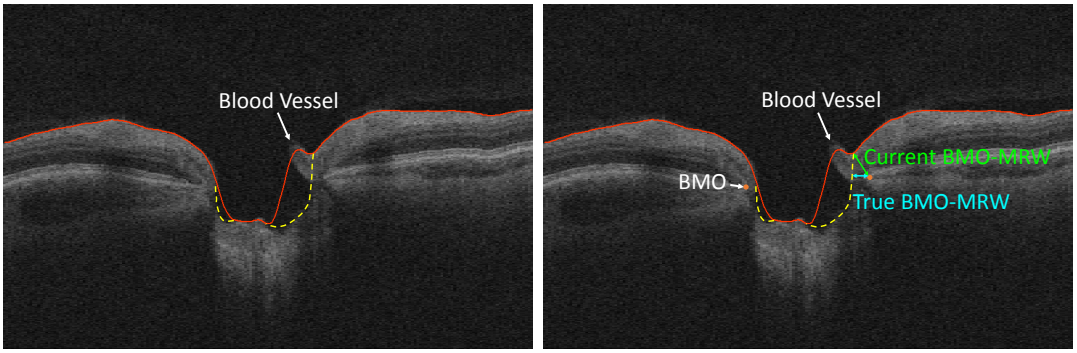

(a) (b)

Figure 7.2: (a) ILM segmentation error due to the presence of blood vessels. The red lines indicate segmentation results using the approach of Lee *et al.* [16] and the yellow dashed lines indicate the desired segmentation. (b) The resulting inaccuracy in computing the BMO-MRW structural parameter. Underestimating the cup volume because of including the blood vessel in the ILM segmentation is also observed.

theoretic method for segmenting multiple objects and surfaces of the brain where in order to be able to segment the complex-topology surfaces of the brain, the columns in graph construction were obtained by computing the GVF field. Similarly, in order to allow for steep and deep cupping, we benefited from the direction of the GVF field to construct a new set of equally spaced columns along the normals of the ILM surface. Since the columns in the graph construction must be non-overlapping (otherwise it may lead to a self-intersecting surface segmentation) and GVF-based columns satisfy this condition, the OCT volume was resampled using the new GVF-based columns which also served as the columns in the graph construction.

In order to compute the GVF field, an initial ILM segmentation is required which was computed using a multiresolution method. Since the GVF-based columns are perpendicular at the initial ILM segmentation, the ILM surface in the resampled volume does not contain any steep slope or deep cupping, hence, we segment the ILM surface using a graph-theoretic approach by incorporating prior shape information [76]. The blood vessels are dealt with by correcting the initial segmentation as well as modifying the cost function that was used in the graph-based segmentation at the blood vessel locations. Since the blood vessels are more visible in fundus photographs (especially inside the ONH), they are segmented from registered fundus photographs. Based on the survey conducted by Kafieh *et al.* [132], the graph-theoretic approach proposed by Lee *et al.* is one of the best existing intraretinal approaches and will be used in this work for comparison purposes.

7.1 Methods

The flowchart of the proposed method is shown in Fig. 7.3. There are four major steps in the proposed method including: 1) preprocessing, 2) computing initialization and blood vessel correction, 3) computing GVF-based columns, and 4) identifying the ILM surface using a graph-theoretic method.

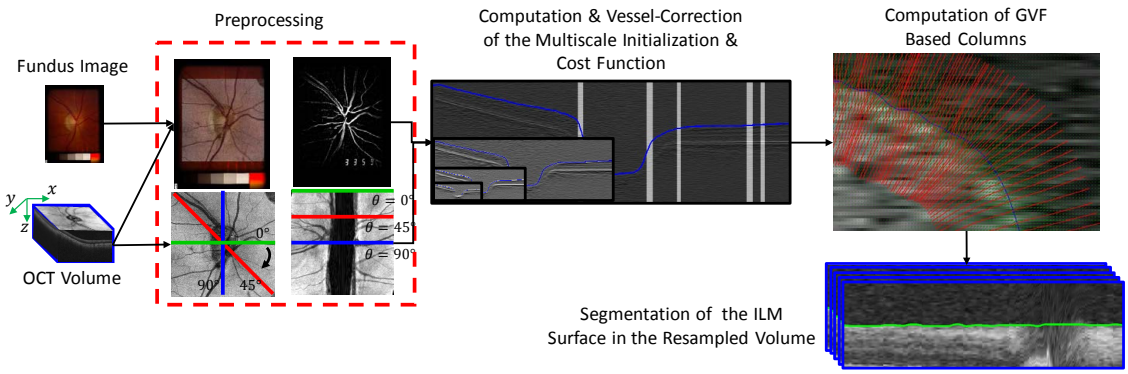

Figure 7.3: Flowchart of proposed algorithm.

7.1.1 Preprocessing

Due to better visibility of the retinal blood vessel inside ONH in fundus photographs than in SD-OCT projection images, the blood vessels are segmented from fundus photographs [94]. In order to be able to map the blood vessel mask to SD-OCT volumes, the fundus photographs need to be registered to their corresponding SD-OCT volumes. A 2D projection image is created from SD-OCT volume by segmenting the intraretinal layers and averaging the intensities within the retinal pigment epithelium (RPE)-complex subvolumes in the z-direction [16]. The fundus photographs are registered to the 2D projection images using the method described in Chapter 6.

Additionally, in order to obtain a more consistent shape of the ILM within ONH region across all slices, the SD-OCT volume is transferred from the Cartesian domain $(x \times y \times z)$ to the radial domain $(r \times \theta \times z)$ with angular resolution of one degree, which results in 180 radial B-scans. The computed retinal blood vessel mask is also transferred to the radial domain.

7.1.2 Initialization

In order to compute the initial ILM segmentation required for calculating the GVF field, a simple and fast, but reasonably accurate, multiresolution gradient-based

peak detection method was utilized. The GVF-based columns are computed based on the location of the initialization, but they extend on both sides of the initial segmentation such that a sufficiently large band around the initial segmentation is covered, hence, a rough segmentation of the ILM surface is sufficient. Since a simple peak detection method is utilized to identify the initialization, the speckle noise of the images must be suppressed otherwise, the initialization may include discontinuities along the surface. Therefore, the peak detection is performed in multiple resolutions where downsampling the volume (by a factor of 2) to three lower resolutions reduces the speckle noise of the image significantly. The boundary of retina and vitreous body appears as a strong edge in OCT volumes and in order to capture this dark-to-bright transition, where the ILM surface generates a large response, the OCT volume at each level, $I^{(i)}$, was convolved with an asymmetric 3D Gaussian derivative filter as follows:

$$\mathcal{E}^{(i)}(r,\theta,z) = \frac{\partial}{\partial z}\left[\frac{1}{2\pi\sigma_r^i\sigma_\theta^i\sigma_z^i}\, e^{-\left[(\frac{r}{\sqrt{2}\sigma_r^i})^2+(\frac{\theta}{\sqrt{2}\sigma_\theta^i})^2+(\frac{z}{\sqrt{2}\sigma_z^i})^2\right]}\right] * I^{(i)} \;\;,\;\; i\in\{0,1,2,3\} \;\;, \tag{7.1}$$

where σ_r^i, σ_θ^i, and σ_z^i are the standard deviation of the Gaussian filter in the i-th level in r, θ, and z, respectively. As it is depicted in Eq. 7.1, the derivative is performed only in z-direction, however, in order to incorporate the contextual information from surrounding regions and neighboring slices, the filter was designed in 3D. Since the first dominant high response from the top of each A-scan belongs to the ILM surface, the peak detector identifies the location of first peak at each A-scan within the lowest resolution, $\mathcal{E}^{(3)}(r,\theta,z)$. While the entire A-scan was included for detecting the peaks in the lowest resolution, in the next resolution instead of the entire A-scan, the searching interval includes only a small portion of the A-

scan relative to the location of the peak in the previous lower resolution. Besides the noise cancellation, the other advantage of obtaining the initialization through a multiresolution process is that constraining the possible surface locations in the subsequent resolutions helps avoid finding edges produced by other surfaces.

Since the presence of blood vessels may affect their surrounding regions as well, the radial blood vessel mask computed in section 7.1.1 was dilated by 2 pixels and mapped on the initialization such that the surface segmentation at the A-scans containing blood vessel was ignored and a cubic interpolation was used to compute the new values at these locations. The vessel-corrected initial segmentation, $\mathcal{S}_{\text{initial}}(r, \theta)$, is used in section 7.1.3 for computing GVF field. Furthermore, the response of the 3D Gaussian filter in the original resolution, $\mathcal{E}^{(0)}(r, \theta, z)$, is used as part of the cost function computation of the graph-theoretic approach in section 7.1.4.

7.1.3 Gradient Vector Flow Computation

In the cases of deep cupping, in order to be able to follow the steep slopes, we resample the volume using a set of equally spaced non-overlapping columns which are perpendicular to the initialization surface. Since the new columns are also used as the columns in the graph construction, these columns are computed by following the direction of the gradient vectors to assure non-overlapping columns. If an SD-OCT volume in the radial domain is represented by $I(r, \theta, z)$, GVF is the vector field $\vec{V}(r, \theta, z) = \big[u(r, \theta, z), v(r, \theta, z), w(r, \theta, z)\big]$ that minimizes the energy function E [131]:

$$E = \int\int\int \mu |\nabla \vec{V}|^2 + |\nabla I|^2 |\vec{V} - \nabla I|^2 dr d\theta dz \ , \tag{7.2}$$

where μ is the regularization parameter. Due to the smooth shape of ONH, μ was not a sensitive parameter for computing GVF field and was set empirically to 0.02.

The vector field in Eq. 7.2 can be found by solving the following Euler equations:

$$\begin{aligned} \mu\nabla^2 u - (u - I_r)|\nabla I|^2 = 0 \,, \\ \mu\nabla^2 v - (v - I_\theta)|\nabla I|^2 = 0 \,, \\ \mu\nabla^2 w - (w - I_z)|\nabla I|^2 = 0 \,, \end{aligned} \tag{7.3}$$

where $\nabla I = (I_r, I_\theta, I_z)$ and I_r, I_θ, and I_z are the derivatives in r, θ, and z directions, respectively. Therefore, an initial vector field, ∇I, with high gradient at the initial segmentation is required in order to be able to compute the appropriate GVF field. The initial vector field, ∇I, is derived from the following 3D binary function $I(r, \theta, z)$:

$$I(r,\theta,z) = \begin{cases} 0, & \mathcal{S}_{\text{initial}} > z \\ 1, & \mathcal{S}_{\text{initial}} < z \end{cases} . \tag{7.4}$$

Constructing the GVF-based columns starts from a point on the initial surface $\mathcal{S}_{\text{initial}}(r, \theta)$, and continues by following the directions of the gradient flow on both sides of the initial surface. In order to find the next point on the column, the direction and the step size need to be determined. The direction of all normalized gradient vectors in the neighborhood of the current point (i.e. $\left\{\vec{V}_i/|\vec{V}_i| \mid i \in \mathcal{N}_c\right\}$ where $\mathcal{N}_c$ represents the neighborhood) are interpolated to find the resultant direction, $\vec{V}_R$. In order to avoid sampling artifacts, the step size, s, must be smaller than half of the distance between two voxels in the volume. Therefore, moving in the direction of $\vec{V}_R$ with step size s indicates the next point on the column and assures obtaining non-overlapping columns. There is no limit on the length of the GVF-based column and the next points are obtained by continuously moving in the direction of the gradient flow at both sides of the initial surface. The length of the columns set to 100 in this study (Fig. 7.4).

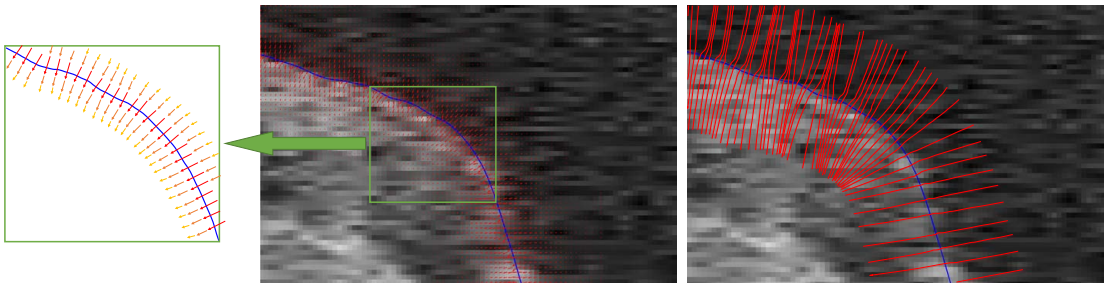

(a) (b)

Figure 7.4: (a) A zoomed-in illustration of gradient vectors, for better illustration of the gradient vectors, a schematic image is provided where the larger and reddish vectors represents stronger gradient vectors. (b) The columns constructed by following the flow of the gradient vectors. The blue line shows the corrected initial segmentation.

7.1.4 Graph Construction and Cost Function Computation

The radial OCT volume is resampled using the GVF-based columns computed in section 7.1.3. When the OCT volume is transferred from the radial domain to the new space, the neighborhood relationships are retained (i.e., the 8-neighboring columns of a specific column in the radial volume and the resampled volume stay the same). Due to the fact that the GVF-based columns are along the normals at the initialization surface, and the columns are extended to the same length in both sides of the initial segmentation, it is expected that the ILM surface in the resampled volume appears as a smooth surface with minimal variation in the middle of the cube. We incorporate this prior shape information in the graph construction which helps with managing the presence of blood vessels.

Our graph-theoretic approach follows the methods proposed in [44,76]. Consider a volumetric image in the resampled volume described as $\mathcal{I}(i,j,k)$ with dimensions $I \times J \times K$, and the ILM surface $\mathcal{S}$ can be defined as a function $\mathcal{S}(i,j)$ that maps each (i,j) pair to its corresponding k value. The surface $\mathcal{S}$ has to intersect with one and only one voxel on each GVF-based column in the resampled domain, parallel to the k–axis and

spans the entire $i \times j$ domain. In order to assure obtaining a smooth segmentation, the surface smoothness constraints in both i and j directions are enforced. The *hard* surface smoothness constraint represents the maximum allowed variation of $\mathcal{S}$ between two adjacent columns in i–direction, Δ_i, and in j–direction, Δ_j. In other words, if $\mathcal{I}(i,j,k_1)$ and $\mathcal{I}(i+1,j,k_2)$ are two adjacent voxels on the surface $\mathcal{S}$ in the i–direction ($k_1 = \mathcal{S}(i,j)$ and $k_2 = \mathcal{S}(i,j+1)$), then $\left|\mathcal{S}(i,j) - \mathcal{S}(i+1,j)\right| \leq \Delta_i$. Similarly, for two adjacent voxel on the surface $\mathcal{S}$ in the j–direction ($\mathcal{I}(i,j,k_1)$ and $\mathcal{I}(i,j+1,k_2)$) we have $\left|\mathcal{S}(i,j) - \mathcal{S}(i,j+1)\right| \leq \Delta_j$.

In order to incorporate the shape prior information, in addition to hard smoothness constraints, *soft* smoothness constraints, responsible for penalizing the deviation from the expected shape inside the allowed variations (hard smoothness constraints) is also enforced [76]. Therefore, the deviation of the surface $\mathcal{S}$ from its expected shape is penalized via a convex function $f(h)$. Specifically, for any pair of neighboring columns $p = (i_1, j_1)$ and $q = (i_2, j_2)$ on surface $\mathcal{S}(i,j)$, if the expected shape change of surface $\mathcal{S}$ between (p,q) is $m_{(i_1,j_1),(i_2,j_2)}$ the cost of the shape term can be written as:

$$C_{shape} = \sum_{\{(i_1,j_1),(i_2,j_2)\in\mathcal{N}_c\}} f(\mathcal{S}(i_1,j_1) - \mathcal{S}(i_2,j_2) - m_{(i_1,j_1),(i_2,j_2)}). \tag{7.5}$$

Here, $\mathcal{N}_c$ indicates the neighboring relationships. Due to the resampling of the volume along the normals of the initial segmentation, it is expected that the ILM surface appears as a smooth surface with minimal variation in the resampled volume, hence, $m_{(i_1,j_1),(i_2,j_2)} = 0$. Since the weights of those graph arcs that are responsible for enforcing the soft smoothness constraints are related to the second derivatives of the penalizing function f [76], and the arc weights need to be greater than or equal to zero, the penalizing function is required to be convex for which a quadratic function is employed in Eq. 7.5.

As part of the total cost function of the ILM surface, C_{total}, an edge-based cost function called the *on-surface* cost function is employed [44]. The on-surface cost function reflects the unlikelihood of a voxel being located on the ILM surface (i.e., it has lower values for the voxels located on the ILM surface). The strategy to deal with the blood vessels is relying more on the contextual information from adjacent slices, the shape prior knowledge, and the feasibility constraints than on the on-surface cost function values. Hence, the on-surface cost function at the blood vessel locations is modified to enable the graph-theoretic approach to cut through the blood vessels that change the shape of the ILM surface substantially. The blood vessel location is obtained by transferring the binary vessel map computed from the registered fundus photographs to the radial domain. The on-surface cost function can be expressed as:

$$C_{on-surface} = \sum_{\{(i,j,k)|k=\mathcal{S}(i,j)\}} w(i,j)\acute{\mathcal{E}}(i,j,k) \quad , \quad w(i,j) = \begin{cases} 1/3 & , \quad M_{vessel}(i,j) = 1 \\ 1 & , \quad M_{vessel}(i,j) = 0 \end{cases} \tag{7.6}$$

where $w(i,j)$ controls the modification of the cost function at the blood vessel locations and M_{vessel} is the binary vessel map in the radial domain. The edge information, $\acute{\mathcal{E}}(i,j,k)$, is computed by resampling the inverted response of the 3D Gaussian derivative filter ($\mathcal{E}(r,\theta,z)$ computed in section 7.1.2) using the GVF-based columns. The intensities of $\mathcal{E}(r,\theta,z)$ were normalized and inverted before resampling, to reflect the unlikelihood of a voxel being located on the ILM surface. Therefore, the total cost of finding the ILM surface in the resampled volume can be written as follows:

$$C_{total} = C_{on-surface} + \alpha C_{shape} \; . \tag{7.7}$$

Here, the coefficient α was set to 0.85. As in [76], the optimal ILM surface can be found by computing the max–flow/min–cut in the arc-weighted graph. Once the ILM

surface is obtained in the resampled volume, the segmentation is transferred back to the radial domain.

7.2 Experimental Methods

7.2.1 Data and Reference Standard

The dataset in this work includes optic nerve head (ONH)-centered SD-OCT volumes in one eye (per patient) of 44 open-angle glaucoma or glaucoma suspect patients acquired using a Cirrus HD-OCT device (Carl Zeiss Meditec, Inc., Dublin, CA) at the University of Iowa. The size of each scan was 200×200×1024 voxels (in the x-y-z direction, respectively) which corresponds to a voxel size of 30×30×2 μm, and the voxel depth was 8 bits in grayscale. Additionally, the color fundus photograph of the optic disc corresponding to each SD-OCT scan was taken as well. Twenty-four patients had stereo color fundus photographs taken using a stereo-base Nidek 3-Dx stereo retinal camera (3072×2048 pixels). The rest of the patients had color fundus photographs taken using a Topcon 50-DX camera (2392×2048 pixels). The pixel depth was 3 8-bit red, green and blue channels.

The reference standard was obtained by randomly selecting two radial slices from each SD-OCT volume and performing the manual delineation of the ILM surface by an expert.

7.2.2 Experiments

The performances of the following three methods were compared: 1) the initialization computed using a multiresolution process in section 7.1.2, 2) the ILM segmentation proposed by Lee *et al.* [16], and 3) the proposed graph-theoretic approach in this paper. The metrics used to evaluate the accuracy of the segmentation results consisted of the signed and unsigned border positioning errors calculated in the radial domain. The unsigned border positioning error was calculated by averaging the distances between all surface points (on two randomly selected slices) from the reference

standard and the corresponding closest points from the segmentation result. The signed border positioning error was similarly calculated but the signs of the distances were retained. If the algorithm's surface point was above the surface point of the reference standard, the sign was considered positive.

Additionally, in order to further asses the effectiveness of the proposed method in dealing with the presence of the retinal blood vessels and the steep slopes, the signed and unsigned border positioning errors were measured locally as well. Hence, for measuring the localized error at the blood vessel locations, only the A-scans intersecting with blood vessels were considered for measuring the border positioning errors. Similarly, the localized error of steep slope is computed at the A-scans containing steep slopes which were identified by computing the gradient of the ground truth. A paired t-test was utilized to compare the performances of three methods where $p < 0.05$ was considered significant.

Furthermore, the accuracy of the three segmentation approaches were evaluated using the cup volume. In order to compute the cup volume, the reference plane at each B-scan is defined as a straight line 150 μm (standard cup offset) above the straight line that connects the two BMO points [133] and the volume bounded between the ILM surface and the BMO reference plane was considered as the cup volume. The average of the cup volumes on the two B-scans with the manual segmentation was calculated for each subject.

The second structural parameter that is influenced by the ILM segmentation is BMO-MRW. Hence, we investigate the extent that accounting for the presence of blood vessels and steep slope in segmenting ILM surface affects the rim-width-based parameter. To this end, the structure-structure Pearson correlation of RNFL_{L} and $\text{BMO-MRW}_{\text{L}}$ computed using the ILM segmentation in [16] and the Pearson correlation RNFL_{P} and $\text{BMO-MRW}_{\text{P}}$ computed using the ILM segmentation proposed in this chapter were compared with each other using the method mentioned in Chap-

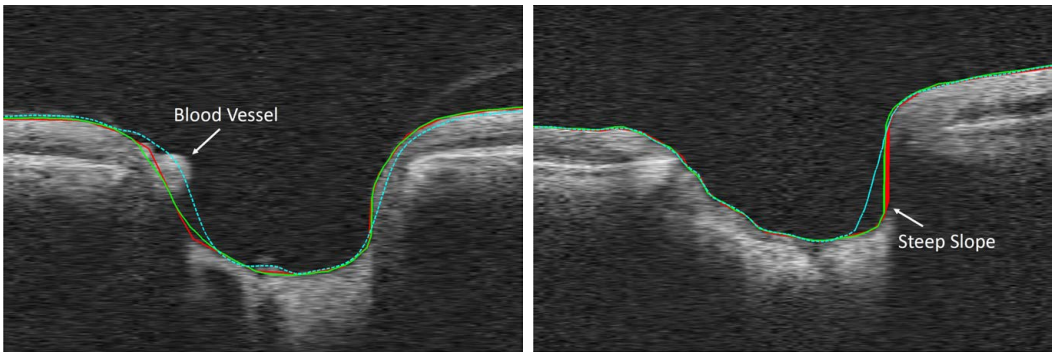

(a) (b)

Figure 7.5: Example results on the ONH portion of two slices from two volumes (only the ONH portion shown for better visibility). Red is the reference standard, green is the proposed algorithm and dashed cyan is Lee *et al.* [16] results. (a) Shows the effect of the presence of blood vessels and (b) shows an example of deep cupping.

ter 5 [112]. BMO-MRW measures were computed on the 20 evenly spaced randomly selected radial scans where the BMO points were identified by consensus manual delineations from three experts (the same manual delineations that were used in Chapter 5).

7.3 Results

Two examples ILM surface segmentation are shown on a single radial B-scan in Fig. 7.5. The quantitative evaluations of border positioning errors for the entire ILM surface are provided in Table 7.1. The proposed method had significantly smaller signed and unsigned border positioning errors than the initialization and Lee *et al.* segmentations (p-value < 0.05). In addition, the proposed method improved the average unsigned border positioning error of Lee *et al.* method and the initialization by 47.95% and 68.09%, respectively.

Furthermore, the localized border positioning errors at the blood vessel locations and steep slopes are reported in Table 7.2. The signed and unsigned border positioning errors (at the blood vessel locations) of the proposed method were significantly

Table 7.1: Average signed and unsigned border positioning error (Mean ± SD in μm).

Methods	Unsigned	Signed
Initialization	20.12 ± 10.36	7.23 ± 4.38
Lee *et al.* [16]	13.68 ± 7.12	5.21 ± 3.45
Proposed	**7.05 ± 3.43**	**-2.07 ± 1.62**

Table 7.2: Localized unsigned and signed border positioning error at blood vessel and steep slope locations (Mean ± SD in μm).

	Blood Vessel		Steep Slope	
Error	Unsigned	Signed	Unsigned	Signed
Initialization	18.23±12.41	12.98±15.91	26.49±17.22	25.89±22.58
Lee *et al.* [16]	11.58± 9.06	10.28±12.58	16.65±10.37	16.13±13.72
Proposed	**4.03± 2.28**	**1.88± 3.14**	**5.18± 3.65**	**4.88± 4.67**

lower than the initialization and and Lee *et al.* segmentations (p-value < 0.05). The proposed method improved the average unsigned border positioning error (at the blood vessel locations) of Lee *et al.* method and the initialization by 65.20% and 77.89%, respectively.

Similarly, the proposed method had significantly lower signed and unsigned border positioning errors (at the steep slopes) than the initialization and Lee *et al.* segmentations (p-value < 0.05). The proposed method improved the average unsigned border positioning error (at the steep slopes) of Lee *et al.* method and the initialization by 68.89% and 80.45%, respectively.

The cup volume measurements are reported in Table 7.3. Furthermore, the Bland-Altman graphs in the Fig. 7.6 clearly shows that initialization and the method in [16] underestimate the cup volume which resulted in the negative biases, whereas, the proposed method decreased the existing bias in the other approaches substantially. Additionally, the cup volume calculated using the manual segmentation and the auto-

Table 7.3: Cup volume measurements.

	Mean± SD in mm^2	Pearson Correlation
Initialization	1.756±0.441	98.66
Lee *et al.* [16]	1.836±0.457	99.02
Proposed	**1.900±0.475**	99.94
Reference standard	1.905±0.477	–

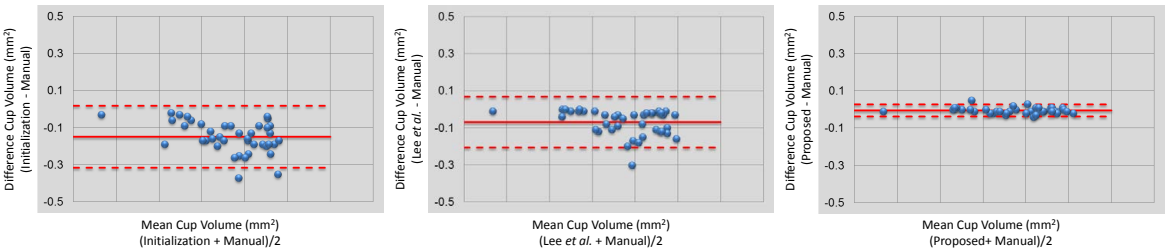

(a) (b) (c)

Figure 7.6: The Bland-Altman graphs of the cup volume measurement corresponding to (a) initialization, (b) Lee *et al.* [16], and (c) the proposed method in comparison with the manual tracing.

mated approaches were compared using paired t-tests and the results showed that the cup volume computed using the initialization and the method in [16] are significantly different from that of the manual segmentation ($p < 0.05$). However, the cup volume computed using the proposed method was not significantly different from that of the manual segmentation ($0.05 < p$).

The Pearson correlation of the BMO-MRW$_{\mathrm{L}}$ and BMO-MRW$_{\mathrm{P}}$ was 98.84 and the

Table 7.4: BMO-MRW computation and correlation with RNFLT.

	Mean± SD in μm	Correlation with RNFLT
BMO-MRW$_{\mathrm{L}}$	181.11±84.25	71.16
BMO-MRW$_{\mathrm{P}}$	179.57±80.45	72.42

paired t-test did not show any significant difference between two measures ($0.05 < p$). Additionally, the test for comparing two overlapping correlations based on two dependent groups did not show significant difference between the Pearson correlations of the BMO-MRW computations with their corresponding RNFLT measures.

7.4 Discussion and Conclusion

In this chapter, we proposed a multimodal graph-theoretic approach for segmenting the internal limiting membrane surface from optic-nerve-head-centered SD-OCT volumes and the proposed method was tested on 44 glaucoma patients. The existing ILM segmentation approaches (e.g. the method in [16]) generate erroneous results inside the optic nerve head region due to the presence of retinal blood vessels and existing deep cupping and steep slopes in the ILM surface which are very typical in glaucomatous SD-OCT scans. These issues cause inaccurate measurements of ONH structural parameters such as Bruch's membrane opening-minimum rim width and cup volume. The proposed method deals with the issue of large blood vessels by modifying the cost function associated with the graph-theoretic approach and eliminates the steep slopes by resampling the OCT volumes using the gradient vector flow-based columns.

The large retinal blood vessels locating near the ILM surface, which are characteristics of ONH region, are able to change the morphology of the ILM surface. Current segmentation approaches include the blood vessels as part of the ILM surface which increase the possibility of inaccurate measurement of the structural parameters such as BMO-MRW. The correct way of dealing with retinal blood vessels is controversial [6], however, we currently argue that doing a better job of only including the non-vascular tissue can provide the most precise measurements of glaucoma parameters of interest such as BMO-MRW, where going around the vessels would lead to overestimating the MRW. Note that as BMO-MRW is measured as the shortest Euclidean distance from the BMO to the ILM surface, depending on the location of

blood vessels, and the closest point on the ILM surface to BMO, the BMO-MRW parameter may or may not be affected by the presence of blood vessel. Hence, it is possible that BMO-MRW computed using the proposed ILM segmentation stays the same as that of computed using the existing ILM segmentation approaches.

The proposed method also addresses the issue of segmenting ILM surface inside deep cups with steep slopes. In order to be able to accurately segment the ILM surface, the segmentation must be able to intersect with A-scans containing steep slopes more than once, therefore, those segmentation approaches [16, 44] that were initially designed to segment the intraretinal layers of the macula or the peripapillary region surrounding the ONH cannot catch the steep slopes inside the deeper cups. This issue results in inaccurate cup volume measurements [133], and the Bland-Altman graphs in Fig. 7.6 shows the negative bias of the method in [16] which is associated with the underestimating cup volumes. Resampling the volume using GVF-based columns which are along the normals of initial segmentation helps eliminate the steep slopes and transfers the ILM surface into a smooth surface with minimal variation. Therefore, the graph-theoretic approach incorporates this shape prior knowledge while segmenting the ILM surface in the resampled volume. The Bland-Altman graphs in Fig. 7.6 demonstrate that the proposed method successfully removed the negative bias existed in the initialization and Lee *et al.*'s method.

The results of BMO-MRW computations with and without ILM segmentation correction showed that the effects of proposed method for segmenting the ILM surface on computing the BMO-MRW was not significant. The reason is that first of all, the presence of blood vessels or steep slopes do not always intervene the computation of BMO-MRW, hence in those slices the BMO-MRW with and without ILM correction are the same. Secondly, the location of closet point on the ILM surface to the BMO point (from where the BMO-MRW is computed) does not always modified by the correction. Lastly, even if the ILM correction modifies the location of closet point on

the ILM surface to the BMO point, the distance between the BMO-MRW parameter as a distance measure could still remain the same or change slightly. Even though our results did not show significant difference between BMO-MRW_L and BMO-MRW_P, computing the BMO-MRW from a more accurate ILM segmentation results in a more precise estimation of remaining neuroretinal rim tissue.

While Lang *et al.* [134] demonstrated that reformatting the OCT volume is beneficial for intraretinal layer segmentation in macular scans and GVF-based columns have been previously used in the graph-construction for segmenting complex-topology surfaces of the brain [135], we present a new framework for precise segmentation of the ILM surface by reformatting the OCT volumes using non-overlapping GVF-based columns. Additionally, use of multimodal information for the graph-construction and cost function design for use in the 3D graph-based approach that incorporates shape priors [76] is generally novel as well. In addition to allowing for a more precise ILM segmentation for ophthalmic applications, as in this work, it is expected that other application domains would also benefit from a multimodal graph-construction and cost-function design framework.

In summary, we proposed a method for accurate segmentation of the ILM surface within ONH region of OCT volumes where first, the blood vessels are segmented from the registered fundus photographs due to the higher visibility of ONH region in fundus photographs than OCT projection images. The vessel mask is transferred to the radial domain along with the OCT volumes and is utilized for two purposes 1) correcting the initial segmentation which is computed using a multiscale peak detection method and 2) modifying the cost function used in the graph-theoretic approach at the vessel locations. The radial volumes are resampled using non-overlapping GVF-based columns which are calculated by following the directions of gradient vector flow field of the initial segmentation. The optimal solution with respect to the edge-based and shape-based cost functions is obtained using a graph-theoretic approach in the

resampled domain and finally the segmentation is transferred back to the original domain.

CHAPTER 8
A MACHINE-LEARNING GRAPH-BASED APPROACH FOR 3D SEGMENTATION OF BRUCH'S MEMBRANE OPENING FROM GLAUCOMATOUS SD-OCT VOLUMES

The content of this chapter is presented in [136]. As mentioned in Chapter 5, Bruch's membrane opening-minimum rim width (BMO-MRW) measures the remaining neuroretinal rim tissue and recent studies showed that BMO-MRW is superior to other structural parameters for diagnosing open-angle glaucoma [19, 20]. Beside the necessity of identifying BMO points for computing the BMO-MRW, the BM surface ending points also define the true optic disc boundary. The 3D imaging ability of SD-OCT machines showed that the disc margin (DM) from fundus photographs does not always coincide with the outer border of rim tissue, however, BMO, also referred to as the neural canal opening (NCO), is the true outer border of rim tissue (optic disc boundary) which remains unaltered during intraocular pressure changes due to glaucoma [19–21]. Hence, considering the inherent subjectivity and required time for manual delineations, in order to be able to identify the true optic disc boundary and compute the structural parameter BMO-MRW automatically, having a reliable automated approach for segmentation of BMO points is of great desire.

Various approaches have been employed for segmenting the optic disc from SD-OCT volumes including pixel-based classification methods [16, 17, 88], model-based approaches [23], and graph-based approaches [18, 22], among which some techniques are also utilized for segmenting the optic disc from fundus photographs [7–15]. The approaches that attempted to segment the BMO from SD-OCT volumes mostly focused on 2D segmentation of BMO points. For instance, the works in [18] and our method in Chapter 4 focused on segmenting the 2D projection of BMO points, while Fu *et al.* found the BMO points from a number of individual 2D B-scans and fitted an ellipse to the points to obtain the complete ring-shape BMO segmentation [23].

Our proposed method in [24] was the first step towards directly obtaining a 3D

segmentation, where we presented an automated iterative graph-theoretic approach for segmenting multiple surfaces with a shared hole. The method was applied to segment the junction of the inner and outer segments (IS/OS) of the photoreceptors and the Bruch's membrane (BM) surfaces and their shared hole (i.e. BM opening). This method needs an initial 2D segmentation of BMO points, which is obtained from a 2D projection image, using a method similar to the existing 2D approaches [18, 22]. The corresponding z-values are identified by projecting the 2D segmentations onto the BM surface. Since the layer segmentation around the ONH region is not precise, the computed z-values are not always accurate. In order to allow for correcting the z-values, an iteration phase was added to the method within which the z-values along with new layer segmentations are identified as part of the proposed surface+hole method. The updated layers produces a new 2D projection image from which an updated 2D BMO segmentation is obtained and the iterations continue. This surface + hole approach was shown to be more accurate than existing 2D approaches; however, the presence of externally oblique border tissue [19], which attaches to the end of BM surface and appears very similar to the ending point of BM surface sometimes confuses the algorithm and causes continuing of its iterative search on the border tissue such that instead of the end of the BM surface, the BMO is identified on the border tissue.

Correspondingly, the purpose of this chapter is to address the limitation of our previous approach by eliminating the iteration phase and presenting an automated machine-learning graph-theoretic approach that segments the BMO points as a 3D ring in radially resampled SD-OCT volumes. More specifically, similar to our previous approach, a 2D initial segmentation is obtained using a graph-theoretic approach. The volume in the z-direction is downsampled to achieve an isotopic grid and an estimated 3D location of BMO points is computed by projecting the (r, θ) pairs onto the BM surface. Instead of defining a mathematical model for BMO points, which is not feasible as they appear differently even in slices corresponding to a

single subject, we learn the intensity-based attributes of BMO points a priori. In particular, based on a random-forest classifier trained using BMO intensity models, a likelihood map corresponding to the *BMOness* of voxels located in a small vicinity of each estimated 3D locations is generated. The inverted likelihood map will serve as the cost function for finding the 3D BMO path using a shortest-path approach. The final BMO segmentation in the original image resolution is obtained by refining the z-coordinates using a similar approach as used to find the BMO path within the downsampled volume.

8.1 Methods

The overall flowchart of the proposed method is shown in Fig. 8.1. The four major components of the proposed method are: 1) a preprocessing step including transferring the SD-OCT volumes to the radial domain and segmenting intraretinal surfaces (Section 8.1.1), 2) identifying the 2D projected locations of the BMO points using a graph-theoretic approach (Section 8.1.2), 3) computing a cost function for identifying the BMO 3D path using a machine-learning approach (Section 8.1.3), and 4) identifying the 3D location of BMO points (as a 3D path within the SD-OCT volumes) using a shortest path method (Section 8.1.4) and refining the path in the z-direction (Section 8.1.5).

8.1.1 Preprocessing

In the preprocessing step, the SD-OCT volume is transfered to the radial domain and the intraretinal surfaces that are needed for identifying the BMO points are segmented as in Chapter 4. If the original SD-OCT volume in the Cartesian domain is represented by $I(x, y, z)$, the radial volume $I_R(r, \theta, z)$ is obtained using bilinear interpolation of the original volume with angular precision of 1° degree. The radial transformation is performed because the BMO points are more obvious in the radial volume than in the original SD-OCT volume where BMO points are less obvious in

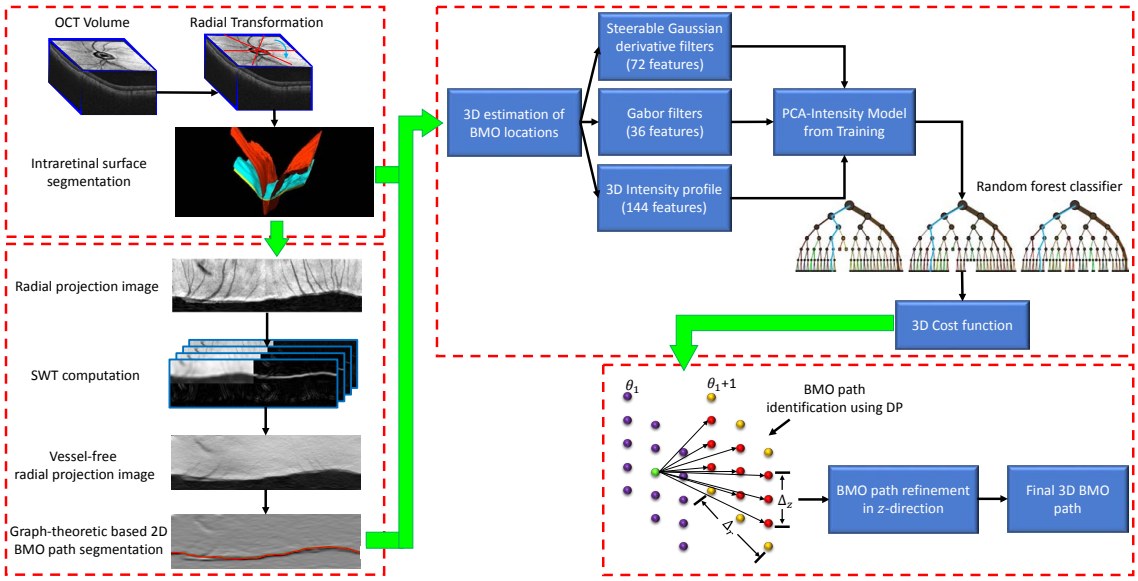

Figure 8.1: Flowchart of overall method.

the slices close to the upper/lower part of disc boundary and are not present in the slices that do not intersect with optic disc (Fig. 5.4). With such a transformation, there are two BMO points in each radial slice and unlike the original domain, Bruch's membrane opening has a stiffer shape especially in the r-direction (i.e. displacement of the BMO points in-between slices in the r-direction is minimal). This property will be used later as a constraint for the graph-theoretic approach in Sections 8.1.2.3 and 8.1.4.

Once the radial volume is created, intraretinal surfaces are segmented from the radial volume using a theoretical multi-resolution graph-based approach [16,44]. Specifically, the intraretinal surface segmentation problem is transformed to an optimization problem with a number of specific constraints and the goal is finding a set of feasible surfaces with the minimum cost, simultaneously [44]. Lee *et al.* [16] proposed a multi-resolution approach for executing the algorithm which speeds up the segmentation. We employed this method for segmenting three intraretinal surfaces from the radial volumes: the first surface is called the internal limiting membrane (ILM), surface two

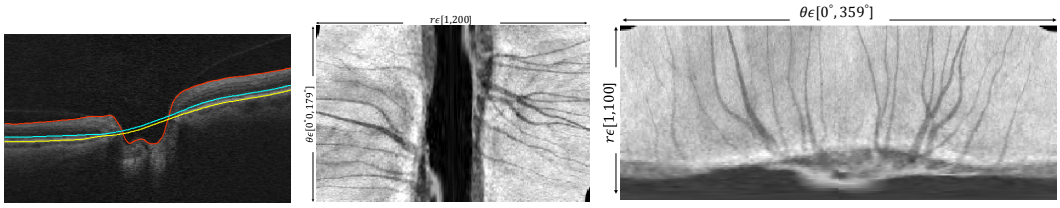

(a) (b) (c)

Figure 8.2: Radial surface segmentation and projection image creation. (a) Example radial scan with segmented surfaces where red, green, and yellow are the ILM, IS/OS, and BM surfaces, respectively. Note that the IS/OS and BM surfaces are interpolated inside the ONH. (b) The projection image obtained as described in Section 6.1.1. (c) The reformatted radial projection image in which the 2D BMO projection locations appear as a horizontal path.

is located at the junction of the inner and outer segments of photoreceptors (IS/OS), and surface three, called Bruch's membrane (BM) surface, is the outer boundary of the retinal pigment epithelium (RPE). These surfaces are segmented because (1) the ILM surface will be used as a constraint for finding the 2D and the 3D BMO path as well as computing BMO-MRW, (2) IS/OS and BM surfaces will be used for creating the radial projection image, and (3) the BM surface also will be used for identifying the estimated 3D location of the BMO points. Since the RPE-complex, bounded by IS/OS and BM surfaces, does not exist inside the ONH, the surface segmentations corresponding to the second and third surfaces are not meaningful inside the opening. Hence, the second and the third surfaces are interpolated inside the ONH opening which is approximated by a circle larger than the typical size of the ONH opening (1.73 mm radius) and centered at the center of the ONH [22]. The lowest point of the ILM surface is considered as the approximated center of the ONH (Fig. 8.2a).

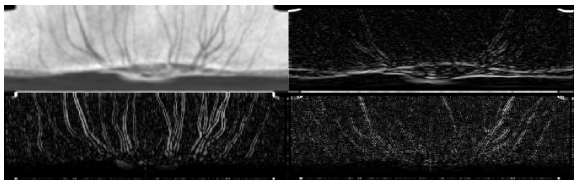

(a)

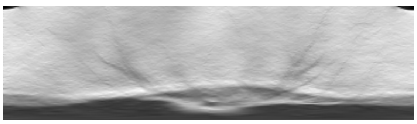

(b)

(c)

Figure 8.3: An example of edge-based cost function computation. (a) The 2$^{\text{nd}}$ scale of SWT decomposition. Note that BMO boundary appears in the horizontal coefficients while the blood vessels mostly appear in vertical and diagonal coefficients. (b) The vessel-free radial projection image. (c) The edge-based cost function computed by applying the Gaussian derivative filter, $\mathcal{F}_{\sigma_r,\sigma_\theta}(r,\theta)$, to the vessel-free radial projection image.

8.1.2 Identifying 2D Projected Location of BMO Endpoints

The projected locations of BMO points are identified from the radial projection image in the form of a 2D path utilizing a graph-theoretic approach and an edge-based cost function computed from the radial projection image. The approach is similar to our method in Chapter 4, except that here, the total cost function does not include the *in-region* cost term and shape prior information is also enforced.

8.1.2.1 Computing the Radial Projection Image

The radial projection image is created by averaging the intensities of the RPE-complex (the sub-volume between the blue and yellow surfaces in Fig. 8.2a) in the z-direction (Fig. 8.2b). In particular, the intensities of the sub-volume bounded by 15 voxels (29.3 μm) above the second surface and 15 voxels below the third surface are averaged in the z-direction and the resulting projection image is reformatted such that radial and θ values appear on vertical and horizontal axes, respectively and the BMO projection path appears as an approximately horizontal boundary (Fig. 8.2c).

8.1.2.2 *Computing the Edge-Based Cost Function*

An edge-based cost function is designed to have information regarding the location of the boundary of interest in the image (here, the 2D BMO trajectory). More specifically, the edge-based cost function is a probability map that contains the unlikelihood of pixels locating on the boundary. Therefore, we would like to have a cost function with low values on the expected location of the boundary and high values everywhere else.

The BMO boundary and the retinal blood vessels are the two major structures of the reformatted radial projection images. With the help of the Haar stationary wavelet transform (SWT) [101], we eliminate the effect of retinal blood vessel in computing the edge-based cost function. Similar to Chapter 4, we compute the vessel-free radial projection image (Fig. 8.3b). In order to compute the edge-based cost function, an asymmetric 2D Gaussian derivative filter $\mathcal{F}_{\sigma_r,\sigma_\theta}(r,\theta)$ is applied to the vessel-free projection image $I_{vf}(r,\theta)$ with the aim of capturing the dark-to-bright transitions. The filter has larger scale in the θ-direction ($\sigma = 4$) than the r-direction ($\sigma = 2$) and computes the derivatives only in the r-direction (vertical axis). If a general 2D Gaussian filter in the radial domain can be written as:

$$\mathcal{G}_{\sigma_r,\sigma_\theta}(r,\theta) = \frac{1}{2\pi\sigma_r\sigma_\theta}\, e^{-\left[(\frac{r}{\sqrt{2}\sigma_r})^2+(\frac{\theta}{\sqrt{2}\sigma_\theta})^2\right]}, \tag{8.1}$$

the asymmetric Gaussian derivative filter applied to the vessel-free image can be expressed as $\mathcal{F}_{\sigma_r,\sigma_\theta}(r,\theta) = \partial\mathcal{G}_{\sigma_r,\sigma_\theta}/\partial r$, where σ_r and σ_θ are the standard deviations in the r and θ directions, respectively. The edge-based cost function is shown in Fig. 8.3c. Therefore, the total edge-cost representing the cost of pixels on a 2D BMO path, $\mathcal{B}(\theta)$, can be expressed as

$$C_{edge} = \sum_{\{(r,\theta)|r=\mathcal{B}(\theta)\}} \mathcal{F}_{\sigma_r,\sigma_\theta}(r,\theta) * I_{vf}(r,\theta) \tag{8.2}$$

and the goal is to select $\mathcal{B}(\theta)$ that minimize the cost function C_{edge}.

8.1.2.3 Segmenting BMO 2D Path

In order to identify the minimum-cost 2D BMO path, a graph-theoretic approach proposed by Song *et al.* [76] is utilized. This approach, is an extension to the method proposed by Garvin *et al.* [44] that enables us to constrain the geometry of the boundary of interest based on prior shape information of the boundary. For instance, as mentioned in Section 6.1.1, it is known that in the radial projection image, the BMO boundary is very smooth across slices with minimal changes in the r-direction. This shape-prior knowledge was enforced as a *soft* smoothness constraint along with the *hard* smoothness constraints [76].

More specifically, consider a 2D image $I(r,\theta)$ of size $R\times\Theta$ in the radial domain and the 2D BMO boundary $\mathcal{B}(\theta)$ as a function of θ that maps each θ-value to its corresponding r-value. In addition, assume that the function intersects with each column (each θ) once (at r) and the function uses a two-neighbor relationship. Two types of constraints are applied to the neighboring columns, the *hard* smoothness constraint and the shape-prior (*soft* smoothness) constraints. The *hard* smoothness constraint for a pair of neighboring columns (θ_1,θ_2) in the θ-direction can be written as below

$$-\Delta_r \leq \mathcal{B}(\theta_1) - \mathcal{B}(\theta_2) \leq \Delta_r \quad , \tag{8.3}$$

where Δ_r is the maximum allowed change of r between two neighboring columns. In order to incorporate the shape prior information, in addition to hard smoothness constraints, the deviation from the expected shape inside the allowed constraint is penalized as well [76]. A convex function $f(h)$ penalizes the cost of the boundary if

the change of the boundary is deviated from its expected shape. Specifically, for any pair of neighboring columns (identified by N_c) such as (θ_1, θ_2) on boundary $\mathcal{B}$, if the expected shape change of boundary $\mathcal{B}$ between (θ_1, θ_2) is $m_{(\theta_1,\theta_2)}$ the cost of the shape term can be written as:

$$C_{shape} = \sum_{\{(\theta_1,\theta_2)\in\mathcal{N}_c\}} f(\mathcal{B}(\theta_1) - \mathcal{B}(\theta_2) - m_{(\theta_1,\theta_2)}). \tag{8.4}$$

Here, $m_{(\theta_1,\theta_2)} = 0$ as we expect to have very smooth BMO boundary with minimal change between neighboring columns. The penalizing function f needs to be a convex function for which a quadratic function is chosen. The total cost of finding the initial 2D BMO boundary $\mathcal{B}$ consists of both edge-based and shape prior cost functions which can be expressed as follows:

$$C_{\mathcal{B}} = C_{edge} + \alpha C_{shape} \ . \tag{8.5}$$

The coefficient α determines the impact of shape prior cost function with respect to the edge-based cost function. Using a training set, the parameter α was set to 0.7 in this study. The optimal boundary can be found by computing the maxflow/min-cut in the arc-weighted graph as in [76]. At this step, the 2D BMO locations were identified using which the location of 3D BMO points were estimated by projecting the 2D locations onto the BM surface.

8.1.3 Computing Machine-Learning-Based 3D Cost Function

In order to compute the 3D cost function for more precisely identifying the 3D BMO locations, a machine-learning based approach is utilized. First, to obtain an isotropic grid, the radial OCT volume is downsampled in the z-direction to reflect its physical resolution such that the size of each pixel in the r-z plane changes from $30\mu\text{m} \times 2\mu\text{m}$ to $30\mu\text{m} \times 30\mu\text{m}$. For each subject in the training set, a set of intensity-

based features are extracted from each BMO location. An intensity model of BMO (called BMO_L to represent the low-resolution BMO model) is created from the extracted features using PCA technique. In order to train a random forest [99] classifier, the same set of intensity-based features are extracted from BMO points (positive) as well as non-BMO points (negative) and projected to the BMO_L model. The classifier computes the "BMOness" of each point in the vicinity of estimated 3D BMO locations (explained in section 8.1.3.2) for subjects in the test set. The inverted BMOness probability map will serve as the 3D cost function of the shortest path method for identifying the 3D BMO locations (Section 8.1.4).

8.1.3.1 Computing 3D PCA-Intensity BMO Model

In order to compute the 3D intensity model of BMO, three types of intensity features are computed at each BMO point: 1) neighborhood intensity profile (NIP), 2) steerable Gaussian derivatives (SGD), and 3) Gabor features. Since the radial OCT volumes are created by sampling the original OCT volume in a circular pattern (Fig. 5.4), the first and last slices are considered as neighbors during feature extraction. The BMO_L intensity model consists of a number of PCA-based models created from each feature category. Before feature extraction, the intensities of the radial OCT volume are linearly normalized to the $[0, 255]$ interval such that the intensity scale throughout the dataset is consistent.

The NIP feature provides information regarding the 3D intensity profile of the query point's neighborhood. NIP features are computed using a mask of size $9 \times 9 \times 3$ within which 48 neighbors around the query point in each of current, previous, and next slices are marked (a total of 144 features). The 48 neighbors are inspired by the positions of offsets used in the FAST-ER corner detector [137]. The difference of the query point's intensity and the intensities of its 144 neighbors are computed to learn the 3D intensity profile around a BMO point.

A set of 3D steerable Gaussian derivative filters with $\sigma = \{0.5 : 0.5 : 3\}$ and

$\phi = \{0° : 30° : 359°\}$ are used to reflect the intensity change around a BMO point (a total of 72 features). Assume $\mathcal{G}_\sigma^\phi(r, z, \theta)$ is a symmetric 3D Gaussian filter and $(\cdots)^\phi$ represents the rotation operator in the r-z plane such that $\mathcal{F}_\sigma^{\phi_0^\circ}(r, z, \theta)$ is the rotated version of $\mathcal{F}_\sigma(r, z, \theta)$ at angle ϕ_0° in the r-z plane. Thus, the 3D steerable Gaussian derivative filter, $\mathcal{F}_\sigma^\phi(r, z, \theta)$, can be expressed as follows:

$$\begin{aligned}
\mathcal{F}_\sigma^{0^\circ}(r, z, \theta) &= \frac{\partial}{\partial r}\mathcal{G}_\sigma(r, z, \theta) \ , \\
\mathcal{F}_\sigma^{90^\circ}(r, z, \theta) &= \frac{\partial}{\partial z}\mathcal{G}_\sigma(r, z, \theta) \ , \\
\mathcal{F}_\sigma^{\phi}(r, z, \theta) &= \cos(\phi)\mathcal{F}_\sigma^{0^\circ}(r, z, \theta) + \sin(\phi)\mathcal{F}_\sigma^{90^\circ}(r, z, \theta) \ .
\end{aligned} \tag{8.6}$$

As depicted in Eq. 8.6, the derivative is taken only in the r-z plane, however, in order to incorporate the 3D contextual information, the SGD filters are designed in 3D to integrate information from neighboring slices as well.

A set of Gabor filters [138] extract localized frequency information (i.e. textural information) from the region of interest. The Gabor filters are represented as:

$$\begin{aligned}
\mathcal{GB}_{\sigma,\gamma,\lambda,\phi,\psi}(r, z) &= e^{-\frac{r'^2+\gamma^2 z'^2}{2\sigma^2}} e^{i\left(2\pi\frac{r'}{\lambda}+\psi\right)} \ , \\
r' &= r\cos\phi + z\sin\phi \ , \ z' = -r\sin\phi + z\cos\phi \ .
\end{aligned} \tag{8.7}$$

where σ, γ, λ, ϕ, and ψ are the scale, spatial aspect ratio, wavelength, orientation, and the phase offset, respectively. Since the Gabor filters are symmetric, the filter bank includes 6 scales and 6 orientations of $\sigma = \{0.5 : 0.5 : 3\}$ and $\phi = \{0°, 30° : 179°\}$. The wavelength ($\lambda$) was set to $\sigma/0.56$ as this corresponds to a half-response spatial frequency bandwidth of one octave. The spatial aspect ratio and the phase offset were set to $\gamma = 1$ and $\psi = 0°$, respectively.

Once the intensity features are extracted from the BMO points, in order to reduce the dimensionality of the feature set (144 NIP, 72 SGD, and 36 Gabor features), PCA was utilized to create 13 PCA-based intensity models by retaining more than 90% of

the variation in each category. The PCA-based intensity models consisted of 1 NIP model, 6 SGD models corresponding to the 6 different scales used for creating SGD filters, and 6 Gabor models corresponding to 6 scales of Gabor filters.

8.1.3.2 Classification

For training, the search region is limited to a small vicinity of each BMO point which is the region inside a donut defined by two ellipses centered at each BMO location. It is known that BMO always locates below the ILM surface; hence, if any parts of the search region fall above the ILM surface, they are excluded for feature extraction (e.g. the shaded region in Fig. 8.4a). The area inside the smaller ellipse represents the inherent subjectivity of manual delineation for identifying a BMO point and the positive class members are selected from this region. Since the training set is highly skewed (i.e. only one BMO point exists in each search region) and to reflect the inter-observer variability, we consider each BMO point along with its 4-neighborhood pixels as positive class (a total of 5) and randomly sampled 20 points from the search region (the area between the outer and inner ellipses) to represent the negative class (Fig. 8.4a). The appropriate size of the search region was computed in the training set such that in addition to the manual delineation (true BMO locations), an estimated 3D location for each BMO in the training set was computed by projecting the 2D location (i.e. (r, θ)-values) of each BMO point (that obtained in Section 8.1.2.3) to the BM surface. The estimated and true locations of BMO points were compared to obtain the range of estimation error. The radii of outer ellipse were computed such that more than 99% of the estimated BMO locations were included in the search region ($r_{\text{big}} = 300\mu\text{m}, r_{\text{small}} = 120\mu\text{m}$). The radii of the inner ellipse were set to $r_{\text{big}} = 90\mu\text{m}, r_{\text{small}} = 45\mu\text{m}$. The same set of intensity features that were used for creating the BMO_{L} model were extracted for both classes. The features were projected to the BMO_{L} model using their corresponding eigenvectors that were computed for creating PCA models. The number of trees was set to 500 and the

number of variables available for splitting at each tree node was set to square root of total number of predictors (28 NIP, 12 SGD, and 21 Gabor $\rightarrow \lceil \sqrt{\#predictors} \rceil = 8$).

For testing, in order to locate the search region, which is an ellipse with the same size as the outer ellipse of the donut used for training, we need an estimation of BMO location. Similar to obtaining the estimated location of BMO points in the training set, the 2D location (i.e. (r, θ)-values) of each BMO point computed in Section 8.1.2 were projected to the BM surface (the yellow surface in Fig. 8.4b) to estimate the corresponding z-values. All voxels inside the search region in the testing set are potential candidates for being a BMO point (Fig. 8.4b). Hence, the intensity features are extracted for all points inside the search region and projected to the BMO_L model using their corresponding eigenvectors.

The RF classifier computed the BMOness of all voxels inside the search region and generated the 3D likelihood map of voxels being a BMO point. The inverse of likelihood map (Fig. 8.4c) was utilized in the total cost function of finding the 3D BMO path.

8.1.4 Identifying the 3D BMO Path Using Dynamic Programming

The problem of finding the BMO 3D path is formulated as a shortest-path problem. Here, the goal is to find a path with minimum cost that satisfies a set of constraints. Assume that a directed acyclic graph (DAG) $\mathcal{G}(V, E)$ is constructed from the radial volume $\mathcal{R}$ of size $R \times Z \times \Theta$ with non-negative edge and node costs and we want to find the BMO locations as a minimum-cost 3D path $\mathcal{P} = \{V_\mathcal{P}, E_\mathcal{P}\}$ within $\mathcal{G}$. Each voxel in the volume is represented by a node in the graph; hence, the number of nodes in the graph, $|V|$, is equal to the number of voxels in the volume. Each node is connected only to its neighbors (i.e., the feasible nodes in the subsequent slice). As there is only one BMO endpoint in each slice, the nodes in the same slice are not connected to each other. The neighboring constraint in the r-direction and

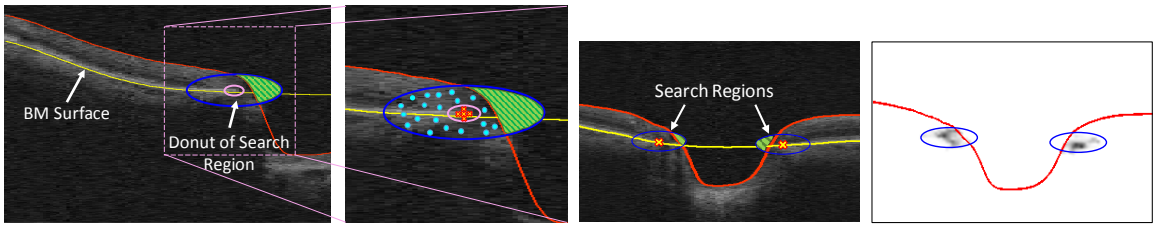

(a) (b) (c)

Figure 8.4: (a) Illustration of the donut of search region for training set. The negative class (cyan dots) are randomly sampled from the area between ellipses and the positive class (yellow crosses) are taken from the area inside the small purple ellipse. (b) Illustration of search region for testing set which is an ellipse with the same size as the outer ellipse (dark blue) of the donut around the estimated 3D BMO location (yellow cross). The green shaded areas in (a) and (b) are excluded from the search region due to the fact that BMO never locates above the ILM surface. (c) A slice (corresponding to the B-scan shown in (b)) of the 3D cost function utilized for identifying the BMO 3D path which is obtained by inverting the output of the RF classifier.

z-direction are $\Delta_r = 2$ and $\Delta_z = 1$, respectively which means the neighborhood of each node is a 3×5 rectangle in the next slice such that there is an edge between the node and its neighbors (Fig 8.5). The neighbors of each node in the subsequent slice is specified according to the maximum variations of BMO paths in-between slices in the training set. Additionally, since the BMO path is a closed circular path in the Cartesian domain, we need to assure that the computed shortest path is a closed loop (i.e., the first and last radial slices are considered as adjacent slices)

There are two types of costs in the graph: edge costs and node costs. The edge costs are responsible for smoothness of the path and they penalize the deviations from the BMO location in the previous slice. The penalizing function in r-direction is $f_r = (r_{\theta_1} - r_{\theta_2})^2$ and in the z-direction it is $f_z = |z_{\theta_1} - z_{\theta_2}|$ which generate the following edge weights for all neighborhoods:

$$W_r = \begin{bmatrix} 4 & 2 & 0 & 2 & 4 \\ 4 & 2 & 0 & 2 & 4 \\ 4 & 2 & 0 & 2 & 4 \end{bmatrix} \ , \ W_z = \begin{bmatrix} 1 & 1 & 1 & 1 & 1 \\ 0 & 0 & 0 & 0 & 0 \\ 1 & 1 & 1 & 1 & 1 \end{bmatrix} \tag{8.8}$$

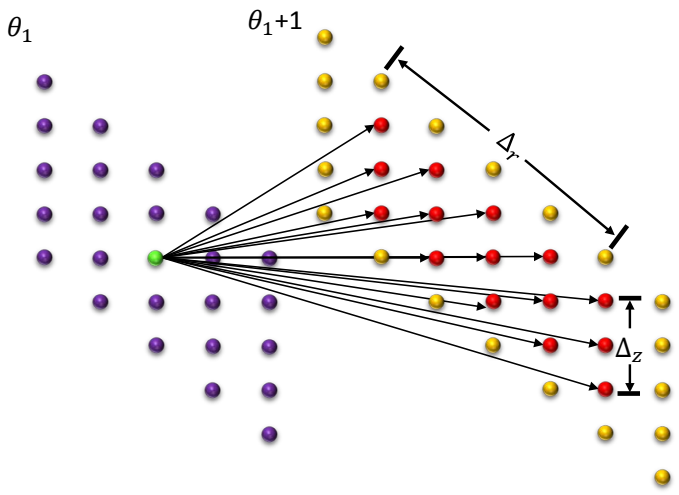

Figure 8.5: Graph construction. The are weighted edges between each node (green) and its neighboring nodes (red). The neighboring constraint in r-direction (Δ_r) and in z-direction (Δ_z) determine the amount of allowed variation from slice to slice.

The cost of the edge (u, v), C_{uv}, connecting nodes $u = (z_u, r_u, \theta_u)$ and $v = (z_v, r_v, \theta_v)$ is obtained by adding the weights (assuming W_r and W_z elements are expanded at $-2:2$ and $-1:1$ in r and z directions, respectively) as follows:

$$C_{uv} = W_r(z_u - z_v, r_u - r_v) + W_z(z_u - z_v, r_u - r_v). \tag{8.9}$$

Hence, the total cost of a feasible BMO path is as follows:

$$C_{\mathcal{P}} = \sum_{V \in V_{\mathcal{P}}} C_V(r_V, z_V, \theta_V) + \beta \sum_{E \in E_{\mathcal{P}}} C_E \tag{8.10}$$

where C_V is the 3D node cost computed by the random forest classifier in Section 8.1.3.2 and $0 < \beta < 1$ determines the importance of edge cost with respect to the node cost. In order to reflect the anatomical information that the BMO can touch the ILM surface but never pass it, the nodes in the search region that fall above the ILM surface are not considered as neighbors of any node in the graph (there is no edge connecting them to any other nodes).

In order to compute the minimum-cost shortest path through the constructed graph, dynamic programming (DP) approach is utilized. In order to solve the problem using DP we need to define the subproblem and the recursive formulation to solve the problem as well as the base case. Suppose we add a dummy node, s, and we connect all nodes in the first slice to s using identical zero-cost edges. Now the problem becomes to find the minimum-cost path from s to any node located in the last slice (the enforcement of circularity constraint will be explained later). We know that if $s \rightsquigarrow u \rightsquigarrow v$ is a shortest path from s to v, this implies that $s \rightsquigarrow u$ is a shortest path from s to u, as well; otherwise if there was a shorter path between s and u we would obtain a better path between s and v by replacing the $s \rightsquigarrow u$ with the shorter path. But we assumed that $s \rightsquigarrow u \rightsquigarrow v$ is a shortest path between s and v, so we have a contradiction. Based on this idea, we define the subproblem. Let us assume $OPT(v,k)$ is the minimum-cost path from s to node v in slice k, the recursive formulation for $OPT(v,k)$ can be written as the following:

$$OPT(v,k) = \min_{\substack{u \in V \\ (u,v) \in E}} \left\{ OPT(u,k-1) + C_{uv} + C_V(r_v, z_v, \theta_v) \right\}. \tag{8.11}$$

and the base case is $OPT(v,1) = C_V(r_v, z_v, \theta_v)$. The optimal solution can be efficiently computed using dynamic programming by computing the values in order of increasing k.

Here, the circularity constraint means that, assuming the first and last slices are adjacent slices, the path ends at one of the allowed neighbors of the starting node. In order to ensure that this condition is satisfied, we found all possible shortest paths that satisfied the circularity condition and picked the path with the minimum cost. To find all the shortest path satisfying the circularity constraint, we forced the path to start at a specific node in the first slice and end at one of its neighbors in the last slice. The enforcement was performed by deliberately increasing the cost of all

nodes in the search region of the first slice except for the starting node and repeating the same action for all nodes in the search region of the last slice except for the neighboring nodes.

8.1.5 Refinement of BMO Path in the z-Direction

The BMO path computed in Section 8.1.4 needs further refinement as the path was found in the downsampled (in the z-direction with $30 \times 30\mu$m voxel size in r-z plane) volume. Processing the data initially in the isotropic grid was beneficial for easily setting up the smoothness/neighborhood constraints for graph construction, saving time and space for extracting the features, training the RF classifier, and finding the shortest path (especially for computing all possible shortest paths satisfying the circularity constraint). In order to obtain the BMO path in the original image resolution ($30 \times 2\mu$m voxel size in r-z plane), a similar method as used to find the BMO path in the downsampled volume was utilized. However, the search region for refinement was restricted such that it only consisted of those 15 voxels in the original resolution that corresponded to the BMO point found in the lower resolution. Therefore, as r-values were fixed during this step, the refined z-values were computed as a shortest path with the circularity constraint within a small 2D image of size 15×360 in $Z \times \Theta$.

The node cost computation procedure is similar to that of Section 8.1.3. From the volumes in the training set, a new intensity model reflecting the intensity profile around the BMO in the original resolution was created (called BMO_Z representing the BMO model with original resolution in the z-direction). The model was obtained using the same set of features as in Section 8.1.3.1 and applying PCA such that 90% of the variation in the feature set was retained. For training the RF classifier a 15-voxel length array around each BMO point in the z-direction was involved. The positive class (BMO) included the BMO point itself and the voxels right above and below it (in order to resemble the inter-observer variability) and the negative class (non-BMO)

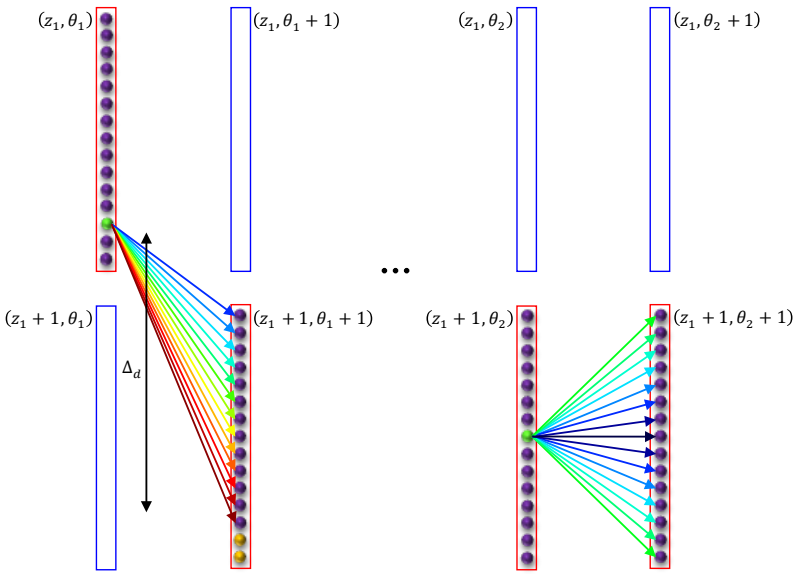

Figure 8.6: Refinement Graph, $\mathcal{G}_Z$, construction. The red box indicates one voxel on the BMO path in the downsampled volume which corresponds to 15 voxels in the original resolution. The edges are color coded with warmer colors corresponding to higher weights. For a particular node (green) in slice θ_1, all nodes in the subsequent slice, $\theta_1 + 1$, with a distance less than Δ_d are considered as neighbors. The yellow nodes indicate those nodes with a distance larger than Δ_d.

included the rest of the array (a total of 12). The intensity-based features of all points in positive and negative classes were computed and projected to the BMO_z model and the RF_z classifier was trained utilizing the projected intensity features. The number of trees and variables to be randomly extracted at each decision split were set to 500 and the square root of number of features, respectively.

As mentioned above, each BMO point (found in the lower resolution) contributes 15 voxels from the original resolution to the test set. The intensity-based features were computed for all points in the test set and projected to the BMO_z model. The trained RF_z classifier produced the likelihood map of each node being BMO. The inverted likelihood map served as the node cost in the graph construction. The graph $\mathcal{G}_Z = (V_Z, E_Z)$ consisted of 15×360 nodes and edges existed only between each node and its neighbors in the subsequent slice. The furthest neighbor of each node

has at most Δ_d distance in the z-direction for which the Δ_d is computed from the training set. The edge weight increases (Fig 8.6) as the distance of neighbors becomes larger via the penalizing function $f_d = |z_{d_1\theta_1} - z_{d_2\theta_2}|$. The final 3D BMO path was obtained by finding the shortest path with circularity constraint using the dynamic programming approach similar to that in Section 8.1.4.

8.2 Experimental Methods

8.2.1 Data

The training dataset includes 25 glaucomatous SD-OCT scans centered at the optic nerve head that were acquired using a Cirrus HD-OCT device (Carl Zeiss Meditec, Inc., Dublin, CA) at the University of Iowa. The size of each scan was 200×200×1024 voxels with a voxel size of 30×30×2 μm in the x-y-z direction. Similarly, the testing set includes 44 patients diagnosed with glaucoma suspect or open-angle glaucoma and an optic nerve head (ONH)-centered SD-OCT volumes (Cirrus, Carl Zeiss Meditec, Inc.; 200×200×1024 voxels corresponding to 6×6×2 mm^3) obtained in one eye of each patient.

8.2.2 Reference Standard

For training set, the BMO points were marked on all radial B-scans such that one expert first traced the BMO points on the 3D SD-OCT volume with two additional experts providing corrections resulting in final tracing that was the result of the consensus of three experts through a discussion. For the testing set, however, the BMO points were identified on 20 evenly-spaced randomly-picked radial slices by consensus of manual delineations from three experts (a total of 40 BMO points for each subject).

8.2.3 Experiments

As two separate datasets were available for training and testing purposes, the proposed method used the entire training set for creating the BMO models and training the classifiers and it was tested on the entire test set. The performance of the proposed BMO identification method (BMO_P) as well as our previous iterative method [24] (BMO_I) were evaluated on the 20 slices of each subject with manual delineation (BMO_M). The signed and unsigned distances of automated BMO points with manual BMO points in r-direction and z-direction, were measured separately. If the automated methods identify the BMO closer to the optic disk center, the sign of distance in r-direction is positive. Similarly, if the automated BMO (BMO_P/BMO_I) located below the manual BMO (BMO_M), the sign of distance in z-direction is positive. In addition, the distance of automated and manual BMO points in r-z plane was measured.

Furthermore, as enabling to automatically compute the BMO-MRW measure is one of the major applications of our proposed method, this structural parameter was computed using manual (BMO_M-MRW), proposed method (BMO_P-MRW) and the iterative approach (BMO_I-MRW). The signed and unsigned differences of BMO_P-MRW and BMO_I-MRW with BMO_M-MRW (called the BMO-MRW error) were calculated. The Pearson correlation as well as root mean square error (RMSE) of automated BMO-MRW measures with respect to the manual BMO-MRW were also computed. Zou's method for comparing two overlapping correlations based on two dependent groups [112] was utilized to compare the Pearson correlations of BMO_M-MRW with BMO_P-MRW and BMO_I-MRW (p-values < 0.05 was considered significant).

8.3 Results

Fig. 8.7 shows example results of BMO identification and BMO-MRW computation using the automated methods and the reference standard. For better visualization, only the central part of each B-scan is shown. The first row in Fig. 8.7 shows an

example that both automated methods successfully identified the BMO points. The second and third examples demonstrate how presence of the externally oblique border tissue causes erroneous BMO identification for the automated approaches; however, the proposed method is less affected than the iterative approach. The externally oblique border tissue attaches to the end of BM surface and resembles the BMO points which influences the automated methods. The last example demonstrates a case that the results of both iterative approach and the proposed method are affected by the presence of an ambiguous border tissue. In such cases, without using the 3D contextual information, it is very difficult (even for humans) to mark the exact location of BMO. Note that when there is no border tissue present, the iterative and our proposed methods have comparable performances (Fig. 8.7).

The unsigned and signed BMO identification errors in r-direction, z-direction, and r-z plane are reported in Table 8.1. Based on BMO identification errors, the proposed method outperformed our previous iterative approach [24] in z-direction, r-direction, and r-z plane ($p < 0.05$). Similarly, the signed BMO identification error, showed that the proposed method has significantly lower errors in r and z directions than the iterative approach ($p < 0.05$). The maximum unsigned BMO identification error in r and z directions and in the r-z plane for the proposed (iterative) method were 76.5 (148.5), 42.8 (92.4), and 85.1 (166.17) μm, respectively.

Table 8.2 shows the measurements associated with the structural parameter BMO-MRW including unsigned and signed BMO-MRW error and RMSE. Based on the unsigned BMO-MRW error, the proposed method had a significantly lower BMO-MRW error than the iterative approach ($p < 0.05$). Similarly, the signed BMO-MRW error showed that BMO_P-MRW has significantly smaller bias than BMO_I ($p < 0.05$). The mean$\pm$standard deviation of manual and automated BMO-MRW measures were 182.41$\pm$86.07 μm (BMO_M-MRW), 184.46$\pm$81.61 μm (BMO_P-MRW), and 187.33$\pm$88.51 μm (BMO_I-MRW), respectively. The maximum unsigned BMO-

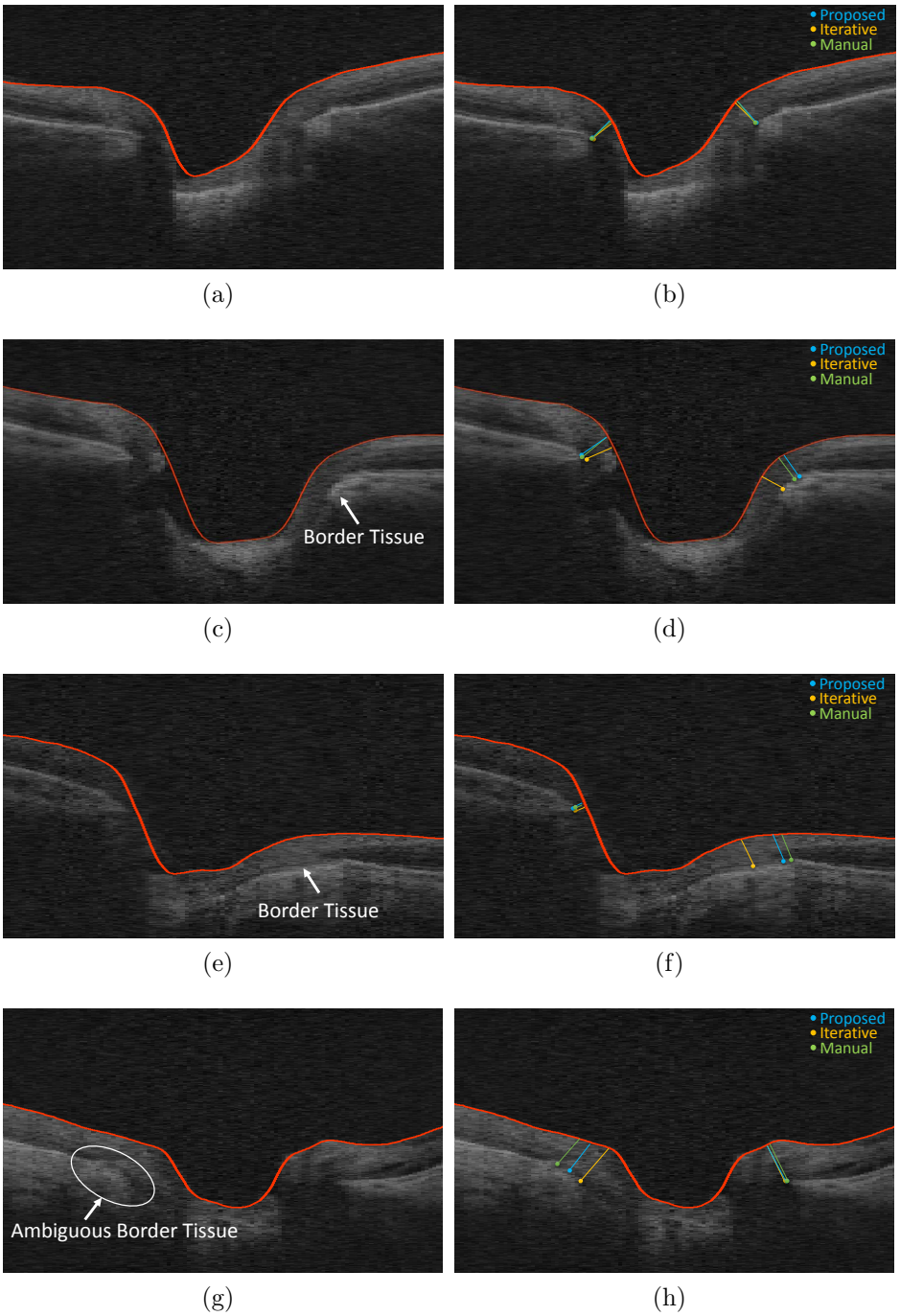

Figure 8.7: Example results, left column is the original B-scan along with the ILM surface and the right column demonstrates the segmentation results. The blue, yellow, and green circles indicate the BMO_P, BMO_I, and BMO_M, respectively. The lines connecting the BMO points to the ILM surface, indicate the corresponding BMO-MRW measures.

Table 8.1: Unsigned and signed BMO identification error in r-direction, z-direction, and r-z plane in μm (Mean± SD).

	Unsigned		Signed	
Error	Antony *et al.* [24]	**Proposed**	Antony *et al.* [24]	**Proposed**
r-direction	49.53±30.41	37.98±14.91	26.49±40.22	-9.49±24.58
z-direction	31.58±21.06	22.28± 8.58	25.45±14.37	8.33±17.72
r-z plane	63.03±36.28	49.28±16.78	–	–

Table 8.2: BMO-MRW error measurements in μm (Mean± SD).

Error	Antony *et al.* [24]	**Proposed**
Unsigned error	26.65±13.27	22.22± 5.99
Signed error	6.61±18.59	- 0.30±12.44
RMSE	17.99± 8.15	11.62± 4.63

MRW error of the proposed (iterative) method was 38.08 (75.10) μm. Furthermore, the proposed method had a smaller RMSE than the iterative approach for computing the BMO-MRW ($p < 0.05$).

The comparison of Pearson correlations of BMO_M-MRW with BMO_P-MRW (0.992) and BMO_I-MRW (0.980) using the method in [112] showed that the proposed method had significantly higher correlation with the reference standard than the iterative approach ($p < 0.05$). Additionally, Fig. 8.8 depicts the Bland-Altman plots of BMO_P-MRW and BMO_I-MRW with respect to BMO_M-MRW where the tighter fit and smaller error of the proposed method in computing the BMO-MRW are observable.

8.4 Discussion and Conclusion

In this chapter, we presented a machine-learning graph-based approach for automated segmentation of Bruch's membrane opening from SD-OCT volumes. Our results showed that the proposed method successfully identifies the opening points

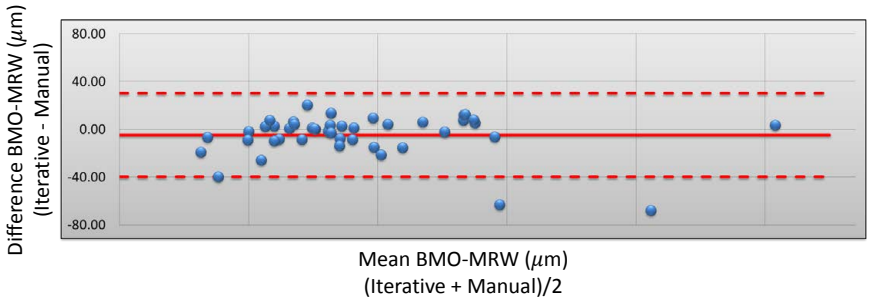

(a)

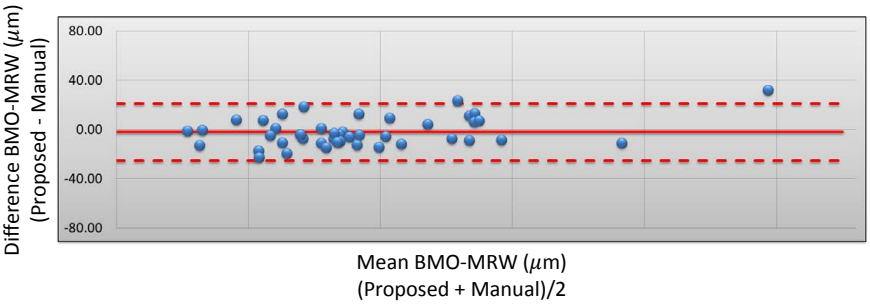

(b)

Figure 8.8: The Bland-Altman plots of (a) BMO_I-MRW and (b) BMO_P-MRW in comparison with BMO_M-MRW. The proposed method has a tighter fit and lower error than the iterative approach.

of the BM surface such that it enables computing the structural parameter Bruch's membrane opening-minimum rim width (BMO-MRW) automatically. The proposed method identifies the estimated location of BMO points by finding the BMO projection locations using a similar graph-theoretic approach reported in [22] with incorporation of shape prior and mapping them onto the BM surface. The estimated 3D locations were utilized to find the 3D BMO loop by formulating the problem as computing the minimum-cost path within the 3D volume using dynamic programming. Since defining a mathematical model for BMO points is not feasible, as they appear differently even in slices corresponding to a single subject, we learned the intensity-based attributes of BMO points (in the form of PCA models) using a random forest classifier which computed the cost function needed for identifying the minimum-cost path.

To the best of our knowledge, our previous work [24] was the only non-commercialized approach reported for identifying the 3D BMO points automatically. We previously proposed an iterative graph-theoretic approach to segment the BM surface along with its opening. A graph-theoretic approach was utilized for identifying the initial 2D segmentation of BMO points, and while the (r, θ) pairs kept unchanged, we looked for the corresponding z-values. Upon finding the 3D BMO locations as part of the surface + hole method, a new radial projection image was created from which the updated 2D locations were identified. This iteration was repeated until convergence. In this chapter, we aimed to improve our previous method by removing the iterations and eliminating the two-step identification of the (r, θ) pairs and z values and instead, finding the (r, θ, z) coordinates as part of a 3D loop in a single run.

The other limitation of the iterative approach was that in the presence of externally oblique border tissue [19], the iteration would continue to search for the BMO point along the anterior surface of the border tissue. As discussed in Chapter 5, the

presence of externally oblique border tissue confuses the algorithm and causes the algorithm to find the BMO point on the border tissue instead of end of BM surface. The presence of externally oblique border tissue was definitely one of the main reasons for the large positive signed border positioning errors of the iterative method reported in Table 8.1. The issue of presence of border tissue was addressed in the proposed method to a certain extent by setting some edge weights to penalize the deviation from the expected shape of path while performing shortest path identification.

The penalizing weights not only helped with avoiding the border tissues, but they were also effective in dealing with the vessels shadows. Unlike a typical BMO point locating at the end of a bright band, co-localizing a BMO point with a blood vessel causes the BMO point to be located inside a dark region. Presenting the penalizing weights helped the BMO path to keep the natural trend of the BMO trajectories in the volume and not deviate from the expected shape of the BMO path. However, it must be noted that setting up high penalizing weights is not the solution for the issues of presence of border tissue and blood vessel shadows. The reason is that even though higher penalizing weights leads to a stiffer BMO path with minimal variation in the r- and z-directions; however, there are cases that the BMO path must be capable of following the "true" natural translation of the BMO points throughout the volume. Hence, there is a trade off between being capable of dealing with the presence of border tissue and blood vessel shadows and following the true displacements of the BMO path throughout the volume.

Additionally, the issue of presence of border tissue and the blood vessels were also dealt with in identifying the 2D location of the BMO points. This was performed by enforcing the prior shape constraint in the r-direction during applying the graph-theoretic approach. Identifying an accurate 2D location of BMO points is important as it leads to a better estimated 3D location which requires smaller search region to find the actual BMO point. The size of the search region was computed based on the

accuracy of estimated 3D BMO points in the training set. Shrinking the searching area decreases the BMO point candidates and the reduces the size of the graph to be solved.

In summary, we proposed a machine-learning graph-based approach for segmentation of BMO point from SD-OCT volumes. After transferring the volumes to the radial domain, radial projection images were computed by segmenting the intraretinal surfaces. The projection images were processed using SWT in order to create the vessel-free images in which the blood vessels were significantly suppressed. An edge-based cost function was obtained from the gradient of vessel-free images to incorporate in a graph-theoretic approach for finding the 2D location of BMO points (r, θ). The volumes were downsampled in the z-direction to achieve an isotropic grid (with the same size as the physical resolution) and an estimated 3D location of BMO points, (r, z, θ), were obtained by projecting the 2D coordinations onto the BM surface. An elliptical search region around each estimated location was considered to form a 3D tube from which the 3D BMO points were identified by looking for the minimum-cost path within the searching tube using dynamic programming. The cost function for finding the minimum-cost path was computed by inversing the likelihood map generated by a RF classifier based on the resemblance of each point inside the searching tube to the BMO intensity models. Once the BMO points were identified, a similar approach as used to find the BMO path within the downsampled volume was utilized to refine the z-values such that the 3D coordinates of BMO points in image resolution were obtained.

CHAPTER 9
CONCLUSION

The overall underlying theme of this thesis was to benefit from complementary information available from multimodal imaging of the retina in order to automatically segment the optic nerve head structures by incorporation of the machine-learning techniques into theoretical graph-based approaches. Here, the structural parameter of interest was Bruch's membrane opening-minimum rim width (BMO-MRW) which estimates the remaining neuroretinal rim tissue and could be employed for diagnosis and monitoring glaucoma. Since it has been shown that BMO-MRW is superior to other conventional structural parameters such as CDR in diagnosis of glaucoma [20], it is important to be able to compute this parameter automatically. Hence, the focus of the current work was on enabling automated computation of BMO-MRW which required precise segmentation of ILM surface and BMO points.

Additionally, since during the screening of glaucoma patients, both fundus and SD-OCT modalities are acquired to monitor structural changes, we also proposed to benefit from complementary information of both sources in designing automated approaches for segmenting optic disc structures. For instance, since the visibility of retinal blood vessels inside the optic disc region is higher in fundus photographs, we computed the vessel maps from fundus photographs and overlaid the results on SD-OCT volumes.

Chapter 4 further demonstrated the benefit of combining complementary information from SD-OCT modality and fundus photography for 2D segmentation of optic disc (BMO points) and cup boundaries. Our results showed the superiority of the multimodal approach over the unimodal methods which was consistent with results of the previous work for multimodal segmentation of the retinal blood vessels [93]. The optic disc and cup boundaries were segmented using a graph-theoretic approach for which the cost functions were computed automatically by random forest classifiers

that were trained using a multimodal feature set. For creating the multimodal feature set, different information was extracted from intrinsic red, green, and blue channels as well as three color-opponent channels of red-green, blue-yellow, and dark-bright where the original use of the color-opponent channels as in [7] is motivated by the theory of color vision.

Correspondingly, in order to be able to use complementary information form fundus and SD-OCT modalities, we needed to register the images such that multimodal information was extracted from the same locations in the images. We used an ICP-based registration method in Chapter 4 for registering fundus photographs and SD-OCT volumes where retinal blood vessel maps were utilized for identifying the corresponding points (e.g. bifurcations and vessel-crossings) between images. The vessel segmentation algorithms, however, could introduce errors to the registration process by producing false positives. Additionally, results of vessel segmentation algorithms [94] are scale-dependent and parameter-tuning based on the scale of the input image must be performed in order to obtain satisfactory results. As our second glaucoma dataset included color and stereo fundus photographs which have different sizes and resolutions, in some cases, the ICP registration method utilized in Chapter 4 needed additional manual corrections and failed to register the multimodal pairs precisely.

Therefore, with the aim of removing the scale-dependency and increasing the speed of the registration process, we proposed a feature-based registration algorithm in Chapter 6 to align the fundus photographs (including color and stereo fundus) with SD-OCT volumes using histogram of oriented gradients. The proposed registration method extracts the common structural information (mostly from the retinal blood vessels) within the surrounding region of each control point, which was detected using FAST corner detection, without need of segmenting the blood vessels. The histogram of oriented gradients attributes were employed to find the matching control

points between image pairs. Finally, the fundus photographs were registered to their corresponding SD-OCT volumes using the matched CPs.

The use of complementary information from multimodal images was extended further in Chapter 7, where the blood vessels were segmented from the fundus photographs and the cost function for segmenting the ILM surface was modified at the blood vessel location. Due to the technical limitation that exists in the original Iowa reference algorithm method [16] (i.e. surfaces must intersect with each column only once), there are errors in segmenting steep slopes presenting in deeper cups of glaucomatous SD-OCT volumes. Moreover, there are situations that we need to have the ability to cut through the blood vessels in order to enable a more precise computation of BMO-MRW (Fig. 7.2). Oguz *et al.* [135] showed the benefit of utilizing GVF in brain segmentation. Similarly, in this work, in order to obtain a precise segmentation of the ILM surface and manage the issue of presence of retinal blood vessels and steep slopes, we benefited from the gradient vector flow (GVF) field. The SD-OCT volumes were resampled using a set of non-overlapping columns, which were computed from the GVF field of the initial segmentation of the ILM surface. Since the new columns are normal at the ILM surface, the resampling transforms the ILM surface into a very smooth structure. The non-overlapping GVF-based columns also served as the columns in the graph construction where the prior information regarding the shape of ILM surface in the resampled volume was incorporated in constructing the graph from which the resampled ILM surface was segmented.

Chapter 8 summarized an automated approach for 3D segmentation of BMO points form SD-OCT volumes. A similar approach to the graph-theoretic method that was utilized in Chapter 4 with incorporation of shape prior information was employed to identify the 2D locations of BMO points. The estimated 3D BMO points were obtained by projecting the 2D coordinates onto the BM surface. We formulated the 3D BMO segmentation as finding the minimum-cost path (i.e. closed loop) within the

radial volume. Following the overall theme of the thesis, we benefited from machine-learning techniques for computing the required cost-functions and a random forest classifier was used to compute the 3D cost function needed for finding the shortest path. The random forest classifier was trained using a set of intensity-based features including Gaussian derivative, Gabor, and intensity profile of the estimated BMO point's neighboring region where the dimensionality of the feature space was reduced using the PCA technique. Formulating the problem as finding the shortest path within the radial volume allowed us to enforce desired shape constraints and also assure that the path is a closed loop. The circularity constraint was applied by running the dynamic programming multiple times (i.e. the number of possible starting points) and constraining the beginning and ending points of the path in each run. The path with the lowest cost was considered as the 3D BMO segmentation result. In order to be able to create the BMO intensity models in an isotropic r-z grid, the volume was downsampled in the z-direction. Hence, a similar approach as used to find the BMO path within the downsampled volume was utilized to refine the z-values such that the 3D coordinates of BMO points in image resolution were obtained.

The genuine 3D segmentation method proposed in Chapter 8 enabled more accurate identification of BMO points which results in more precise computation of BMO-MRW measure and consequently, more accurate diagnosis of glaucoma.

Besides developing automated algorithms for computing the BMO-MRW parameters, we also investigated the effect of presence of externally oblique border tissue (EOBT) in measuring BMO-MRW in Chapter 5. As externally oblique border tissue attaches to the end of the Bruch's membrane surface, the presence of EOBT causes identification of the ending point of the Bruch's membrane surface to be challenging. Hence, we proposed EOBT-MRW as an alternative measure for computing BMO-MRW when EOBT exists due to the fact that computing EOBT-MRW does not require identification of the exact location of BMO points. In contrast to BMO-MRW

which is a point-to-surface shortest distance, EOBT-MRW is a surface-to-surface shortest distance and measures the minimum Euclidean distance between the ILM surface and the anterior surface of border tissue. Our results showed that there was not a significant difference between structure-structure correlations of RNFLT with BMO-MRW and EOBT-MRW. This implies that, in addition to the point-to-surface measure, BMO-MRW, the remaining neuroretinal rim tissue can be also estimated using the surface-to-surface measure, EOBT-MRW without requiring precise definition of BMO point.

In addition to proposing a new structural parameter, we also compared two rim-width-based parameters, BMO-MRW and BMO-HRW. Since the BMO-HRW does not always measure the minimum Euclidean distance between the BMO point and ILM surface, the possibility of overestimating the remaining neuroretinal rim tissue using BMO-HRW exists. Hence we compared the structure-structure correlations of these two parameters with RNFLT and the result showed that BMO-MRW outperformed BMO-HRW. Significantly higher correlation of BMO-MRW with RNFLT indicates that BMO-MRW better estimates the remaining rim tissue than BMO-HRW.

In conclusion, we demonstrated examples of how automated algorithms for medical image analysis could benefit from combining information available from different resources and modalities. Similarly, automated analysis of medical images in other areas could profit from combining available complementary information in variety of applications such as segmentation purposes and diagnosis and severity-related classification. Furthermore, we demonstrated the flexibility and power of the graph-theoretic approaches in different tasks and how we satisfied the task-objectives by incorporating the required constraints and/or prior information in the graph construction. Lastly, we showed that machine-learning techniques can be employed for computing cost functions of the graph-theoretic approaches. Utilizing the machine-learning approach

for designing the cost functions instead of hand-designed cost functions are beneficial when we would like the cost functions to include information from different resources or modalities. In addition, machine-learning approaches are expected to perform better on producing the cost-function for unseen datasets than hand-designed techniques. The algorithms proposed in this work were applied to ONH-centered fundus photographs and SD-OCT volumes of glaucoma patients; however, they can be an inspiration for other medical/non-medical image analysis applications where an appropriate training set for training the classifiers exist.

REFERENCES

[1] D. Huang, E. A. Swanson, C. P. Lin, J. S. Schuman, W. G. Stinson, W. Chang, M. R. Hee, T. Flotte, K. Gregory, and C. A. Puliafito, "Optical coherence tomography," *Science*, vol. 254, no. 5035, pp. 1178–1181, Nov. 1991.

[2] B. C. Chauhan and C. F. Burgoyne, "From clinical examination of the optic disc to clinical assessment of the optic nerve head: a paradigm change," *Am J Ophthalmol*, vol. 156, no. 2, pp. 218–227, 2013.

[3] B. C. Chauhan, N. O'Leary, F. Almobarak, A. S. C. Reis, H. Yang, G. P. Sharpe, D. M. Hutchison, M. T. Nicolela, and C. F. Burgoyne, "Enhanced detection of open-angle glaucoma with an anatomically accurate optical coherence tomography-derived neuroretinal rim parameter," *Ophthalmology*, vol. 120, no. 3, pp. 535–543, 2013.

[4] N. G. Strouthidis, J. Grimm, G. Williams, G. Cull, D. J. Wilson, and C. F. Burgoyne, "A comparison of optic nerve head morphology viewed by spectral domain optical coherence tomography and by serial histology," *Invest Ophthalmol Vis Sci*, vol. 51, no. 3, pp. 1464–1474, 2010.

[5] A. S. C. Reis, G. P. Sharpe, H. Yang, M. T. Nicolela, C. F. Burgoyne, and B. C. Chauhan, "A comparison of optic nerve head morphology viewed by spectral domain optical coherence tomography and by serial histology," *Ophthalmology*, vol. 119, no. 4, pp. 738–747, 2012.

[6] F. A. Almobarak, NeilÓLeary, A. S. C. Reis, G. P. Sharpe, D. M. Hutchison, M. T. Nicolela, and B. C. Chauhan, "Automated segmentation of optic nerve head structures with optical coherence tomography," *Invest Ophthalmol Vis Sci*, vol. 55, no. 22, pp. 1161–1168, 2014.

[7] M. D. Abràmoff, W. L. M. Alward, E. C. Greenlee, L. Shuba, C. Y. Kim, J. H. Fingert, and Y. H. Kwon, "Automated segmentation of the optic disc from stereo color photographs using physiologically plausible features," *Invest Ophthalmol Vis Sci*, vol. 48, no. 4, pp. 1665–1673, Apr. 2007.

[8] J. Cheng, J. Liu, Y. Xu, F. Yin, D. W. K. Wong, N.-M. Tan, D. Tao, C.-Y. Cheng, T. Aung, and T. Y. Wong, "Superpixel classification based optic disc and optic cup segmentation for glaucoma screening," *IEEE Trans. Med. Img.*, vol. 32, no. 6, pp. 1019–1032, June 2013.

[9] J. Xu, O. Chutatape, E. Sung, C. Zheng, and P. C. T. Kuan, "Optic disk feature extraction via modified deformable model technique for glaucoma analysis," *Pattern Recogn*, vol. 40, no. 7, pp. 2063–2076, July 2007.

[10] F. Yin, J. Liu, S. H. Ong, Y. Sun, D. W. K. Wong, N. M. Tan, C. Cheung, M. Baskaran, T. Aung, and T. Y. Wong, "Model-based optic nerve head segmentation on retinal fundus images," in *33rd Ann. Int. Conf. IEEE EMBS*, Boston, Massachusetts USA, Aug. 2011, pp. 2626–2629.

[11] J. Lowell, A. Hunter, D. Steel, A. Basu, R. Ryder, E. Fletcher, , and L. Kennedy, "Optic nerve head segmentation," *IEEE Trans. Med. Img.*, vol. 23, no. 2, pp. 256–264, Feb. 2008.

[12] R. Chràsteka, M. Wolfa, K. Donatha, H. Niemanna, D. Paulusb, T. Hothornc, B. Lausenc, R. Lmmerd, C. Mardind, and G. Michelsond, "Automated segmentation of the optic nerve head for diagnosis of glaucoma," *Med. Img. Anal.*, vol. 9, no. 4, pp. 297–314, Aug. 2005.

[13] M. B. Merickel Jr, X. Wu, M. Sonka, and M. D. Abràmoff, "Optimal segmentation of the optic nerve head from stereo retinal images," in *Proc. SPIE, Med. Img. 2006: Physiology, Function, and Structure from Medical Images*, vol. 6143, 2006, p. 61433B (8 pages).

[14] M. B. Merickel Jr, M. D. Abràmoff, M. Sonka, and X. Wu, "Segmentation of the optic nerve head combining pixel classification and graph search," in *Proc. SPIE, Med. Img. 2007: Img. Proc.*, vol. 6512, 2007, p. 651215 (10 pages).

[15] Y. Zheng, D. Stambolian, J. OBrien, and J. C. Gee, "Optic disc and cup segmentation from color fundus photograph using graph cut with priors," in *Proc. MICCAI, 2013, Part II*, vol. 8150, Nagoya, Japan, Sept. 2013, pp. 75–82.

[16] K. Lee, M. Niemeijer, M. K. Garvin, Y. H. Kwon, M. Sonka, and M. D. Abràmoff, "Segmentation of the optic disc in 3-D OCT scans of the optic nerve head," *IEEE Trans. Med. Imag.*, vol. 29, no. 1, pp. 159–168, 2010.

[17] M. D. Abràmoff, K. Lee, M. Niemeijer, W. L. M. Alward, E. C. Greenlee, M. K. Garvin, M. Sonka, and Y. H. Kwon, "Automated segmentation of the cup and rim from spectral domain OCT of the optic nerve head," *Invest Ophthalmol Vis Sci*, vol. 50, no. 12, pp. 5778–5784, Dec. 2009.

[18] Z. Hu, M. D. Abràmoff, Y. H. Kwon, K. Lee, and M. K. Garvin, "Automated segmentation of neural canal opening and optic cup in 3D spectral optical coherence tomography volumes of the optic nerve head," *Invest Ophthalmol Vis Sci*, vol. 51, no. 11, pp. 5708–5717, Nov. 2010.

[19] A. S. Reis, G. P. Sharpe, H. Yang, M. T. Nicolela, C. F. Burgoyne, and B. C. Chauhan, "Optic disc margin anatomy in patients with glaucoma and normal controls with spectral domain optical coherence tomography," *Ophthalmology*, vol. 119, no. 4, pp. 738–747, Apr. 2012.

[20] B. C. Chauhan, N. O'Leary, F. A. AlMobarak, A. S. Reis, H. Yang, G. P. Sharpe, D. M. Hutchison, M. T. Nicolela, and C. F. Burgoyne, "Enhanced detection of open-angle glaucoma with an anatomically accurate optical coherence tomography–derived neuroretinal rim parameter," *Ophthalmology*, vol. 120, no. 3, pp. 535–543, Mar. 2013.

[21] B. C. Chauhan and C. F. Burgoyne, "From clinical examination of the optic disc to clinical assessment of the optic nerve head: A paradigm change," *Am J Ophthalmol*, vol. 156, no. 2, pp. 218–227, Aug. 2013.

[22] M. S. Miri, M. D. Abràmoff, K. Lee, M. Niemeijer, J.-K. Wang, Y. H. Kwon, and M. K. Garvin, "Multimodal segmentation of optic disc and cup from SD-OCT and color fundus photographs using a machine-learning graph-based approach," *IEEE Trans. Med. Imag.*, vol. 34, no. 9, pp. 1854–1866, Sept. 2015.

[23] H. Fu, D. Xu, S. Lin, D. W. K. Wong, and J. Liu, "Automatic optic disc detection in OCT slices via low-rank reconstruction," *IEEE Trans. Biomed. Eng.*, vol. 62, no. 4, pp. 1151–1158, Apr. 2015.

[24] B. J. Antony, M. S. Miri, M. D. Abràmoff, Y. H. Kwon, and M. K. Garvin, "Automated 3D segmentation of multiple surfaces with a shared hole: Segmentation of the neural canal opening in SD-OCT volumes," in *Medical Image Computing and Computer-Assisted Intervention (MICCAI)*, vol. 8673, no. Pt 1, 2014, pp. 739–746.

[25] D. C. Fernàndez, H. M. Salinas, and C. A. Puliafto, "Automated detection of retinal layer structures on optical coherence tomography images," *Opt Express*, vol. 13, no. 25, pp. 10 200–10 216, 2005.

[26] M. Baroni, P. Fortunato, and A. L. Torre, "Towards quantitative analysis of retinal features in optical coherence tomography," *Med Eng Phys*, vol. 29, no. 4, pp. 432–441, May 2007.

[27] M. Shahidi, Z. Wang, and R. Zelkha, "Quantitative thickness measurement of retinal layers imaged by optical coherence tomography," *Am J Ophthalmol*, vol. 139, no. 6, pp. 1056–1061, June 2005.

[28] A. Chan, J. S. Duker, H. Ishikawa, T. H. Ko, J. S. Schuman, and J. G. Fujimoto, "Quantification of photoreceptor layer thickness in normal eyes using optical coherence tomography," *Retina*, vol. 26, no. 6, pp. 655–660, 2006.

[29] H. Ishikawa, D. M. Stein, G. Wollstein, S. Beaton, J. G. Fujimoto, and J. S. Schuman, "Macular segmentation with optical coherence tomography," *Invest Ophthalmol Vis Sci*, vol. 46, no. 6, pp. 2012–2017, June 2005.

[30] A. M. Bagci, M. Shahidi, R. Ansari, M. Blair, N. P. Blair, and R. Zelkha, "Thickness profiles of retinal layers by optical coherence tomography image segmentation," *Am J Ophthalmol*, pp. 679–687, Nov. 2008.

[31] T. Fabritius, S. Makita, M. Miurä, R. Myllyla, and Y. Yasuno, "Automated segmentation of the macula by optical coherence tomography," *Opt Express*, vol. 17, no. 18, pp. 15 659–15 669, Aug. 2009.

[32] O. Tan, G. Li, A. T.-H. Lu, R. Varma, D. Huang, and Advanced Imaging for Glaucoma Study Group, "Mapping of macular substructures with optical coherence tomography for glaucoma diagnosis," *Ophthalmology*, vol. 115, no. 6, pp. 949–956, June 2008.

[33] O. Tan, V. Chopra, A. T.-H. Lu, J. S. Schuman, H. Ishikawa, G. Wollstein, R. Varma, and D. Huang, "Detection of macular ganglion cell loss in glaucoma by Fourier-domain optical coherence tomography," *Ophthalmology*, vol. 116, no. 12, pp. 2305–2314.e2, Dec. 2009.

[34] R. J. Zawadzki, A. R. Fuller, D. F. Wiley, B. Hamann, S. S. Choi, and J. S. Werner, "Adaptation of a support vector machine algorithm for segmentation and visualization of retinal structures in volumetric optical coherence tomography data sets," *J Biomed Opt*, vol. 12, no. 4, p. 41206, Dec. 2007.

[35] F. Rossant, I. Ghorbel, I. Bloch, M. Paques, and S. Tick, "Automated segmentation of retinal layers in OCT imaging and derived ophthalmic measures," in *IEEE International Symposium on Biomedical Imaging: From Nano to Macro (ISBI 2009)*, 2009, pp. 1370–1373.

[36] K. A. Vermeer, J. van der Schoot, H. G. Lemij, and J. F. de Boer, "Automated segmentation by pixel classification of retinal layers in ophthalmic OCT images," *Biomed Opt Express*, vol. 2, no. 6, pp. 1743–1756, June 2011.

[37] A. Mishra, A.Wong, K. Bizheva, and D. A. Clausi, "Intra-retinal layer segmentation in optical coherence tomography images," *Opt Express*, vol. 17, no. 26, pp. 23 719–23 728, 2009.

[38] A. Yazdanpanah, G. Hamarneh, B. R. Smith, and M. V. Sarunic, "Segmentation of intraretinal layers from optical coherence tomography images using an active contour approach," *IEEE Trans. Med. Imag.*, vol. 30, no. 2, pp. 484–496, Feb. 2011.

[39] F. Rathke, S. Schmidt, and C. Schnörr, "Order preserving and shape prior constrained intra-retinal layer segmentation in optical coherence tomography," in *Medical Image Computing and Computer-Assisted Intervention (MICCAI)*, vol. 14, no. Pt 3, Jan. 2011, pp. 370–377.

[40] V. Kajić, B. Považay, B. Hermann, B. Hofer, D. Marshall, P. L. Rosin, and W. Drexler, "Robust segmentation of intraretinal layers in the normal human fovea using a novel statistical model based on texture and shape analysis," *Opt Express*, vol. 18, no. 14, pp. 14 730–14 744, July 2010.

[41] Q. Yang, C. A. Reisman, Z. Wang, Y. Fukuma, M. Hangai, N. Yoshimura, A. Tomidokoro, M. Araie, A. S. Raza, D. C. Hood, and K. Chan, "Automated layer segmentation of macular OCT images using dual-scale gradient information," *Opt Express*, vol. 18, no. 20, pp. 21 293–21 307, 2010.

[42] S. J. Chiu, X. T. Li, P. Nicholas, C. Toth, J. Izatt, and S. Farsiu, "Automatic segmentation of seven retinal layers in SD-OCT images congruent with expert manual segmentation," *Opt Express*, vol. 18, no. 18, pp. 19 413–19 428, Aug. 2010.

[43] S. J. Chiu, J. a. Izatt, R. V. OĆonnell, K. P. Winter, C. a. Toth, and S. Farsiu, "Validated automatic segmentation of AMD pathology including drusen and geographic atrophy in SD-OCT images," *Invest Ophthalmol Vis Sci*, vol. 53, no. 1, pp. 53–61, Jan. 2012.

[44] M. K. Garvin, M. D. Abràmoff, X. Wu, S. R. Russell, T. L. Burns, and M. Sonka, "Automated 3-D intraretinal layer segmentation of macular spectral-domain optical coherence tomography images," *IEEE Trans. Med. Imag.*, vol. 28, no. 9, pp. 1436–1447, 2009.

[45] Q. Song, X. Wu, and Y. Liu, "Simultaneous searching of globally optimal interacting surfaces with shape priors," in *IEEE Conference on Computer Vision and Patter Recognition (CVPR 2010)*, 2010.

[46] B. J. Antony, M. D. Abràmoff, K. Lee, P. Sonkova, P. Gupta, Y. H. Kwon, M. Niemeijer, Z. Hu, and M. K. Garvin, "Automated 3D segmentation of intraretinal layers from optic nerve head optical coherence tomography images," in *Proc. SPIE, Med. Img. 2010: Biomed. App. Molec., Struct., and Funct. Img*, vol. 7626, 2010, p. 76260U (12 pages).

[47] B. E. Klein, R. Klein, W. E. Sponsel, T. Franke, L. B. Cantor, J. Martone, and M. J. Menage, "Prevalence of glaucoma. The Beaver Dam Eye Study," *Ophthalmology*, vol. 99, no. 10, p. 1499, 1992.

[48] D. S. Friedman, R. C. Wolfs, B. J. O'Colmain, B. E. Klein, H. R. Taylor, S. West, M. C. Leske, P. Mitchell, N. Congdon, and J. Kempen, "Prevalence of open-angle glaucoma among adults in the United States," *Arch Ophthalmol*, vol. 22, no. 4, p. 532, 2004.

[49] H. A. Quigley and A. T. Broman, "The number of people with glaucoma worldwide in 2010 and 2020," *B J Ophthalmol*, vol. 90, no. 3, pp. 262–267, 2006.

[50] M. D. Abràmoff, M. K. Garvin, and M. Sonka, "Retinal imaging and image analysis," *IEEE Rev. Biomed. Eng.*, vol. 3, pp. 169–208, 2010.

[51] F. Medeiros, L. Zangwill, C. Bowd, R. Vessani, R. S. JR, and R. N. Weinreb, "Evaluation of retinal nerve fiber layer, optic nerve head, and macular thickness measurements for glaucoma detection using optical coherence tomography," *Am J Ophthalmol*, vol. 139, no. 1, pp. 44–55, 2005.

[52] J. E. DeLeón-Ortega, S. N. Arthur, G. McGwin, A. Xie, B. E. Monheit, and C. A. Girkin, "Discrimination between glaucomatous and nonglaucomatous eyes using quantitative imaging devices and subjective optic nerve head assessment," *Invest Ophthalmol Vis Sci*, vol. 47, no. 8, pp. 3374–3380, Aug. 2006.

[53] H.-Y. Chen and M.-L. Huang, "Discrimination between normal and glaucomatous eyes using Stratus optical coherence tomography in Taiwan Chinese subjects," *Graefes. Arch. Clin. Exp. Opththalmol.*, vol. 243, no. 9, pp. 894–902, 2005.

[54] K. Lee, Y. H. Kwon, M. K. Garvin, M. Niemeijer, M. Sonka, and M. D. Abràmoff, "Distribution of damage to the entire retinal ganglion cell pathway," *Arch Ophthalmol*, vol. 130, no. 9, pp. 1118–1126, Sept. 2012.

[55] M. K. Garvin, M. D. Abràmoff, K. Lee, M. Niemeijer, M. Sonka, and Y. H. Kwon, "2-D pattern of nerve fiber bundles in glaucoma emerging from spectral-domain optical coherence tomography," *Invest Ophthalmol Vis Sci*, vol. 53, no. 1, pp. 483–489, Jan. 2012.

[56] Z. Popovic, J. Thaung, P. Knutsson, and M. Owner-Petersen, "Dual conjugate adaptive optics prototype for wide field high resolution retinal imaging," in *Adaptive Optics Progress*, R. K. Tyson, Ed. InTech, Dec. 2012, ch. 1, pp. 125–143.

[57] N. G. Strouthidis, H. Yang, B. Fortune, J. C. Downs, and C. F. Burgoyne, "Detection of the optic nerve head neural canal opening within three-dimensional histomorphometric and spectral domain optical coherence tomography data sets," *Invest Ophthalmol Vis Sci*, vol. 50, no. 1, pp. 214–223, 2009.

[58] H. Yang, J. C. Downs, A. Bellezza, H. Thompson, and C. F. Burgoyne, "3–D histomorphometry of the normal and early glaucomatous monkey optic nerve head: prelaminar neural tissues and cupping," *Invest Ophthalmol Vis Sci*, vol. 48, no. 11, pp. 5068–5084, Nov. 2007.

[59] J. C. Downs, H. Yang, C. Girkin, L. Sakata, A. Bellezza, H. Thompson, and C. F. Burgoyne, "Three–dimensional histomorphometry of the normal and early glaucomatous monkey optic nerve head: neural canal and subarachnoid space architecture," *Invest Ophthalmol Vis Sci*, vol. 48, no. 7, pp. 3195–3208, July 2007.

[60] H. Kolb, E. Fernandez, and R. Nelson, *Webvision: The Organization of the Retina and Visual System*. University of Utah Health Sciences Center, 1995.

[61] M. Wojtkowski, R. Leitgeb, A. Kowalczyk, T. Bajraszewski, and A. F. Fercher, "In vivo human retinal imaging by Fourier domain optical coherence tomography," *J Biomed Opt*, vol. 7, no. 3, pp. 457–463, July 2002.

[62] M. Wojtkowski, T. Bajraszewski, I. Gorczyńska, P. Targowski, A. Kowalczyk, W. Wasilewski, and C. Radzewicz, "Ophthalmic imaging by spectral optical coherence tomography," *Am J Ophthalmol*, vol. 138, no. 3, pp. 412–419, Sept. 2004.

[63] M. Wojtkowski, V. Srinivasan, J. G. Fujimoto, T. Ko, J. S. Schuman, A. Kowalczyk, and J. S. Duker, "Three-dimensional retinal imaging with high-speed ultrahigh-resolution optical coherence tomography," *Ophthalmology*, vol. 112, no. 10, pp. 1734–1746, Oct. 2005.

[64] D. C. DeBuc, "A review of algorithms for segmentation of retinal image data using optical coherence tomography," in *Image Segmentation*, P.-G. Ho, Ed. InTech, 2011.

[65] D. Koozekanani, K. Boyer, and C. Roberts, "Retinal thickness measurements from optical coherence tomography using a Markov boundary model," *IEEE Trans. Med. Imag.*, vol. 20, no. 9, pp. 900–916, Sept. 2001.

[66] X. Zhang, S. Yousefi, L. An, and R. K.Wang, "Automated segmentation of intramacular layers in Fourier domain optical coherence tomography structural images from normal subjects," *J Biomed Opt*, vol. 17, no. 4, p. 046011, Apr. 2012.

[67] S. Lu, C. Y. l. Cheung, J. Liu, J. H. Lim, C. K.-S. Leung, and T. Y. Wong, "Automated layer segmentation of optical coherence tomography images," *IEEE Trans. Biomed. Eng.*, vol. 57, no. 10, pp. 2605–2608, Oct. 2010.

[68] M. Mujat, R. Chan, B. Cense, B. Park, C. Joo, T. Akkin, T. Chen, and J. de Boer, "Retinal nerve fiber layer thickness map determined from optical coherence tomography images," *Opt Express*, vol. 13, no. 23, pp. 9480–9491, Nov. 2005.

[69] X. Wu and D. Z. Chen, "Optimal net surface problems with applications," in *Proc. of the 29th International Colloquium on Automata, Languages, and Programming (ICALP), LNCS 2380*. Springer-Verlag, 2002, pp. 1029–1042.

[70] K. Li, X. Wu, D. Z. Chen, and M. Sonka, "Optimal surface segmentation in volumetric images–a graph-theoretic approach," *IEEE Trans. Pattern Anal. Machine Intell.*, vol. 28, no. 1, pp. 119–134, Jan. 2006.

[71] X. Xu, M. Niemeijer, Q. Song, M. Sonka, M. K. Garvin, J. M. Reinhardt, and M. D. Abràmoff, "Vessel boundary delineation on fundus images using graph based approach," *IEEE Trans. Med. Imag.*, vol. 30, no. 6, pp. 1184–1191, June 2011.

[72] Q. Song, X. Wu, Y. Liu, M. Smith, J. Buatti, and M. Sonka, "Optimal graph search segmentation using arc-weighted graph for simultaneous surface detection of bladder and prostate," in *Medical Image Computing and Computer-Assisted Intervention (MICCAI)*, no. Pt 2, Jan. 2009, pp. 827–835.

[73] Q. Song, M. Chen, J. Bai, M. Sonka, and X. Wu, "Surface-region context in optimal multi-object graph-based segmentation: robust delineation of pulmonary tumors," in *Information Processing in Medical Imaging (IPMI)*, Jan. 2011, pp. 61–72.

[74] Y. Yin, X. Zhang, R. Williams, X. Wu, D. Anderson, and M. Sonka, "LOGISMOS: Layered optimal graph image segmentation of multiple objects and surfaces: Cartilage segmentation in the knee joint," *IEEE Trans. Med. Imag.*, vol. 29, no. 12, pp. 2023–2037, 2010.

[75] Q. Song, X. Wu, X. Dou, and M. Sonka, "Globally optimal 3–d graph search incorporating both edge and regional information: application to aortic MR image segmentation," in *Proc. SPIE, Med. Img. 2009: Img. Proc.*, Feb. 2009, p. 725913 (8 pages).

[76] Q. Song, J. Bai, M. K. Garvin, M. Sonka, J. M. Buatti, and X. Wu, "Optimal multiple surface segmentation with shape and context priors," *IEEE Trans. Med. Imag.*, vol. 32, no. 2, pp. 376–386, Feb. 2013.

[77] B. J. Antony, M. D. Abràmoff, M. M. Harper, W. Jeong, E. H. Sohn, Y. H. Kwon, R. Kardon, and M. K. Garvin, "A combined machine-learning and graph-based framework for the segmentation of retinal surfaces in SD-OCT volumes," *Biomed Opt Express*, vol. 4, no. 12, pp. 2712–2728, 2013.

[78] C.-L. Tsai, C.-Y. Li, G. Yang, and K.-S. Lin, "The edge-driven dual-bootstrap iterative closest point algorithm for registration of multimodal fluorescein angiogram sequence," *IEEE Trans. Med. Imag.*, vol. 29, no. 3, pp. 1707–1718, Mar. 2010.

[79] M. Niemeijer, K. L. M. K. Garvin, M. D. Abràmoff, and M. Sonka, "Registration of 3-D spectral OCT volumes combining ICP with a graph-based approach," in *Proc. SPIE, Med. Img. 2012: Img. Proc.*, vol. 8314, 2012, p. 83141A (9 pages).

[80] M. Skokan, A. Skoupy, and J. Jan, "Registration of multimodal images of retina," in *Proc. IEEE Conf. Eng. Med. Biol.*, vol. 2, 2002, pp. 1094–1096.

[81] F. Maes, A. Collignon, D. Vandermeulen, G. Marchal, and P. Suetens, "Multimodality image registration by maximization of mutual information," *IEEE Trans. Med. Imag.*, vol. 16, no. 2, pp. 187–198, Apr. 1997.

[82] P. Thevenaz and M. Unser, "Optimization of mutual information for multiresolution image registration," *IEEE Trans. Imag. Proc.*, vol. 9, no. 19, pp. 2083–2099, Dec. 2000.

[83] J. P. W. Pluim, J. B. A. Maintz, and M. A. Viergever, "Mutual-information based registration of medical images: a survey," *IEEE Trans. Med. Imag.*, vol. 22, no. 8, pp. 986–1004, Aug. 2003.

[84] E. Peli, R. A. Augliere, and G. T. Timberlake, "Feature-based registration of retinal images," *IEEE Trans. Med. Imag.*, vol. MI-6, no. 2, pp. 272–278, Sept. 1987.

[85] H. Bogunović, M. Sonka, Y. H. Kwon, P. Kemp, M. D. Abràmoff, and X. Wu, "Multi-surface and multi-field co-segmentation of 3-D retinal optical coherence tomography," *IEEE Trans. Med. Imag.*, vol. 33, no. 12, pp. 2242–2253, Dec. 2014.

[86] P. C. Cattin, H. Bay, L. V. Gool, and G. Székely, "Retina mosaicing using local features," in *MICCAI*, vol. 4191, 2006, pp. 185–192.

[87] M. Haeker, M. D. Abràmoff, X. Wu, R. Kardon, and M. Sonka, "Use of varying constraints in optimal 3-D graph search for segmentation of macular optical coherence tomography images," in *Medical Image Computing and Computer-Assisted Intervention (MICCAI)*, vol. 4791, no. Pt 1, 2007, pp. 244–259.

[88] M. S. Miri, K. Lee, M. Niemeijer, M. D. Abràmoff, Y. H. Kwon, and M. K. Garvin, "Multimodal segmentation of optic disc and cup from stereo fundus and SD-OCT images," in *Proc. SPIE, Med. Img. 2013: Img. Proc.*, vol. 8669, Orlando, Florida, Mar. 2013, p. 86690O (9 pages).

[89] M. S. Miri, M. D. Abràmoff, K. Lee, M. Niemeijer, A. Whale, Y. H. Kwon, and M. K. Garvin, "A multimodal machine-learning-based approach for segmenting the optic disc and cup in fundus and SD-OCT images," pp. E–abstract, May 2013.

[90] R. Kolar and P. Tasevsky, "Registration of 3D retinal optical coherence tomography data and 2D fundus images," in *WBIR*, vol. 6204, June 2010, pp. 72–82.

[91] Y. Li, nGiovanni Gregori, R. W. Knighton, B. J. Lujan, and P. J. Rosenfeld, "Registration of OCT fundus images with color fundus photographs based on blood vessel ridges," *Opt. Exp.*, vol. 19, no. 1, pp. 7–16, Jan. 2011.

[92] M. Golabbakhsh and H. Rabbani, "Vessel-based registration of fundus and optical coherence tomography projection images of retina using a quadratic registration model," *IET Imag. Proc.*, vol. 7, no. 8, pp. 768–776, Nov. 2013.

[93] Z. Hu, M. Niemeijer, M. D. Abràmoff, and M. K. Garvin, "Multimodal retinal vessel segmentation from spectral-domain optical coherence tomography and fundus photography," *IEEE Trans. Med. Img.*, vol. 31, no. 10, pp. 1900–1911, Oct. 2012.

[94] M. Niemeijer, J. Staal, B. van Ginneken, M. Loog, and M. D. Abràmoff, "Comparative study of retinal vessel segmentation methods on a new publicly available database," in *Proc. SPIE, Med. Img. 2004: Img. Proc.*, vol. 5370, 2004, pp. 648–656.

[95] M. Niemeijer, M. K. Garvin, B. van Ginneken, M. Sonka, and M. D. Abràmoff, "Vessel segmentation in 3-D spectral OCT scans of the retina," in *Proc. SPIE, Med. Img. 2008: Img. Proc.*, vol. 6914, 2008, p. 69141R (8 pages).

[96] P. J. Besl and N. D. McKay, "A method for registration of 3-D shapes," *IEEE Trans. Patt. Anal. Mach. Intell.*, vol. 12, no. 14, pp. 239–256, Feb. 1992.

[97] A. Corana, M. Marchesi, C. Martini, and S. Ridella, "Minimizing multimodal functions of continuous variables with the "simulated annealing" algorithm," *ACM Trans. Math. Software*, vol. 13, no. 3, pp. 262–280, 1987.

[98] M. J. D. Powell, "An efficient method for finding the minimum of a function of several variables without calculating derivatives," *The Comput J*, vol. 7, no. 2, pp. 155–162, 1964.

[99] L. Breiman, "Random forests," *Mach. Learn.*, vol. 45, no. 1, pp. 5–32, 2001.

[100] M. W. Schwarz, W. B. Cowan, and J. C. Beatty, "An experimental comparison of RGB, YIQ, LAB, HSV, and opponent color models," *ACM Trans. Graphics*, vol. 6, no. 2, pp. 123–158, Apr. 1987.

[101] J. E. Fowler, "The redundant discrete wavelet transform and additive noise," *IEEE Sig. Proc. Let.*, vol. 12, no. 9, pp. 629–632, Sept. 2005.

[102] Z. Hu, M. Niemeijer, M. D. Abràmoff, K. Lee, and M. K. Garvin, "Automated segmentation of 3-D spectral OCT retinal blood vessels by neural canal opening false positive suppression," in *Proc. MICCAI 2010, LNCS*, vol. 6363, 2010, pp. 33–40.

[103] M. S. Miri, H. Bogunovic̀, Y. H. Kwon, M. D. Abràmoff, M. Sonka, and M. K. Garvin, "Minimum rim width better correlates with structural and functional measurements than horizontal rim width," pp. E–abstract, May 2015.

[104] M. S. Miri, Y. H. Kwon, J.-K. Wang, M. D. Abràmoff, M. Sonka, and M. K. Garvin, "Computing the minimum rim width: Should the border tissue be considered?" pp. E–abstract, May 2014.

[105] J. Morgan, "Optic nerve head structure in glaucoma: astrocytes as mediators of axonal damage," *Eye (Lond)*, vol. 14, pp. 437–444, 2000.

[106] R. R. A. Bourne, "GLOSSARY the optic nerve head in glaucoma," *Community Eye Heal.*, vol. 19, no. 59, pp. 44–45, Sept. 2006.

[107] D. F. Garway-Heath, S. T. Ruben, A. Viswanathan, and R. Hitchings, "Vertical cup/disc ratio in relation to optic disc size: its value in the assessment of the glaucoma suspect," *B J Ophthalmol*, vol. 82, no. 10, pp. 1118–1124, 1998.

[108] A. S. C. Reis, N. O'Leary, H. Yang, G. P. Sharpe, M. T. Nicolela, and C. F. B. B. C. Chauhan, "Influence of clinically invisible, but optical coherence tomography detected, optic disc margin anatomy on neuroretinal rim evaluation," *Invest Ophthalmol Vis Sci*, vol. 53, no. 4, pp. 1852–1860, 2012.

[109] S. K. Gardiner, R. Ren, H. Yang, B. Fortune, C. F. Burgoyne, and S. Demirel, "A method to estimate the amount of neuroretinal rim tissue in glaucoma: comparison with current methods for measuring rim area," *Am J Ophthalmol*, vol. 157, no. 3, pp. 540–549, 2014.

[110] H. Bogunović, Y. H. Kwon, A. Rashid, K. Lee, D. B. Critser, M. K. Garvin, M. Sonka, and M. D. Abràmoff, "Multi-surface and multi-field co-segmentation of 3-D retinal optical coherence tomography," *Invest Ophthalmol Vis Sci*, vol. 56, no. 1, pp. 259–271, Jan. 2015.

[111] M. K. Garvin, K. Lee, T. L. Burns, M. D. Abràmoff, M. Sonka, and Y. H. Kwon, "Reproducibility of SD-OCT-based ganglion cell-layer thickness in glaucoma using two different segmentation algorithms," *Invest Ophthalmol Vis Sci*, vol. 54, no. 10, pp. 6998–7004, 2013.

[112] G. Y. Zou, "Toward using confidence interval to compare correlations," *Psychol. Methods*, vol. 12, no. 4, pp. 399–413, Dec. 2007.

[113] J. S. Schuman, "Spectral domain optical coherence tomography for glaucoma (an AOS thesis)," *Trans. Am. Ophthalmol. Soc.*, vol. 106, pp. 426–458, Dec. 2008.

[114] H. M. Taha, N. El-Bendary, A. E. Hassanien, Y. Badr, and V. Snase, "Retinal feature-based registration schema," in *ICIEIS*, vol. 252, 2011, pp. 26–36.

[115] M. Niemeijer, M. K. Garvin, K. Lee, B. van Ginneken, M. D. Abràmoff, and M. Sonka, "Registration of 3D spectral OCT volumes using 3D sift feature point matching," in *Proc. SPIE, Med. Img. 2009: Img. Proc.*, vol. 7259, 2013, p. 72591I (8 pages).

[116] J. Chen, J. Tian, N. Lee, J. Zheng, R. T. Smith, and A. F. Laine, "A partial intensity invariant feature descriptor for multimodal retinal image registration," *IEEE Trans. Biomed. Eng.*, vol. 57, no. 7, pp. 1707–1718, July 2010.

[117] Y. Lin and G. Medioni, "Retinal image registration from 2D to 3D," in *Computer Vision and Pattern Recognition (CVPR)*, June 2008, pp. 1–8.

[118] G. Yang, C. V. Stewart, M. Sofka, and C.-L. Tsai, "Registration of challenging image pairs: Initialization, estimation, and decision," *IEEE Trans. Patt. Anal. Mach. Intell.*, vol. 29, no. 11, pp. 272–278, Nov. 2007.

[119] J. Zheng, J. Tian, K. Deng, X. Dai, X. Zhang, and M. Xu, "Salient feature region: A new method for retinal image registration," *IEEE Trans. Inf. Tech. Biomed.*, vol. 15, no. 2, pp. 221–232, Mar. 2011.

[120] G. K. Matsopoulos, P. A. Asvestas, N. A. Mouravliansky, and K. K. Delibasis, "Multimodal registration of retinal images using self organizing maps," *IEEE Trans. Med. Imag.*, vol. 23, no. 12, pp. 1557–1563, Dec. 2004.

[121] Z. Ghassabi, J. Shanbehzadeh, A. Sedaghat, and E. Fatemizadeh, "An efficient approach for robust multimodal retinal image registration based on UR-SIFT features and PIIFD descriptors," *EURASIP J. Imag. Vid. Proc.*, vol. 25, p. 16 pages, Dec. 2013.

[122] S. Niu, Q. Chen, H. Shen, L. de Sisternes, and D. L. Rubin, "Registration of SD-OCT en-face images with color fundus photographs based on local patch matching," in *MICCAI Worshop: Ophthalmic Medical Image Analysis*, Sept. 2014, pp. 25–32.

[123] E. Rosten and T. Drummond, "Fusing points and lines for high performance tracking," in *IEEE Int. Conf. Comp. Vis.*, vol. 2, Oct. 2005, pp. 1508–1511.

[124] E. Rosten and T. Drummond, "Machine learning for high-speed corner detection," in *Eur. Conf. Comp. Vis.*, vol. 1, May 2006, pp. 430–443.

[125] N. Dalal and B. Triggs, "Histograms of oriented gradients for human detection," in *IEEE Comp. Soc. Conf. Comp. Vis. Patt. Rec. (CVPR)*, vol. 1, June 2005, pp. 886–893.

[126] D. G. Lowe, "Distinctive image features from scale-invariant keypoints," *Int. J. Comp. Vis.*, vol. 60, no. 2, pp. 91–110, Nov. 2004.

[127] R. Hartley and A. Zisserman, *Multiple View Geometry in Computer Vision*, 2nd ed. Cambridge University Press, 2004.

[128] S. M. Pizer, E. P. Amburn, J. D. Austin, R. Cromartie, A. Geselowitz, T. Greer, B. T. H. Romeny, and J. B. Zimmerman, "Adaptive histogram equalization and its variations," *Comp. Vis. Graph. Img. Proc.*, vol. 39, no. 3, pp. 355–368, Sept. 1987.

[129] M. S. Miri, V. A. Robles, M. D. Abràmoff, Y. H. Kwon, and M. K. Garvin, "Multimodal graph-theoretic approach for segmentation of the internal limiting membrane at the optic nerve head," *MICCAI Workshop: Ophthalmic Medical Image Analysis (OMIA)*, pp. 57–64, 2015.

[130] A. Shah, J.-K. Wang, M. K. Garvin, M. Sonka, and X. Wu, "Automated surface segmentation of internal limiting membrane in spectral-domain optical coherence tomography volumes with a deep cup using a 3-D range expansion approach," in *Biomedical Imaging (ISBI), 2014 IEEE 11th International Symposium on*, 2014, pp. 1405–1408.

[131] C. Xu and J. L. Prince, "Snakes, shapes, and gradient vector flow," *IEEE Trans. Image Process.*, vol. 7, no. 3, pp. 359–369, Mar. 1998.

[132] R. Kafieh, H. Rabbani, and S. Kermani, "A review of algorithms for segmentation of optical coherence tomography from retina," *J. Med. Signals Sens.*, vol. 3, no. 1, pp. 45–60, 2013.

[133] T. M. Shaarawy, M. B. Sherwood, J. G. Crowston, and R. A. Hitchings, *Glaucoma Volume 1: Medical Diagnosis and Therapy*, 1st ed. Saunders Ltd., May 2009.

[134] A. Lang, A. Carass, P. A. Calabresi, H. S. Ying, and J. L. Prince, "An adaptive grid for graph-based segmentation in retinal OCT," in *Proc. SPIE, Med. Imag. 2014: Imag. Proc.*, vol. 9034, 2014, p. 903402 (9 pages).

[135] I. Oguz and M. Sonka, "LOGISMOS-B: Layered optimal graph image segmentation of multiple objects and surfaces for the brain," *IEEE Trans. Med. Imag.*, vol. 33, no. 6, pp. 1220–1235, June 2014.

[136] M. S. Miri, M. D. Abràmoff, Y. H. Kwon, M. Sonka, and M. K. Garvin, "Automated 3D segmentation of bruch's membrane opening from SD-OCT volumes," May 2016, accepted.

[137] E. Rosten, R. Porter, and T. Drummond, "Faster and better: A machine learning approach to corner detection," *IEEE Trans. Pattern Anal. Mach. Intell.*, vol. 32, no. 1, pp. 105–119, Jan. 2010.

[138] S. E. Grigorescu, N. Petkov, and P. Kruizinga, "Comparison of texture features based on Gabor filters," *IEEE Trans. Image Process.*, vol. 11, no. 10, pp. 1160–1167, Jan. 2002.